STATICS AND DYNAMICS OF SIMPLE FLUIDS ON CHEMICALLY PATTERNED SUBSTRATES

Von der Fakultät Mathematik und Physik der Universität Stuttgart
zur Erlangung der Würde eines
Doktors der Naturwissenschaften (Dr. rer. nat.)
genehmigte Abhandlung

von
Fabian Dörfler
aus Steinheim an der Murr

Hauptberichter: Prof. Dr. S. Dietrich
Mitberichter: Prof. Dr. J. Main
Tag der mündlichen Prüfung: 16.02.2010

Max-Planck-Institut für Metallforschung, Stuttgart
Institut für Theoretische und Angewandte Physik (ITAP), Universität Stuttgart

2009

Contents

Erklärung **3**

CV **4**

Einführung und Zusammenfassung **7**

Introduction **19**

Symbols and Notations **29**

1 Fluids in Equilibrium **31**

1.1 The capillary model 35
1.2 Microscopic density functional theory 40
1.3 Minimization of the free energy 48

2 Fluid Dynamics from Kinetic Theory **53**
2.1 The Boltzmann equation 57
2.2 The fluid-dynamic limit of the Boltzmann equation 68
2.3 The BGK-model 78
2.4 The Chapman-Enskog analysis 84

3 The Lattice Boltzmann Approach **91**
3.1 The lattice Boltzmann equation 94
3.2 The Shan-Chen model 100
3.3 The free energy model 108

4 Macroscopic Fluid Properties **115**
4.1 Morphologic transitions on chemical channels 118
4.2 Dynamics on chemical channels 142

5 Mesoscopic Fluid Properties **161**
5.1 Mesoscopic droplet morphologies 167
5.2 Analytical model 168
5.3 The morphologic transition of mesoscopic droplets 172

Bibliography **185**

Erklärung

Gemäß §5 Absatz 3 der Prüfungsordnung der Universität Stuttgart erkläre ich hiermit, die vorliegende Arbeit eigenständig unter Zuhilfenahme der angegebenen Quellen durchgeführt zu haben.

Stuttgart, im November 2009,

Fabian Dörfler

Curriculum Vitae

Fabian Dörfler

1976	geboren in Steinheim an der Murr
1988 - 1996	Friedrich-Schiller-Gymnasium in Marbach/Neckar
1997	Zivildienst
1998 - 2000	Ausbildung zum Schreiner in Ludwigsburg
2000 - 2005	Studium der Physik an der Universität Stuttgart
2005/2006	Diplomarbeit am Max-Planck-Institut für Metallforschung bei Prof. Dr. M. Fäħnle
	Contributions to the Theory of X-ray magnetic Dichroism in Solids
2006 - 2009	Promotion am Max-Planck-Institut für Metallforschung bei Prof. Dr. S. Dietrich
	Statics and Dynamics of Simple Fluids on chemically patterned Substrates

Einführung und Zusammenfassung

Benetzungsphänomene sind eine alltägliche Erscheinung. Man denke etwa an morgendliche Tautropfen auf Blättern und an Grashalmen, sich in einer Pfanne ausbreitendes Olivenöl oder an einem Geländer hängende Regentropfen.

Die naturwissenschaftliche Beschreibung von Benetzungsphänomenen nahm im neunzehnten Jahrhundert ihren Anfang mit den Arbeiten von Young und Laplace [1–3]. Während Young den Kontaktwinkel eines auf einem festen Substrat sitzenden Flüssigkeitströpfchens auf ein Kräftegleichgewicht an der Kontaktlinie zurückführte, setzte Laplace die Krümmung der Oberfläche eines solchen Tröpfchens in Verbindung zu seiner Oberflächenspannung und der Druckdifferenz der Flüssigkeit zur umgebenden Gasphase. Wenig später war es Gauss, der erstmals eine Betrachtung der Flüssigkeitsoberfläche unter Anwendung eines Minimalprinzips durchführte [4]. Die Arbeiten von Young, Laplace und Gauss münden in das sogenannte *Kapillarmodell*, in dessen Rahmen sich die Benetzungseigenschaften aus der Variation eines phänomenologischen Funktionals gewinnen lassen, welches die freie Energie des Systems aus Substrat, Flüssigkeit und umgebender Gasphase erfasst. Heutzutage werden Benetzungsphänomene als das Resultat von Wechselwirkungen auf der molekularen bzw. atomaren Ebene verstanden, begleitet von entropischen bzw. durch thermische Fluktuation- en bedingte Effekte [5].

Die vorliegende Arbeit hat die theoretische Untersuchung des Benetzungsverhaltens einfacher Fluide auf planaren, chemisch strukturierten Substraten zum Thema.

Einfache Fluide bezeichnen dabei kondensierte oder gasförmige Systeme bestehend aus Teilchen ohne Orientierungs- oder intrinsische Freiheitsgrade, welche über kurz- oder lang- reichweitige Potentiale, beispielsweise Hartkugel- oder Lennard-Jones-Potentiale, elastisch miteinander wechselwirken.

Das Benetzungsverhalten von solchen Fluiden auf einem festen Substrat ist dabei das Resultat der Wechselwirkungen von Fluidteilchen untereinander und von Fluidteilchen mit dem Substrat. Die Eigenschaften der Substratteilchen, aus denen sich Stärke und Reichweite der Fluid-Substrat-Wechselwirkungspotentiale ergeben, werden als chemische Eigenschaften des Substrates bezeichnet. Im Falle eines chemisch strukturierten Substrates verhalten sich diese Eigenschaften derart, daß sich auf der Substratoberfläche zusammenhängende Bereiche jeweils unterschiedlichen Benetzungsverhaltens ergeben. Domänen hoher Benetzbarkeit, d.h. Bereiche auf denen ein bestimmtes Fluid bevorzugt adsorbiert, werden dabei als *lyophil* bezeichnet, gegenüber den *lyophoben* Domänen niederer Benetzbarkeit.

Zusätzlich zu den obengenannten Wechselwirkungen kann das Benetzungsverhalten durch eine topologische Sturktur der Substratoberfläche maßgeblich beeinflusst werden - ein vielzitiertes Beispiel hierfür ist der sogenannte *Lotusblüteneffekt* [6]. Darüber hinaus hat natürlich die Gravitation einen gewissen Einfluß auf die Morphologie eines benetzenden Fluids. Im Rahmen dieser Arbeit werden jedoch einerseits ausschließlich planare Oberflächen betrachtet - d.h. Oberflächen, deren Rauhigkeit hinsichtlich des Benetzungsverhaltens auf irrelevanten Längenskalen gegeben ist - und andererseits bewegen sich die Abmessungen der betrachteten Fluide hinreichend weit unterhalb ihrer Kapillarlänge - d.h. der aus dem Einfluß der Gravitation auf das Benetzungsverhalten eines bestimmten Fluids resultierenden Längenskala -, sodaß Gravitationseffekte vernachlässigbar sind.

Chemisch strukturierte Substrate eröffnen interessante technologische Perspektiven im Bereich der sogennanten *Mikrofluidik*, in der mit Strukturen und Fluidmengen operiert wird, deren charakteristische Abmessungen im μm-Bereich und somit recht weit unterhalb der Kapillarlänge liegen. So ist es etwa möglich, Flüssigkeiten auf streifenförmigen lyophilen Domänen in einer lyophoben Umgebung - sogenannten *chemischen Kanälen* - gezielt über planare Oberflächen zu leiten. Darauf gründet sich das Konzept der sogenannten *chemischen Chips*, auf denen in Analogie zu den integrierten mikroelektronischen Schaltkreisen auf CPUs integrierte Netzwerke chemischer Kanäle und anderer lyophiler und lyophober Domänen mikrochemische Analyse- oder Reaktionseinheiten bilden (*lab-on-a-chip concept*) [7–9]. Solche chemischen Chips sollen die Handhabung und Verarbeitung kleinster Mengen wertvoller, seltener, toxischer oder explosiver Substanzen ermöglichen.

Die durch chemische Strukturierung eines Substrates hergestellten Funktionseinheiten werden dabei, wegen der Existenz einer freien, räumlich nicht durch Substratkontakt einge- schränkten Fluidgrenzfläche, als offene mikrofluidale Einheiten bezeichnet [10–14]. Der Fluidtransport auf solchen offenen Einheiten kann mittels Trägheitskräften, Scherfluß oder Benetzbarkeitsgradienten erfolgen. Das Augenmerk bei der Entwicklung chemischer Chips richtet sich momentan jedoch hauptsächlich auf geschlossene mikrofluidale Einheiten, in denen Fuide in geometrisch geschlossenen Strukturen wie Kapillaren und Kammern gehalten werden und der Fluidtransport mittels Druckgradienten und Ventilen geregelt wird [15]. Gegenüber solchen geschlossenen Einheiten könnten offene Einheiten einige Vorteile bieten, die hauptsächlich darin begründet liegen, daß im Falle der reduzierten Längenskalen in der Mikrofluidik Grenzflächenphänomene gegenüber Volumeneffekten an Bedeutung gewinnen.

So ist beispielsweis nach dem Gesetz von *Hagen* und *Poiseuille* der laminare, schlupffreie Volumenstrom eines homogenen Fluids mit gegebener Viskosität durch eine Kapillare gegebener Länge proportional zum Produkt des Druckgradienten mit der vierten Potenz des Kapillarradiusses. Im Längenskalenbereich der Mikrofluidik könnten somit chemische Kanäle den Kapillaren hinsichtlich der Transporteigenschaften überlegen sein. Desweiteren sind Kapillare anfällig für eine Verstopfung durch gelöste Teilchen, etwa in Form von Kolloiden oder Polymeren, hervorgerufen durch eine Anlagerung derselben an den Kapillarwänden. Insbesondere in dieser Hinsicht kann man sich von chemischen Kanälen

Vorteile erhoffen.

Die Miniaturisierung mikrofluidaler Einheiten mit Strukturen im Bereich von μm führt zu Längenskalen im Bereich von $10 - 100\,nm$, d.h. die Mikrofluidik wird zur Nanofluidik [16–18]. Während in der Mikroelektronik Quanteneffekte die Grenze der Miniaturisierung vorgeben, spielen im Falle offener nanofluidaler Einheiten die thermischen Fluktuationen der freien Fluidgrenzfläche die ausschlaggebende Rolle.

Es existiert eine Reihe verschiedener Verfahren zur chemischen Strukturierung von Substraten auf unterschiedlichen Längenskalen.

Chemische Strukturen im mm-Bereich können relativ einfach durch Schablonendruck- oder Ätzverfahren hergestellt werden. Die μm-Skala ist durch die Technik des Mikrokontaktdruckens, Molekularstrahlepitaxie mit Gittermasken, elektrophoretische Aggregation von Kolloiden oder durch Aufreißen eines Polymerfilmes zugänglich [19–23]. Chemischen Strukturierung auf der nm-Skala gelingt durch Photolithographische Methoden, lokale Oxydation mittels AFM-Spitzen sowie Molekularstrahl- epitaxie mit Lichtmasken [24–26].

Für die Konzeption offener mikro- bzw. nanofluidaler Einheiten zum Aufbau chemischer Chips ist eine fundierte theoretische Beschreibung sowohl statischer Benetzungsphänomene als auch der Benetzungsdynamik bzw. der Fluiddynamik auf chemisch strukturierten Substraten von großer Bedeutung. Eine solche Beschreibung ist zuallererst eine Sache der betrachteten Längenskala. Wie schon erwähnt, spielen sich Mikro- und Nanofluidik auf Längenskalen recht weit unterhalb der Kapillarlänge der jeweiligen Fluide ab, sodaß Gravitationseffekte der Beschreibung außen vor bleiben können. Die Beschreibung von Benetzungsphänomenen gründet sich somit auf einer für die betrachtete Längenskala sinnvollen Erfassung molekularer Wechselwirkungen der Fluidteilchen untereinander sowie der Fluidteilchen mit dem Substrat.

Auf einer makroskopischen Skala, hinreichend groß gegenüber der Reichweite molekularer Wechselwirkungen, kann das Gleichgewichtsbenetzungsverhalten eines Systems zweier fluider Phasen auf einem festen Substrat durch das eingangs erwähnte Kapillarmodell sehr gut beschrieben werden. Demnach ist die räumliche Konfiguration eines Systems zweier Fluide in Kontakt mit einem festen Substrat durch eine Fluid-Fluid-Grenzfläche, die beiden Fluid-Substrat-Grenzflächen sowie eine Drei-Phasen-Kontaktlinie gegeben. Diese geometrischen Objekte sind jeweils mit freien Energiedichten belegt, den sogenannten Grenz- flächenspannungen bzw. der sogenannten Linienspannung, in denen die auf der makroskopischen Skala sehr kurzreichweitigen molekularen Wechselwirkungen indirekt zum Ausdruck kommen. Die Konfiguration minimaler freier Energie zu gegebenen Volumina oder zu einer gegebenen Druckdifferenz der beiden Fluide definiert dann die Krümmung der Fluid-Fluid Grenzfläche sowie den Gleichgewichtskontaktwinkel der Fluid-Fluid-Grenzfläche an der Drei-Phasen-Kontaktline, der ein Maß für die Benetzbarkeit des Substrates darstellt. Chemisch strukturierte Substrate sind somit im Rahmen des Kapillarmodells durch eine Variation des Kontaktwinkels gekennzeichnet, wobei lyophile bzw. lyophobe Domänen einen Kontakt- winkel kleiner bzw. größer als 90° aufweisen.

Auf einer mikroskopischen Skala im und unterhalb des Bereichs der Reichweite molekularer Wechselwirkungen, auf einer Skala also, auf der molekulare

Wechselwirkungen von langer Reichweite sind, hat die Beschreibung unter direkter Berücksichtigung der Wechselwirkungspotentiale zu erfolgen. Im Rahmen einer *Dichtefunktionaltheorie* ist die freie Energie des System durch ein Dichtefunktional gegeben. Die Gleichgewichtskonfiguration des Systems ist dann durch kontinuierliche Dichteprofile gekennzeichnet, die einem Minimum dieses Funktionals entsprechen. An Stelle der Grenzflächen und der Drei-Phasen-Kontaktlinie als geometrische Objekte ohne innere Struktur treten somit räumlich ausgedehnte Phasengrenzbereiche mit einer durch den Verlauf dieser Profile gekennzeichneten inneren Struktur.

Im Hinblick auf eine Miniaturisierung mikrofluidaler Einheiten mit Strukturen im Bereich von μm hin zu Strukturen im nm-Bereich ist die dazwischenliegende, sogenannte mesoskop- ische Längenskala von großer Bedeutung. Auf dieser Skala betrachtet, sind zwar einerseits die molekularen Wechselwirkungen nicht mehr als kurzreichweitig anzusehen, andererseits aber sind makroskopische Konzepte wie zweidimensionale Grenzflächen belegt mit Grenzflächenspannungen immer noch sinnvoll. Dies entspricht der Feststellung, daß die innere Struktur einer Phasengrenze auf der mesoskopischen Skala nicht signifikant ist. So können die grundlegenden Konzepte des makroskopischen Kapillarmodells und der obengenannten mikroskopischen Dichtefunktionaltheorie miteinander verschmolzen werden, um den auf der mesoskopischen Skala mittel- bis langreichweitigen molekularen Wechselwirkungen Rechnung zu tragen [5, 27–29]. Die Benetzungseigenschaften eines Substrates folgen im Rahmen einer solchen mesoskopischen Beschreibung aus einem *effektiven Grenzflächen- potential*, welches die effektive Wechselwirkung eines Fluidfilms mit dem Substrat als Funktion der lokalen Filmdicke modelliert, wobei eine chemische Strukturierung des Substrates sich in der Topologie des effektiven Grenzflächenpotentials wiederspiegelt.

Die makroskopische Dynamik von Fluiden, und damit auch deren Benetzungsdynamik, ist im Prinzip durch die *Navier-Stokes-Gleichungen* gegeben. Wie im Kapillarmodell treten auch in diesen Gleichungen die molekularen Wechselwikungen indirekt zu tage, und zwar in Form der sog. Transportkoeffizienten, welche die Viskosität und die thermische Leitfähigkeit eines Fluids angeben, sowie in den fluiddynamischen Randbedingungen an den Phasengrenzen. Die Berücksichtigung langreichweitiger molekularer Wechselwirkungen und thermischer Fluktuationen in den Navier-Stokes-Gleichungen sowie des fluiddynamischen Schlupfes in den Randbedingungen führt zur mesoskopischen Fluiddynamik [30, 31]. Ein wichtiges analytisches Hilfsmittel in diesem Zusammenhang ist die sogenannte *Lubrikationsnäherung*, mittels derer die Evolutionsgleichung dünner Filme aus den Navier-Stokes-Gleichungen erhalten werden kann [32].

Abgesehen vom Fall dünner Filme ist es äußerst schwer einen analytischen Einblick in die Fluiddynamik auf mesoskopischer Ebene zu gewinnen. Das gilt insbesondere für die Benetzungsdynamik, bei der eine mobile Fluidgrenzfläche und eine mobile Drei-Phasen-Kontaktlinie vorliegt. Konventionelle Simulationsmethoden, wie numerische Integration der Navier-Stokes-Gleichungen und MD-Simulationen, sind hierbei hinsichtlich der benötigten Rechenkapazitäten sehr ineffektiv. Im Bereich der mesoskopischen Fluiddynamik häufig angewendete, thermische Fluktuationen einschließende Simulationansätze sind daher die *dissipative Teilchendynamik* (dissipative particle dynamics, DPD) und die *Vielteilchen-Kolli- sionsdynamik* (multi-particle collision dynamics, MPD) [33].

Ein auf den *statistischen* Prinzipien der *kinetischen Theorie* beruhender Lösungsansatz für die Navier-Stokes-Gleichungen ist die *Gitter-Boltzmann-Methode* (lattice Boltzmann approach) [34–36]. Diese Methode ist vor allem mit Blick auf die Simulation der Benetz- ungsdynamik von Fluiden sehr interessant, da sie hochgradig parallele Algorithmen und gleichzeitig eine einfache Implementierung komplizierter Randbedingungen erlaubt.

Die Methode basiert auf einer vollständig diskreten Version der Boltzmann-Gleichung, der sogenannten Gitter-Boltzmann-Gleichung, und liefert im Kontinuumslimit den Navier-Stokes-Gleichungen äquivalente, dynamische Gleichungen.

Die Gitter-Boltzmann-Methode hat ihre volle Berechtigung auf der makroskopischen Skala. Bei einer Modifikation der zugrundeliegenden Boltzmann-Gleichung zur *Boltzmann-Enskog-Gleichung*, reicht ihre Anwendbarkeit hinunter zur mesoskopischen Skala. Auf kleineren Skalen wird eine Anwendung problematisch, stattdessen sind dort MD-Simulationen das Mittel der Wahl.

Es existiert eine Reihe von theoretischen Untersuchungen im makroskop. Bereich, sowohl der Benetzungseigenschaften im Gleichgewicht als auch der Fluiddynamik auf chemisch strukturierten Substraten. Dabei geht es beispielsweise um Fragen nach der Bildung spezieller Tröpfchenmorphologien und deren Stabilität, der Dynamik der Drei-Phasen-Kontaktlinie, Entnetzung sowie der Fluiddynamik in dünnen Filmen [21, 37–49].

Vor einigen Jahren wurde im Rahmen des Kapillarmodells das energetische

Verhalten auf geraden chemischen Kanälen sitzender Flüssigkeitströpfchen durch einen morphologischen Übergang beschrieben [38–41]. Dabei wurde der chemische Kanal durch eine Diskontinuität der Benetzbarkeit, bzw. einen zwischen lyophilen und lyophoben Plateauwerten springenden Kontaktwinkel definiert.

Dieser morphologische Übergang wurde ebenfalls auf Grundlage des Kapillarmodells in der vorliegenden Arbeit verifiziert und weitergehend untersucht, und zwar für den Fall chemischer Kanäle, die durch einen Benetzbarkeitsgradienten, bzw. ein zwischen den Plateau- werten kontinuierlich verlaufendes Kontaktwinkelprofil definiert sind. Desweitern wurde der morphologische Übergang in der vorliegenden Arbeit durch Simulationen der Benetzungsdynamik bzw. der Relaxation von Flüssigkeitströpfchen auf geraden, durch eine Diskontinuität der Benetzbarkeit definierten, chemischen Kanälen mittels der Gitter-Boltzmann Methode qualitativ verifiziert.

Der morphologische Übergang eines Flüssigkeitströpfchens spielt eine Rolle, wenn das Tröpfchen entlang eines chemischen Kanals geführt wird, dessen laterale Translationsinvarianz in einer bestimmten Art und Weise gebrochen ist. Durch eine quasi-statische Betracht- ung im Rahmen des Kapillarmodells wurde dies in der vorliegenden Arbeit am Beispiel einer Verzweigung chemischer Kanäle gezeigt. Die genannten Untersuchungen auf der Basis des Kapillarmodells und der Gitter-Boltzmann-Methode sowie deren Ergebnisse sind in den Abschnitten 4.1 und 4.2 des Kapitels 4 dargestellt und beschrieben. Das Kapillarmodell, die Gitter-Boltzmann Methode sowie die zugrundeliegende kinetische Theorie sind in den ersten drei Kapiteln der Arbeit beschrieben. Der Abschnitt 4.2 enthält zudem Daten aus Gitter-Boltzmann-Simulationen zum

Verhalten von Flüssigkeitströpfchen auf geraden und verzweigten chemischen Kanälen unter dem Einfluß treibender Trägheitskräfte. Diese Daten stammen aus zur Zeit der Abfassung dieser Arbeit noch laufenden Untersuchungen und haben somit nicht den Rang von endgültigen Ergebnissen. Gleichwohl sind sie als Diskussionsgrundlage geeignet und wurden daher in die Arbeit aufgenommen.

Eine interessante und in einer Reihe von theoretischen und experimentellen Arbeiten untersuchte Erscheinung auf der mesoskopischen Ebene ist die *Entnetzung* geschlossener Flüssigkeitsfilme auf homogenen Substraten [50–55].

Unter gewissen Bedingungen existieren in einem mesoskopischen Höhenbereich über der Substratoberfläche verschiedene Höhenregime, in welchen Flüssigkeitsfilme energetisch entweder stabil, instabil oder metastabil sind. Die *Spinodale Entnetzung* bedeutet in einem solchen Fall den fluktuationsbedingten Kollaps energetisch instabiler Filme und das anschliessende Wachstum von Löchern in denselben bis hin zur Bildung mesoskopischer Tröpfchen. Energetisch metastabile Filme können ein analoges Schicksal erleiden, wobei hier der Filmkollaps einer Nukleation bedarf.

In der Theorie sind diese Entnetzungsphänomene durch das effektive Grenzflächenpotential bestimmt, d.h. die obengenannten Höhenregime stabiler, instabiler und metastabiler Filme ergeben sich aus dem Verlauf des effektiven Grenzflächenpotentials als Funktion der lokalen Filmhöhe über dem Substrat. Anhand einer generischen Form des effektiven Grenz- flächenpotentials wurden in der vorliegenden Arbeit die Morphologie sowie die energeti- sche Stabilität mesoskopischer Tröpfchen auf homogenen Substraten untersucht. Gegenstand zukünftiger Untersuchung in diesem Zusammenhang sind durch eine entsprechende Topologie des effektiven Grenzflächenpotentials gekennzeichnete, chemisch strukturierte Substrate.

Die Untersuchung mesoskopischer Tröpfchen ist im Kapitel 5 dargestellt, während die dem effektiven Grenzflächenpotential zugrundeliegende Theorie im ersten Kapitel zu finden ist. Die im Rahmen dieser Arbeit erzielten und in den Kapiteln 4 und 5 dargestellten und beschriebenen Ergebnisse sind zur Veröffentlichung in physikalischen Fachzeitschriften vorgesehen.

Introduction

Wetting phenomena are a daily experience. One may, e.g., think of dew drops sitting on plant leaves in the morning, olive oil spreading in a coated frying pan, or adherent rain drops at the underside of a balustrade.

The scientific interest in wetting phenomena dates back to the work of *Young* and *Laplace* in the early nineteenth century [1–3]. It was Young who explained the contact angle of sessile liquid droplets on solid substrates via a force balance at the three-phase contact line, and Laplace related the interfacial curvature of such droplets to the tension on and the pressure jump across their interface. Later on it was Gauss, who firstly investigated the morphology of liquid interfaces by means of a minimization principle [4]. The work of Young, Laplace, and Gauss leads to the so-called *capillary model*, in which wetting phenomena follow from the variation of a phenomenological free energy functional associated with a system of fluid phases, e.g., liquid and gas, in the presence of a solid substrate. Nowadays, wetting phenomena are traced back to an interplay of molecular interactions among the fluid molecules and between fluid molecules and the substrate, accompanied by entropic effects due to fluctuating fluid-fluid interfaces [5].

The subject of this thesis are theoretical investigations on the wetting behaviour of *simple fluids* on planar, *chemically patterned substrates.* The characteristic simple means that the fluids are supposed to be made up of particles without any orientational or internal degrees of freedom. The investigated fluid systems consist of different phases or components, e.g., liquid droplets surrounded by a gaseous phase or droplets of oil surrounded by water. The chemical patterning of the substrate becomes manifest in different wettability domains on the substrate surface. Domains of high wettability, where a certain fluid preferentially adsorbs, thereby are called *lyophilic* with respect to the so-called *lyophobic* domains of low wettability. The microscopic origin of lyophilic and lyophobic domains are the chemical properties of the substrate particles, which lead to a certain range and strength of the fluid-substrate interaction potential.

In addition to that, the wetting behaviour can be influenced significantly by a topological structure of the substrate - a well-known example is the so-called *Lotus effect* [6] - and gravity may exert an impact on the morphology of fluid-fluid interfaces. In the frame of this thesis, substrates are considered to be planar, i.e., they do not have any topological roughness significant for the wetting behaviour. Further, gravitational effects are neglected. This corresponds to a situation in which the characteristic spatial dimensions of an investigated fluid system are sufficiently far below the so-called *capillary length*, i.e., the length scale at which gravitation significantly affects the morphology of fluid-fluid interfaces.

Chemically patterned substrates open interesting new perspectives in the field of *microfluidics*. As the name implies, microfluidics deals with the control of fluid behaviour on the scale of microns. Since the capillary length of most fluids is of the order of a few *mm*, gravitational effects generally do not play any role in microfluidics. By means of striped lyophilic surface domains in an otherwise lyophobic proximity, so-called *chemical channels*, it is possible to guide liquid over planar solid substrates. Based on this phenomenon, arrangements of micron-sized lyophilic patterns in a lyophobic proximity, forming, e.g., fluid reservoirs, transport channels, mixing or reaction areas, could be combined to so-called *open microfluidic devices*. Fluid transport on such devices could be managed by body-forces, wettability-gradients, or shear-flow. This directly leads to a technologically relevant *lab-on-a-chip* concept [7–9], which, in analogy to the integrated circuit of electronic devices on a CPU, integrates a combination of microfluidic devices in a very compact way on a *chemical chip* in order to enable the control of specific chemical and physical processes with much smaller quantities of rare, toxic, or explosive educts and products than standard laboratory equipment.

The main line of development with respect to the lab-on-a-chip concept are so-called *closed microfluidic devices*. These are built up with closed geometrical structures like tubes and chambers, in which fluid flow is controlled by pressure gradients [15]. Since on small scales the effect of boundary conditions gains importance with respect to bulk properties, open microfluidic devices could be a serious alternative to closed systems. The well-known law of *Hagen* and *Poiseuille*, for instance, predicts, that the slip-less, viscous flow of a homogeneous fluid through a tube of given length is proportional to the product of an applied pressure gradient and the tube radius raised to the power of four. Hence, open microfluidic devices given by chemically patterned slit pores or single chemically patterned substrates with an uncovered fluid-fluid interface might be more efficient with respect to fluid transport than closed tubes [10–14]. In addition to that, blockage by solute particles like colloids or large polymers due to an attachment to the walls creates a problem for closed systems, which is supposed to be less serious or even avoided on open devices.

A miniaturization of open microfluidic devices leads towards the nano-scale, i.e., fluid flow has to be controlled on length-scales in the range of 10-10^2 nm [16–18]. The limit for a miniaturization thereby is set by entropic effects due to thermal fluctuations.

There exists a number of methods for the fabrication of chemically patterned substrates on different length-scales. Chemical patterns in the mm-range can be obtained by means of printing or etching techniques. The micron-scale is accessible via micro-contact printing, molecular beam epitaxy through grids, electrophoretic aggregation of colloids, or via stripping of polymer films [19–23]. Techniques like photolithography, local oxidation by means of AFM-tips, and molecular beam epitaxy with light masks are adequate in order to obtain chemical patterns on the nm-range [24–26].

In order to obtain design criteria for open micro- and nanofluidic devices, a sound theoretical description of both, the wetting behaviour in equilibrium and the dynamics of wetting on chemically patterned substrates is necessary. To mark the start of this, one has to think about characteristic length-scales. As already mentioned, these scales in any case are quite far below the capillary length, such that gravity does not matter. In fact, the description has to be based on a reasonable compilation of molecular interactions for a given length-scale regime.

On a macroscopic scale of microns, well above the range of molecular interactions, equilibrium wetting phenomena can be described by means of the abovementioned capillary model. The spatial configuration of a system of two fluids in the presence of a solid substrate thereby is characterized by the fluid-fluid interface, the fluid-substrate interfaces, and a three-phase contact line. These geometrical objects are subject to free energy densities, the so-called *interfacial tensions*, and the so-called *line tension*. These energy densities indirectly model the effect of the underlying molecular interactions, which are very short in range on the macroscopic scale. The configuration of minimal integrated free energy for given fluid volumes or a given difference of the fluid bulk pressures then defines the overall curvature of the fluid-fluid interface as well as the macroscopic contact angle at the three-phase contact line. Accordingly, in the frame of the capillary model chemically patterned substrates are characterized by a variation of the contact angle, whereupon lyophilic and lyophobic domains have contact angles below and above $\pi/2$, respectively

On the microscopic scale of a few nm, on which the range of molecular interactions is quite long, the corresponding interaction potentials have to be incorporated explicitely into the description. In a microscopic *density functional* *theory*, the interaction potentials enter into a functional of the particle density, which gives the free energy of the system. The equilibrium configuration of the system then is characterized by smoothly varying density profiles minimizing the free energy functional. Accordingly, instead of interfaces and a three-phase contact line, i.e., geometrical objects without an intrinsic structure, there exist three-dimensional interfacial domains with an inherent structure given by equilibrium density profiles.

With respect to the miniaturization of microfluidic devices, the understanding of fluid behaviour in the intermediate regime between the micron- and the nano-scale, termed the *mesoscopic scale*, is of great importance. Based on the assumption that the inherent structure of an interfacial domain is not significant on this scale, the underlying concepts of the microscopic density functional theory and the macroscopic capillary model can be merged in order to account for the effect of long-ranged molecular interactions [5, 27–29]. The wetting behaviour in this regime is determined by a so-called *effective interface potential*, which models the effective interaction of the fluid-fluid interface with the substrate as a function of the local interfacial height. Chemical patterns in this case are encoded in a certain topology of the effective interface potential.

Fluid flow on the macroscopic scale, and hence, the dynamics of wetting, in principle is governed by the *Navier-Stokes equations.* In analogy to the capillary model, the effect of microscopic interactions thereby is taken indirectly into account via the viscosity and the thermal conductivity, the so-called transport coefficients, and via the kinematic boundary conditions at interfaces.

Amending the Navier-Stokes equations with long-ranged fluid-substrate interactions and fluid-dynamic slip at the substrate leads to meso-scale fluid dynamics. An important analytic tool in meso-scale fluid dynamics is the so-called lubrication approximation, which leads to an evolution equation for thin films [32]. The thin film equation has been used in the context of dewetting, stability of fluid rivulets on chemical channels, and the influence of thermal fluctuations on thin film flow [30, 31, 51–53]. Apart from the thin film case, it is highly non-trivial to get analytic insight into meso-scale fluid dynamics. On the other hand, conventional simulation methods like the numerical integration of the Navier-Stokes equation and MD-simulations make high demands on computational resources. Investigations of meso-scale fluid dynamics thus are mainly based on simulation techniques like *dissipative particle dynamics*, and *multi-particle collision dynamics*, which take into account thermal fluctuations [33].

An efficient solver for the Navier-Stokes equations with moving interfaces, based on the statistical concepts of kinetic theory, is the *lattice Boltzmann approach* [34–36]. Using a fully discrete version of the continuous Boltzmann equation[1], called the lattice Boltzmann equation, this approach models Navier-Stokes dynamics on a scale large compared to the periodicity of the positional lattice. The approach applys for dilute fluids on macroscopic scales. By means of a modification of the underlying Boltzmann equation, known as the *Boltzmann-Enskog equation*, the applicability of the lattice Boltzmann approach can be extended to more dense fluids on the mesoscopic scale [56, 57]. The approach is inappropriate to model nano-scale fluid flow. In order to do so, MD-simulations are the best way. Within its range of applicability, the lattice Boltzmann approach is a very powerful method since, on the one hand, it allows for very efficient, highly parallel algorithms, in which even complex geometries can be implemented quite easily, and on the other hand, it relates the transport coefficients within the fluid-dynamic level equations to quantities defined on the kinetic level.

---

[1] discrete in time, positional degrees of freedom, and velocity degrees of freedom

There exists a number of theoretical investigations on the macroscopic scale dealing with both, equilibrium fluid properties and fluid flow on chemically patterned substrates, addressing problems like the formation of droplet morphologies and their stability, contact line motion, and thin film flow [21, 37–49].

Quite recently, equilibrium properties of sessile liquid droplets on straight chemical channels have been described in the frame of the capillary model [38–41]. The chemical channel thereby was defined by a step-like variation of the wettability, i.e., a jump of the contact angle between lyophilic and lyophobic plateau values. It turned out, that the energetic behaviour of sessile droplets in this case corresponds to a morphologic transition.

Within this thesis, the morphologic transition of sessile droplets on straight chemical channels has been verified and investigated further for the case of contact angle profiles smoothly evolving between lyophilic and lyophobic plateau values. As expected, the morphologic transition strongly depends on the smoothness of the profiles. Further, simulations of the relaxation dynamics of droplets on straight chemical channels in three dimensions have been performed by means of the lattice Boltzmann approach, which give a qualitative verification of the morphologic transition.

The morphologic transition plays a role if the droplets are guided along channels with a broken translation invariance. By means of a quasi-static picture based on the capillary model this has been shown within this thesis for a droplet guided through a junction of chemical channels.

A presentation of the abovementioned investigations is given in chapter 4, whereas the capillary model, the lattice Boltzmann approach, and the underlying kinetic theory are presented in the preceding chapters. Chapter 4 additionally contains a presentation of lattice Boltzmann simulation data on body-force-driven sessile droplets on straight and branched chemical channels. Since this is work still in progress, these data are presented as a matter of discussion, rather than being final results.

An interesting effect on the mesoscopic level investigated both, theoretically and experimentally [50, 54, 55], is the *dewetting* of extended fluid films on homogeneous substrates. Under certain conditions there are different regimes within a mesoscopic height range above the substrate surface, in which wetting films are energetically either stable, or unstable, or metastable. *Spinodal dewetting* in this case means the fluctuation induced collapse of an energetically unstable film, which is followed by a growth of film holes finally leading to a set of mesoscopic droplets. Induced by a nucleation of holes, the analogue happens in case of energetically metastable films. The dewetting process is triggered by the effective interface potential, i.e, the abovementioned height regimes for stable, unstable, and metastable films follow from the latter as a function of the local interfacial film height above the substrate.

Mesoscopic droplets arising by reason of a dewetting process under the impact of the effective interface potential are interesting configurations since in some sense they constitute the in-between of a droplet and a thin film. Based on a generic potential form, the morphology and the energetic stability of mesoscopic droplets on a homogeneous substrate has been investigated within this thesis. A future perspective would be to extend these investigations to chemically patterned substrates.

The investigations on mesoscopic droplets are presented in chapter 5. The theoretical approach leading to the formulation of the effective interface potential followed by a description of the generic potential form which triggers dewetting is presented in the first chapter.

The results obtained in the frame of this thesis, as presented in the chapters 4 and 5, are designated for publication in scientific journals.

Symbols and Notations

The meaning of symbols and notations is supposed to be clear either by immediate explanation, or from the context they appear in, or via explicit reference to basic definitions and expressions in the frame of this thesis. The usual list therefore has been abandoned.

Chapter 1

Fluids in Equilibrium

In the following, the theoretical framework for an investigation of wetting morphologies on solid substrates is presented.

Down to the mesoscopic scale, a wetting morphology is defined as the shape of the interface $\mathcal{A}$, separating two non-volatile fluid phases in contact with a solid substrate. The mechanically stable equilibrium of the interface (not necessarily going along with the thermodynamic equilibrium) corresponds to a minimum value of the interfacial free energy

$$\tilde{F} \ := \ \oint_{\mathcal{A}} dA \ \sigma(\mathbf{r}_{\mathcal{A}}) \quad ,$$

where σ denotes the interfacial free energy density depending on the spatial coordinates $\mathbf{r}_{\mathcal{A}}$ on the interface $\mathcal{A}$. The most general and well known case of a wetting morphology is a liquid droplet surrounded by a gas sitting on a solid substrate. In this case the interface $\mathcal{A}$ is a closed surface consisting of a fluid-fluid and a fluid-substrate interfacial part, and the fluid and solid phases share a boundary line, the so-called three-phase contact line.

From a universal, microscopic point of view, the formation of a specific wetting morphology is the result of both, an interplay of molecular interactions among the components of the system, and the action of external forces on the system. Accordingly, there exist different length-scales at which a wetting morphology has specific characteristics depending on the relative strength of the above mentioned interactions.

The ratio of the interfacial free energy density σ created by molecular interactions versus the density of external forces f_{ext} defines the capillary length,

$$l_{\mathrm{cap}} := \sqrt{\sigma / f_{\mathrm{ext}}} \quad . \tag{1.1}$$

The capillary length sets the scale at which the effect of external forces on the wetting morphology has to be taken into account. It plays the role of a screening length in the sense, that perturbations on a fluid-fluid interface due to an interplay of molecular interactions and external forces die out exponentially over the distance l_{cap}. Hence, in the limit

$$V / l_{\mathrm{cap}}^3 \ll 1 \quad , \tag{1.2}$$

where V is the volume of the wetting phase[1], the effect of external forces can be neglected.

---

[1] in case of a liquid droplet on a solid substrate surrounded by gas, the liquid would be the wetting phase.

Within the limit given by (1.2), two regimes may be distinguished. The first one is the macroscopic regime characterized by the relation

$$l_{\mathrm{cap}} \gg l \gg l_0 \quad , \tag{1.3}$$

i.e., the characteristic morphologic length-scale l is well below the capillary length, but still well above the range l_0 of molecular interactions. This means that the different interfaces within the system are well separated from each other in units of l_0. Then, to a very good approximation, the effects of adhesive and cohesive molecular interactions within the different phases result in constant interfacial free energy densities, aka interfacial tensions, and wetting morphologies form due to an interplay of the latter. An important characteristic of this limit is a well defined three-phase contact line at which the fluid phases and the substrate meet under a certain macroscopic contact angle. These are the main features of the *capillary model* [58–62], presented in a more detailed description within section 1.1.

The second, mesoscopic regime is characterized by the relation

$$l_{\mathrm{cap}} \ggg l \gtrsim l_0 \gg l_{\mathrm{mol}} \quad , \tag{1.4}$$

where l_{mol} is the average separation of fluid molecules, i.e., the characteristic length-scale l is of a similar or even the same order as the range l_0 of molecular interactions, which are long-ranged with respect to l_{mol}. Within this regime, extensive parts of the fluid-fluid interface now come close to the substrate in units of l_0, and hence, the fluid-fluid interfacial free energy depends on the net effect of molecular fluid-fluid and fluid-substrate interactions. This can be accounted for by means of an effective interface potential, which models the effective interaction of the fluid-fluid interface with the substrate as a function of the local interfacial height [28, 29, 63]. The concept of an effective interface potential is based on a microscopic density functional theory [5, 64] and will be described within section 1.2.

Both, the macroscopic capillary model, and the mesoscopic effective interface potential deal with sharp fluid-fluid interfaces to be parameterized as two-dimensional mathematical manifolds. As a consequence, physical quantities like pressure and densities discontinuously jump across an interface and the wetting behaviour results from boundary conditions on the interface and at the three-phase contact line. While this approach is fully justified in the limit (1.3), the general situation described by the microscopic density functional theory is the formation of a fluid-fluid interfacial region characterized by a smoothly varying density profile. However, the effective interface potential simply captures the leading asymptotic behaviour of the underlying density functional theory, which indeed is independent of the intrinsic structure of the fluid-fluid interfacial region [63].

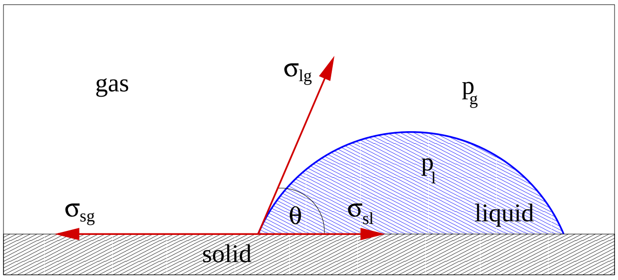

Figure 1.1: Depiction of Young 's law, which relates the liquid-gas, solid-liquid, and solid-gas interfacial tensions, σ_{lg}, σ_{sl}, and σ_{sg}, respectively, to the macroscopic contact angle θ. The interfacial tensions can be seen as forces per unit lenght acting on the three-phase contact line.

1.1 The capillary model

As already mentioned above, within the macroscopic capillary model molecular interactions are summarized into conditions at the phase boundaries, i.e, the fluid-fluid interface and the three-phase contact line. The model explains the formation of wetting morphologies by means of an interplay of constant interfacial tensions acting on the fluid-fluid and solid-fluid interfaces and a line tension acting on a continuous three-phase contact line, where the interfaces meet under a certain contact angle. Line tension effects generally are considered insignificant, hence, they are not taken into account in the following.

Based on the assumption that the interfacial tensions are given, the capillary model relates the resulting physical behaviour of the system to its morphologic topology, i.e, the claim for a mechanical equilibrium of both, the fluid-fluid interface, and the three-phase contact line yields the boundary conditions, which relate the interfacial tensions, the pressure jump across the fluid-fluid interface, the curvature of the fluid-fluid interface, and the contact angle at the three-phase contact line to each other.

The capillary model by itself may be seen as a phenomenological, macroscopic approach with the interfacial tensions as input parameters. However, it constitutes the macroscopic border case of the more fundamental density functional theory, whereat the interfacial tensions and the line tension are related to the underlying molecular interactions.

The interfacial free energy

The mechanical equilibrium of the fluid-fluid interface and the three-phase contact line is expressed by means of vanishing first variations of a free energy, which directly lead to the abovementioned boundary conditions.

The free energy F of a system of two fluids (say, liquid and gas) sharing a three-phase contact line with a solid substrate is given as a functional of the liquid volume V_l, the solid-liquid interfacial area A_{sl} and the liquid-gas interfacial area A_{lg} (with surface elements dA_{sl} and dA_{lg}, respectively), i.e.,

$$F \;=\; \underbrace{\int dA_{lg}\;\sigma_{lg} \;+\; \int dA_{sl}\;(\sigma_{sl}-\sigma_{sg})}_{:=\tilde{F}} \;-\; \Delta p \int dV_l \quad . \tag{1.5}$$

The interfacial free energy $\tilde{F}$ contains the interfacial tensions σ_{sl}, σ_{sg}, and σ_{lg}, between solid and liquid, solid and gas, and liquid and gas, respectively. The interfacial areas A_{lg} and A_{sl} are bounded by the three-phase contact line, and the pressure jump across the liquid-gas interface, $\Delta p := p_l - p_g$, defines the so-called Laplace pressure.

Wetting

A wetting morphology has been defined as the configuration of the liquid-gas interface A_{lg} which for a given volume V_l minimizes the interfacial free energy $\tilde{F}$, i.e, both, the liquid-gas interface, and the three-phase contact line have to be in mechanical equilibrium. The corresponding conditions follow from the first variation of the free energy F.

▷ The first variation of F with respect to the liquid-gas interface A_{lg} and the liquid volume V_l for a fixed three-phase contact line $\mathcal{L}_{slg}$,

$$(\delta^{(1)}_{A_{lg},V_l} F)_{|\mathcal{L}_{slg}} \; = \; \int dA_{lg} \; (2\sigma_{lg} M - \Delta p) \, \psi \quad , \tag{1.6a}$$

yields the mechanical equilibrium condition for the liquid-gas interface A_{lg} ,

$$\Delta p \; = \; 2\sigma_{lg} M \quad . \tag{1.6b}$$

This is know as the Laplace equation, which states that in mechanical equilibrium the liquid-gas interface A_{lg} is characterized by a constant mean curvature M.

- ▷ The first variation of F with respect to the interfacial areas A_{sg} and A_{sl} for a fixed liquid volume V_l ,

$$(\delta^{(1)}_{A_{sg},A_{sl}}F)_{|V_l} \;=\; \sigma_{lg}\int_{\mathcal{L}_{slg}} dl\, \left(\cot\theta - \frac{\sigma_{sg}-\sigma_{sl}}{\sigma_{lg}\sin\theta}\right)\psi \quad , \tag{1.7a}$$

  yields the mechanical equilibrium condition for the three-phase contact line $\mathcal{L}_{slg}$,

$$\sigma_{lg}\cos\theta \;=\; \sigma_{sg}-\sigma_{sl} \quad . \tag{1.7b}$$

  This is know as the law of Young, which specifies the mechanical equilibrium of the three-phase contact line by relating the interfacial tensions to the macroscopic contact angle θ, see figure 1.1.

The variations have been carried out by means of suitable scalar displacement fields ψ defined on A_{lg} and $\mathcal{L}_{slg}$, respectively, and the three-phase contact line $\mathcal{L}_{slg}$ has been parameterized by means of its arc lenght l [38, 41].

The first variations (1.6a) and (1.7a) do not allow to determine the stability of a mechanical equilibrium, i.e., whether the morphology of A_{lg} corresponds to a local energetic maximum, a minimum, or a saddle point. This follows from the definiteness of the second variation of the free energy, which is a quadratic form with respect to the displacement field ψ.

From equations (1.6b) and (1.7b) it follows that the wetting morphology on a planar, homogeneous substrate is given by a spherical cap meeting the substrate at an angle θ. Hence, the macroscopic contact angle θ is the parameter the capillary model provides in order to specify the degree of wetting and to make some qualitative statements on the average ratio of the molecular interactions

- ▷ In the case of adhesive liquid-substrate interactions which are predominant compared to cohesive liquid-liquid interactions, the contact angle θ may approach very small values close zero degrees. The limiting case $\theta = 0$ is called perfect wetting or complete wetting.
- ▷ In the case of predominant cohesive fluid-fluid interactions, the contact angle θ on planar substrates may approach large values[2] up to 150°. This case it called non-wetting.
- ▷ If adhesive liquid-substrate and cohesive liquid-liquid interactions are of the same order of magnitude, the contact angle is about 90°.

According to that, one can define the regime of high wettability by $0^\circ < \theta < 90^\circ$ and the regime of low wettability by $90^\circ \leq \theta < 180^\circ$. Alternatively, the degree of wetting can be specified by means of the so-called spreading parameter

$$S \;:=\; \sigma_{sg} - (\sigma_{sl} + \sigma_{lg}) \;=\; \sigma_{lg}\,(\cos\theta - 1) \quad , \tag{1.8}$$

which is defined as the difference in the interfacial free energy of the system in case of a completely dry or a completely wet substrate. It measures the degree of wetting such, that $S < 0$ corresponds to partial wetting, whereas total wetting means $S \nearrow 0$. The spreading parameter is related to the macroscopic contact angle θ via Young 's law (1.7b).

---

[2] values up to 180° can be reached on structured, super-hydrophobic substrates

1.2 Microscopic density functional theory

In the capillary model intermolecular interactions are taken into account in terms of interfacial and line tensions. This was justified by the fact that the model applies on lenghtscales well above the range l_0 of molecular interactions. On length-scales of the order of l_0 a so-called effective interface potential can be introduced, which, based on a microscopic density functional theory, accounts for the net effect of fluid-substrate and fluid-fluid interactions on the wetting morphology. [5, 28, 29, 63–65].

The grand canonical density functional

In the framework of density functional theory, a thermodynamic potential is expressed as a functional of a spatial density distribution and in the Hilbert space of allowed distributions the equilibrium distribution therefore is the one which minimizes the functional. The grand canonical density functional $\Omega[\varrho(\mathbf{r})]$ for an inhomogeneous fluid which is characterized by the number density $\varrho(\mathbf{r})$ reads

$$\begin{aligned}\Omega[\varrho(\mathbf{r}),T,\mu] \;&=\; \int_V d^3r\; f_{HS}\left(\varrho(\mathbf{r}),T\right) \;+\; \int_V d^3r\;\left[W(\mathbf{r})-\mu\right]\,\varrho(\mathbf{r}) \\ &\quad+\frac{1}{2}\int_{V'}\int_V d^3r d^3r'\; w(|\mathbf{r}-\mathbf{r}'|)\,\varrho(\mathbf{r})\varrho(\mathbf{r}') \quad . \qquad (1.9)\end{aligned}$$

The range of integration is given by the volume V of a system of liquid and vapour. $W(\mathbf{r})$ is the substrate potential, i.e., the fluid-substrate pair interaction integrated over the region occupied by the substrate, and μ is the chemical potential. The long-ranged attractive part of the fluid-fluid pair interaction within the system is modeled by the potential $w(|\mathbf{r}-\mathbf{r}'|)$, whereas the repulsive part at short ranges is taken into account via the bulk free energy density $f_{HS}\left(\varrho(\mathbf{r}), T\right)$ of a hard sphere fluid in a local approximation.

The density functional $\Omega[\varrho(\mathbf{r})]$ is minimized by the equilibrium density distribution $\varrho_0(\mathbf{r})$, which in the fluid-fluid interfacial region in principle is a function smoothly varying between the number densities ϱ_l and ϱ_g of the liquid and gas bulk phases, respectively. Neglecting the intrinsic structure of the diffuse fluid-fluid interface corresponding to such a density profile, one can apply the so-called *sharp-kink approximation*, which implies that $\Omega[\varrho(\mathbf{r})]$ is minimized within the subspace of steplike varying density profiles.

On a flat substrate the density is then given by

$$\varrho(\mathbf{r})_{sk} := \Theta(z - h_{\text{ex}}) \left\{ \varrho_l \Theta\left(h(\mathbf{R}_{\|}) - z\right) + \varrho_g \Theta\left(z - h(\mathbf{R}_{\|})\right) \right\} \quad , \qquad (1.10)$$

where $z = h(\mathbf{R}_{\|})$ is the local height of the liquid-gas interface with respect to lateral coordinates $\mathbf{R}_{\|}$ on the substrate. The above parameterization for the local interfacial height is valid if no overhangs are present. The level h_{ex} accounts for the excluded volume near the substrate due to the repulsive part of the fluid-substrate interaction $W(\mathbf{r})$ and Θ is the Heaviside function.

Inserting the expression (1.10) into (1.9), applying a small gradient expansion, and assuming that the system is close to the liquid-gas coexistence, one obtains a local approximation for the grand canonical free energy as a functional of the liquid-gas interface morphology $h(\mathbf{R}_\parallel)$,

$$\Omega[h(\mathbf{R}_\parallel)] = \int_{A_{sl}} d^2R_\parallel \, \Big\{ \sigma_{lg}\sqrt{1+|\nabla_\parallel h|^2} \,+\, \Delta\mu\Delta\varrho\, h(\mathbf{R}_\parallel) \,+\, \phi\left(h(\mathbf{R}_\parallel)\right) \Big\} + C \quad , \tag{1.11}$$

where A_{sl} denotes the solid-liquid interface, $\nabla_\parallel h$ denotes the two-dimensional gradient with respect to the lateral coordinates, and the constant C contains all terms independent of $h(\mathbf{R}_\parallel)$. The deviation from phase coexistence is given by $\Delta\mu = \mu_0(T) - \mu$, where $\mu_0(T)$ describes the liquid-gas coexistence line and $\Delta\varrho := \varrho_l - \varrho_g$ is the difference of the bulk densities.

Within the sharp-kink approximation, the interactions in the system give rise to the liquid-gas interfacial tension

$$\sigma_{lg} = -\frac{1}{2}(\Delta\varrho)^2 \int_0^\infty dz \; t(z) \tag{1.12a}$$

and the effective interface potential

$$\phi(h) = \Delta\varrho \left\{ \varrho_l \int_{h-h_{\mathrm{ex}}}^\infty dz \; t(z) - \int_h^\infty dz \; W(z) \right\} \quad . \tag{1.12b}$$

In the expressions (1.12a) and (1.12b), the interaction potential of a fluid particle at z with the space above z occupied by fluid particles is

$$t(z) = \int_z^\infty dz' \int_{\mathbf{R}_\parallel} d^2R_\parallel \; w(|\mathbf{r}-\mathbf{r}'|) \quad .$$

The effective interface potential $\phi(h)$ (1.12b) captures the net effect of the long-ranged fluid-fluid pair interactions given by $w(|\mathbf{r}-\mathbf{r}'|)$ and fluid-substrate interactions given by $W(z)$. It measures an effective energy density on the liquid-gas interface $h(\mathbf{R}_{||})$ due to the presence of the substrate, in other words, an effective interaction between the substrate and an interface with a local height profile $h(\mathbf{R}_{||})$.

The effective interfacial free energy

Inspired by the expression (1.11) for the local approximation of the grand canonical free energy, the effective free energy $\mathcal{F}$ of non-volatile liquid surrounded by a gas phase in contact with a planar substrate is written as

$$\mathcal{F} \;=\; \underbrace{\int_{A_{sl}} d^2R_{||} \left\{ \sigma_{lg}\sqrt{1+|\nabla_{||}h|^2} \,+\, \phi\left(h(\mathbf{R}_{||})\right) \right\}}_{:=\tilde{\mathcal{F}}} \;-\; \Delta p \int_{A_{sl}} d^2R_{||}\; h(\mathbf{R}_{||}) \quad . \tag{1.13}$$

The range of integration is the solid-liquid interface A_{sl}, the liquid-gas interfacial profile is given by the parameterization $h(\mathbf{R}_{||})$, where $\mathbf{R}_{||}$ denotes lateral coordinates in the substrate plane, and the two-dimensional gradient with respect to the lateral coordinates is denoted by $\nabla_{||}$.

The interfacial part $\tilde{\mathcal{F}}$ incorporates the liquid-gas interfacial tension σ_{lg} and the effective interface potential $\phi(h)$, whereas the bulk part is given by the Laplace pressure Δp times the integrated liquid volume. The expression (1.11) can be seen as an extension of the phenomenological, macroscopic interface displacement model [63, 66] towards the mesoscopic scale.

The variation problem of the effective free energy $\mathcal{F}$ (1.13) seen as a functional of the lateral coordinates $\mathbf{R}_{||}$ yields the Euler-Lagrange equation,

$$\Delta p + \Pi(h) + \sigma_{lg} \nabla_{||}^2 h \overset{!}{=} 0 \quad , \tag{1.14}$$

which is the constraint on the equilibrium profile $h_0(\mathbf{R}_{||})$. The so-called disjoining pressure $\Pi(h)$ is defined by the relation

$$\Pi(h) := -\partial_h \phi(h) \quad . \tag{1.15}$$

Within (1.13) the liquid-gas interfacial tension σ_{lg} is supposed to be independent of the lateral coordinates $\mathbf{R}_{||}$ and therefore it serves as a scaling parameter for the free energy per unit surface area.

Wetting

The wetting behaviour of a system described by the effective free energy $\mathcal{F}$ (1.13) is determined by the analytic properties of the effective interface potential $\phi(h)$. In case of Lennard-Jones like fluid-fluid interactions the effective interface potential has an algebraic form,

$$\phi(h) = \sum_{j \geq 2} a_j \, h^{-j} \quad , \tag{1.16}$$

where a_2 is known as the Hamaker constant. The figure 1.2 shows a generic potential $\phi(h)$ and the corresponding disjoining pressure $\Pi(h)$ for a partially wetting substrate.

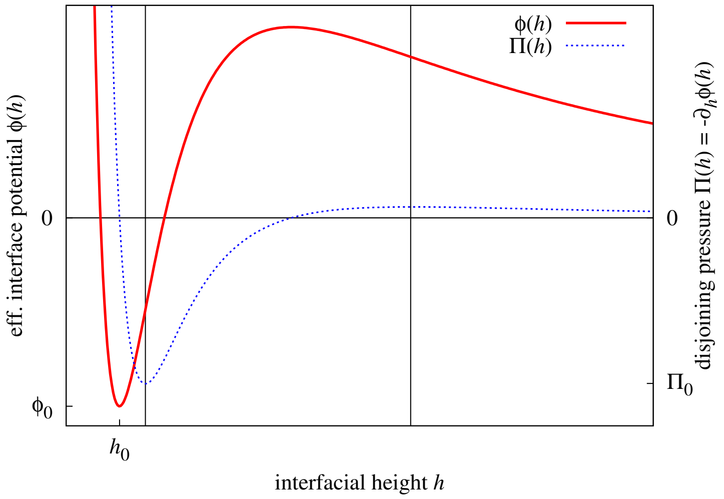

Figure 1.2: Generic form of the effective interface potential $\phi(h)$ and the disjoining pressure $\Pi(h) := -\partial_h \phi(h)$ as a function of the interfacial height h for a partially wetting substrate.

The characteristic mesoscopic scale is given by the height h_0 at which the effective interface potential attains its global minimum ϕ_0. According to the Euler-Lagrange equation (1.14), the Laplace pressure vanishes on the level h_0,

$$\Delta p \;\equiv\; -\Pi_{|h_0} = 0 \quad .$$

Hence, h_0 is the height of a stable equilibrium film at liquid-vapour coexistence.

The height range in-between the two inflection points is characterized by a negative curvature, $\partial_h^2\,\phi(h) < 0$, which means that $\Pi(h)$ increases for increasing heights h. Within this range, wetting films are unstable and spinodal dewetting [5, 67] occurs. This means that an exponential growth of infinitesimal perturbations of the film surface, e.g., generated by thermal fluctuations, leads to a film rupture and finally the formation of droplets. The repulsive tail beyond the second inflection point, where $\partial_h^2\,\phi(h) > 0$, allows for metastable films since a nucleation of holes is necessary in order to induce dewetting.

Following (1.14), the droplets which constitute the final state of the dewetting process are characterized by a non-trivial local balance of a non-vanishing Laplace pressure $\Delta p > 0$, the disjoining pressure $\Pi(h)$, and the curvature term $\sigma_{lg}\nabla_{\|}^2 h$. Due to the fact that the potential diverges at very small interfacial heights, $\phi(h \to 0) \nearrow \infty$, the droplets are not surrounded by dry substrate areas, instead, they are floating on a thin film with a height $\tilde{h}$ determined by a balance of the Laplace pressure and the disjoining pressure,

$$\Delta p \equiv -\Pi_{|\tilde{h}} \quad . \tag{1.17}$$

Based on mechanical equilibrium arguments, the depth $\phi_0 < 0$ of the effective interface potential can be related to an effective contact angle $\tilde{\theta}$ defined at the intersection of the level h_0 and an approximated sessile height profile, i.e.,

$$\phi_0 \;=\; \sigma_{lg}\left(\cos\tilde{\theta} - 1\right) \quad . \tag{1.18}$$

The expression (1.18) is congruent with the spreading parameter S (1.8) for the partial wetting case. In the limit of macroscopic droplets where $h_0 \to 0$, the effective contact angle $\tilde{\theta}$ asymptotically approaches the macroscopic contact angle θ. In this sense, the generic potential $\phi(h)$ in figure 1.2 corresponds to a partially wetting substrate. Contrary to the capillary model, metastable wetting films exist due to the repulsive tail of $\phi(h)$ for any depth $\phi_0 < 0$, and hence, for any possible contact angle.

1.3 Minimization of the free energy

In the preceding sections, the description of wetting in solid-liquid-gas systems on different length-scales has been based on suitable expressions for the free energy. Wetting morphologies have been specified by interfacial profiles which minimize the interfacial part of these expressions under the constraint of a constant enclosed volume. In the following, some technical aspects of the constrained minimization are explained.

Within the macroscopic limit (1.3) governed by the capillary model, the free energy F (1.5),

$$F \;=\; \underbrace{\int dA_{lg}\,\sigma_{lg} \;+\; \int dA_{sl}\,(\sigma_{sl}-\sigma_{sg})}_{:=\tilde{F}} \;-\; \Delta p \int dV_l \quad , \tag{1.19}$$

with the interfacial part $\tilde{F}$ has been given, and, as a measure of the degree of wetting, the spreading parameter S (1.8) has been defined,

$$S \;:=\; \sigma_{sg} - (\sigma_{sl}+\sigma_{lg}) \;=\; \sigma_{lg}\,(\cos\theta - 1) \quad , \tag{1.20}$$

related to the macroscopic contact angle θ.

Within the mesoscopic limit (1.4), the effective free energy $\mathcal{F}$ (1.13),

$$\mathcal{F} \;=\; \underbrace{\int_{A_{sl}} d^2R_{\|}\left\{\sigma_{lg}\sqrt{1+|\nabla_{\|}h|^2} \;+\; \phi\left(h(\mathbf{R}_{\|})\right)\right\}}_{:=\tilde{\mathcal{F}}} \;-\; \Delta p \int_{A_{sl}} d^2R_{\|}\;h(\mathbf{R}_{\|}) \quad , \tag{1.21}$$

has been given, inspired by the local approximation (1.11) of a microscopic density functional. The depth ϕ_0 of the effective interface potential $\phi(h)$ at a finite level h_0 plays the role of a spreading parameter, i.e.,

$$\phi_0 \;=\; \sigma_{lg}\left(\cos\tilde{\theta} - 1\right) \quad , \tag{1.22}$$

where the so-called mesoscopic contact angle $\tilde{\theta}$ corresponds to a droplet floating on a surrounding film with a certain height $\tilde{h} > h_0$ determined by the balance $\Delta p \equiv \Pi_{|\tilde{h}}$.

The numerical minimization of $\tilde{F}$ and $\tilde{\mathcal{F}}$ leading to the wetting morhpologies in the corresponding length-scale regimes is done via a finite element algorithm [68]. Within this algorithm, the interfacial free energy is evaluated on an oriented liquid-gas interface $\mathbf{A}_{lg}$ bounded by the three-phase contact line $\mathcal{L}_{slg}$, whereupon $\mathbf{A}_{lg}$ is represented by a mesh of oriented triangles and $\mathcal{L}_{slg}$ consists of oriented marginal triangle edges. Hence, the interfacial free energies $\tilde{F}$ and $\tilde{\mathcal{F}}$ have to be reformulated such, that the integrations are carried out on $\mathbf{A}_{lg}$ and $\mathcal{L}_{slg}$, respectively.

For the interfacial free energy $\tilde{F}$ (1.19), this means that the energetic contribution of the solid-liquid interface A_{sl} has to be transfered to $\mathcal{L}_{slg}$. Thereto, Young 's law (1.7b) and the circulation theorem of Stokes yield

$$\tilde{F} \;=\; \sigma_{lg}\left\{\int d\mathbf{A}_{lg}\cdot\hat{\mathbf{n}}_{lg} - \oint_{\mathcal{L}_{slg}} d\mathbf{s}\cdot\mathbf{k}\right\} \quad , \tag{1.23a}$$

where $\hat{\mathbf{n}}_{lg}$ is the unit normal on A_{lg}, i.e., $d\mathbf{A}_{lg} = A_{lg}\hat{\mathbf{n}}_{lg}$, and $d\mathbf{s}$ is a vectorial line element of the three-phase contact line $\mathcal{L}_{slg}$. The kernel

$$\mathbf{k} \;=\; x \cos\theta \, \hat{\mathbf{e}}_y \quad . \tag{1.23b}$$

follows from the circulation theorem, i.e., $\nabla \times \mathbf{k} \overset{!}{=} \cos\theta \, \hat{\mathbf{e}}_z$.

The effective interfacial free energy $\tilde{\mathcal{F}}$ (1.21) is reformulated via the relation

$$d\mathbf{A}_{lg} = \begin{pmatrix} -\nabla_{\|} h \\ 1 \end{pmatrix} d^2 R_{\|}$$

for an oriented surface element $d\mathbf{A}_{lg}$. One finds

$$\tilde{\mathcal{F}} \;=\; \sigma_{lg} \int d\mathbf{A}_{lg} \cdot \hat{\mathbf{n}}_{lg} + \int d\mathbf{A}_{lg} \cdot \hat{\mathbf{e}}_z \, \phi_{|_{A_{lg}}} \quad , \tag{1.24}$$

where $\phi_{|_{A_{lg}}}$ means the evaluation of ϕ on the liquid gas interface A_{lg} and $\hat{\mathbf{e}}_z$ is the unit normal on the substrate plane.

Via a gradient projection method, the triangulated interface $\mathbf{A}_{lg}$ iteratively is evolved towards a configuration of minimal interfacial free energy while obeying the volume constraint and any other given constraints on integrated quantities. The constraints are taken into account by Lagrange multipliers, which in a physical interpretation correspond to homogeneous force densities. Accordingly, the Lagrange multiplier of the volume constraint is given by the Laplace pressure Δp.

For an evaluation of the volume constraint on the interface $\mathbf{A}_{lg}$ the flux theorem yields

$$\int dV_l \;=\; \int_{A_s} d^2 R_{\|} \; h(\mathbf{R}_{\|}) \;=\; \int d\mathbf{A}_{lg} \cdot \mathbf{f} \quad , \tag{1.25}$$

where the kernel $\mathbf{f} = z\,\mathbf{e}_z$ follows from $\nabla \cdot \mathbf{f} \overset{!}{=} 1$.

An example for the graphical output of the algorithm is given in figure 1.3.

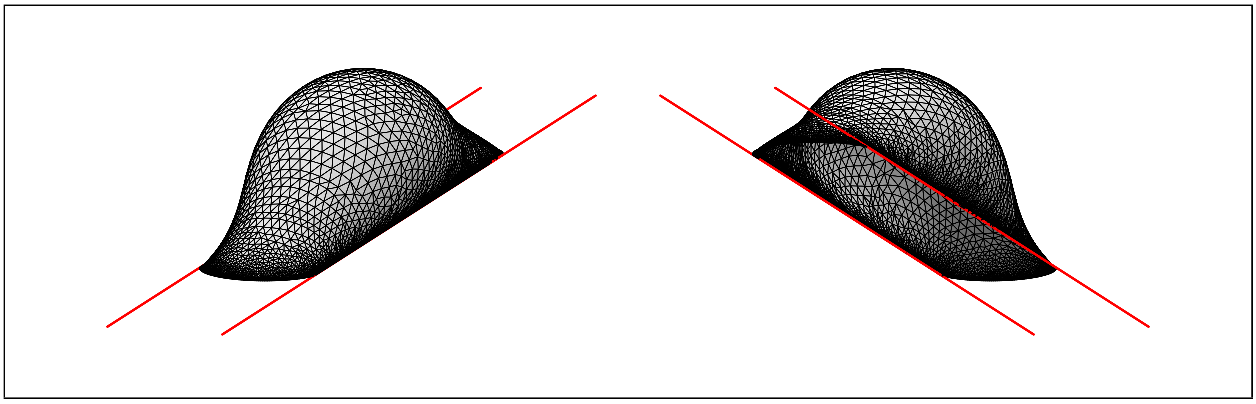

Figure 1.3: Top and bottom view of the triangulated liquid-gas interface A_{lg} of a sessile droplet on a chemical channel close to the minimum of the interfacial free energy $\tilde{F}$ given by (1.19). The chemical channel is given by a step-like variation of the local macroscopic contact angle θ. The channel edges are marked by the red lines. The mesh size of the triangulation was coupled to the interfacial height with respect to the substrate in order to have a high spatial resolution near the three-phase contact line.

Chapter 2

Fluid Dynamics from Kinetic Theory

From the macroscopic point of view, fluid dynamics in principle is governed by the Navier-Stokes equations, i.e., a set of coupled, non-linear, partial differential equations, which relate the diffusion and convection of mass, momentum and internal energy to the gradient of a stress tensor, to heat conduction, and to external fields [61, 69, 70]. The intrinsic fluid properties, which lead to a certain transport of momentum and energy independently from the transport of mass thereby are characterized by transport coefficients. The transport coefficients are given by the viscosity and the thermal conductivity, which appear within the stress tensor and the vector of heat conduction, respectively.

The Navier-Stokes equations provide a phenomenological approach to fluid dynamics in the sense that,

- ▷ the analytic expressions for the stress tensor and the vector of heat conduction, the so-called constitutive equations, have to be postulated,
- ▷ the transport coefficients are input parameters to be specified by experiment or a more fundamental theory,
- ▷ a thermodynamic equation of state for the hydrostatic pressure is needed in order to close the set of equations.

An alternative and more fundamental point of view on fluid dynamics is given by the framework of kinetic theory [57, 71–74]. Within kinetic theory, the complete physical information on the dynamics of the system is carried by the single-particle phase space distribution function, which is determined via an integro-differential equation, known as the Boltzmann equation. The physical properties on the fluid-dynamic level follow from the nature of the particle interactions incorporated in the Boltzmann equation. In the kinetic equilibrium the particle interactions become manifest in the wetting behaviour of different components or phases in the system, e.g., the formation of the macroscopic contact angle of a sessile fluid droplet.

Originally, these interactions are given by elastic two-body collisions, which corresponds to the limit of sufficiently dilute fluids. However, there exist modifications of the Boltzmann equation which describe the behaviour of non-ideal fluids, i.e., fluids which in the equilibrium case would be characterized by a non-ideal equation of state. The most prominent one is the Boltzmann-Enskog equation [57, 74, 75], which models effects on the kinetic level coming into play due to a finite fluid density. In the framework of the lattice Boltzmann equation, see chapter 3, additional two-body interactions are formally introduced based on both, mean field arguments and nearest neighbour interactions.

The fluid-dynamic limit of the Boltzmann equation is given by a set of dynamic equations for the so-called fluid-dynamic moments, formally equivalent to the phenomenological Navier-Stokes equations. The fluid-dynamic moments are local averages of physical quantities defined on the kinetic level, which directly correspond to physical quantities on the fluid-dynamic level, e.g, number density, momentum, stress, internal energy, and the fluxes of heat and energy. However, there are no explicite expressions for the hydrostatic pressure and the transport coefficients in terms of fluid-dynamic moments.

This problem can be approached by means of the Chapman-Enskog analysis [35, 57, 74–76], a multi-scaling analysis, which is based on the idea, that on the fluid-dynamic level ballistic and viscous effects in an incompressible, isothermal system appear on different time scales. These time scales are specified by the ratio of characteristic microscopic and macroscopic scales within the system. Applied to the Boltzmann equation, this analytic scheme yields kinetic equations with a fluid-dynamic limit in which the transport coefficients and the hydrostatic pressure explicitely appear as functions of specific physical quantities defined on the kinetic level.

The structure of the Boltzmann equation can be simplified drastically without any loss of the algebraic properties decisive for the physics encoded in the fluid-dynamic level equations. Hence, the calculation of the fluid-dynamic limit from a solution of the Boltzmann equation in many cases offers a great benefit compared to a direct integration of the Navier-Stokes equations, e.g, with respect to the implementation of boundary conditions. Simplifications of the Boltzmann equation, the so-called kinetic models, arise form a simplified treatment of interactions in the system. A well-known kinetic model is given by the so-called BGK-approximation of the Boltzmann equation [72, 77, 78]. The BGK-model is a very powerful approach, since, on the one hand, its linearized form allows for an algebraic treatment of the Boltzmann equation, and on the other hand, a very efficient iterative algorithm can be based on it. Numerical implementations of this algorithm rely on a fully discrete version of the Boltzmann equation, the lattice Boltzmann equation, see chapter 3.

In the following section, the basic features of the Boltzmann equation are briefly revised in order to provide the basis for a presentation of the fluid-dynamic limit in section 2.2, the BGK-approximation in section 2.3, and the Chapman-Enskog analysis in section 2.4.

2.1 The Boltzmann equation

The Boltzmann equation gives the convection of the single-particle phase space distribution function $f(\mathbf{r}, \boldsymbol{\zeta}, t)$ for a sufficiently dilute fluid composed of N particles in the volume V with an interaction range r_0 in the limit

$$N \;\rightarrow\; \infty \;, \quad Nr_0^3 \;\rightarrow\; 0 \;, \quad Nr_0^2 : \text{ finite} \quad , \tag{2.1a}$$

where the mean free path stays finite,

$$l_0 \;\sim\; \frac{V}{Nr_0^2} \quad , \tag{2.1b}$$

while the total interaction volume Nr_0^3 approaches zero. The particles do not have any internal degrees of freedom, i.e., they are fully characterized by their positional and velocity degrees of freedom, embraced by $\mathbf{r} = (r_1, r_2, r_3)$ and $\boldsymbol{\zeta} = (\zeta_1, \zeta_2, \zeta_3)$, respectively.

In case of a multi-component system, the Boltzmann equation for the particle type σ reads

$$\left[\partial_t + \boldsymbol{\zeta}_\sigma \cdot \nabla + \mathbf{a} \cdot \nabla_{\boldsymbol{\zeta}}\right] f_\sigma(\mathbf{r}, \boldsymbol{\zeta}_\sigma, t) \;=\; \sum_{\tilde{\sigma}} \mathcal{J}[f, f_*]_{\sigma\tilde{\sigma}} \quad . \tag{2.2}$$

The directional derivatives $\boldsymbol{\zeta}_\sigma \cdot \nabla$ and $\mathbf{a} \cdot \nabla_{\boldsymbol{\zeta}}$ on left hand side model the convection and the influence of an external field $\mathbf{a}$, respectively, where $\nabla_{\boldsymbol{\zeta}}$ is defined as the gradient in the velocity sub-space. The right hand side of the

Boltzmann equation (2.2) is given by a summation of the collision integrals,

$$\begin{aligned}\mathcal{J}[f, f_*]_{\sigma\tilde{\sigma}} &= \int d^3\zeta_{\tilde{\sigma}*} \int d\Omega \; |\Delta\boldsymbol{\zeta}|_{\sigma\tilde{\sigma}} \, \sigma_{\sigma\tilde{\sigma}} \, \{f'_\sigma f'_{\tilde{\sigma}*} - f_\sigma f_{\tilde{\sigma}*}\} && \text{(2.3a)} \\ &= \Gamma^{(+)}_{\sigma\tilde{\sigma}} - \Gamma^{(-)}_{\sigma\tilde{\sigma}} \quad , && \text{(2.3b)}\end{aligned}$$

where $d\Omega$ is the solid angle element in the positional sub-space, $\sigma_{\sigma\tilde{\sigma}}$ denotes the differential cross section of the collision process, $f_\sigma := f_\sigma(\mathbf{r}, \boldsymbol{\zeta}_\sigma, t)$ and $f'_{\tilde{\sigma}*} := f_{\tilde{\sigma}*}(\mathbf{r}, \boldsymbol{\zeta}'_{\tilde{\sigma}*}, t)$ denote pre- and post-collisional states, respectively, and $|\Delta\boldsymbol{\zeta}|_{\sigma\tilde{\sigma}} := |\boldsymbol{\zeta}_\sigma - \boldsymbol{\zeta}_{\tilde{\sigma}*}|$ is the absolute difference of the pre-collisional velocities. The collision integral (2.3) models the effective change of f_σ per unit time due to elastic two-body collisions. In case of collisions among particles of the same type, i.e., $\sigma = \tilde{\sigma}$, the distribution functions f and f_* refer to different particles of the same type.

The expressions $d^3\zeta_\sigma \, d^3r \, \Gamma^{(+)}_{\sigma\tilde{\sigma}} \, dt$ and $d^3\zeta_\sigma \, d^3r \, \Gamma^{(-)}_{\sigma\tilde{\sigma}} \, dt$ give the increase and the decrease of the particle number in the μ-space element $d^3\zeta_\sigma d^3r$ due to collisions during the time interval dt, respectively. Accordingly, the collision integral (2.3) is given by a difference of collision frequencies $\Gamma^{(+)}_{\sigma\tilde{\sigma}}$ and $\Gamma^{(-)}_{\sigma\tilde{\sigma}}$ corresponding to inverse scattering geometries.

Formally, the Boltzmann equation is derived from the Liouville theorem, which, for an N-particle system expresses the conservation of probability by stating that the distribution function $f^{(N)}(\vec{\mathcal{R}}, \vec{\mathcal{C}})$ in the N-particle phase space, $\Gamma := \mathrm{span}[\vec{\mathcal{R}}, \vec{\mathcal{C}}]$, behaves like an incompressible fluid. The vectors $\vec{\mathcal{R}} = (r_1, \ldots, r_{3N})$ and $\vec{\mathcal{C}} = (\zeta_1, \ldots, \zeta_{3N})$ embrace the $6N$ positional and velocity degrees of freedom of the system, respectively.

The Liouville theorem is given by[1]

$$0 = \left[\partial_t + \frac{\partial\mathcal{H}}{\partial p_\eta}\frac{\partial}{\partial r_\eta} - \frac{\partial\mathcal{H}}{\partial r_\eta}\frac{\partial}{\partial p_\eta}\right] f^{(N)}(\vec{\mathcal{R}},\vec{\mathcal{C}}) \tag{2.4a}$$

$$= \left[\partial_t + \boldsymbol{\zeta}_\kappa \cdot \nabla_\kappa - \left(\mathbf{a}_\kappa^{(\mathrm{int})} + \mathbf{a}_\kappa^{(ext)}\right) \cdot \nabla_{\zeta,\kappa}\right] f^{(N)}(\vec{\mathcal{R}},\vec{\mathcal{C}}) \quad . \tag{2.4b}$$

The formulation (2.4b) which explicitely refers to the $6N$ degrees of freedom labeled by $\eta = (1, \ldots, 3N)$ is given by the Poisson bracket of $f^{(N)}$ and the N-particle Hamiltonian $\mathcal{H}$. The formulation (2.4b) which refers to the particles labeled by $\kappa = (1, \ldots, N)$, is obtained from (2.4b) by means of the Hamilton equations for the canonic variables r_η and p_η,

$$\frac{\partial\mathcal{H}}{\partial p_\eta} = \dot{r_\eta} \quad , \qquad \frac{\partial\mathcal{H}}{\partial r_\eta} = -\dot{p_\eta} \quad .$$

In (2.4b) the time derivative of the momentum per unit mass has been split into a part $\mathbf{a}_\kappa^{(\mathrm{int})}$ due to the particle interactions and a part $\mathbf{a}_\kappa^{(\mathrm{ext})}$ due to an external field.

Integrating out $6(N-1)$ degrees of freedom and assuming a two-body interaction $\mathbf{a}_{\sigma\tilde{\sigma}}$ between particles of types σ and $\tilde{\sigma}$ yields

$$\left[\partial_t + \boldsymbol{\zeta} \cdot \nabla - \mathbf{a}^{(ext)} \cdot \nabla_\zeta\right] f_\sigma(\mathbf{r}, \boldsymbol{\zeta}, t) = \sum_{\tilde{\sigma}} \int d^3\zeta_{\tilde{\sigma}} \int d^3 r_{\tilde{\sigma}} \left(\mathbf{a}_{\sigma\tilde{\sigma}} \cdot \nabla_\zeta\right) f_{\sigma\tilde{\sigma}}^{(2)} \quad , \tag{2.5}$$

where $f_{\sigma\tilde{\sigma}}^{(2)} := f_{\sigma\tilde{\sigma}}^{(2)}(\mathbf{r}_\sigma, \mathbf{r}_{\tilde{\sigma}}, \boldsymbol{\zeta}_\sigma, \boldsymbol{\zeta}_{\tilde{\sigma}}, t)$ is the two-particle distribution function.

---

[1] Einstein 's Σ-convention is used here and in the following.

The integrated Liouville equation (2.5) can be reduced to the Boltzmann equation (2.2) under the following conditions [57, 72]:

- ▷ The particle interactions are short-ranged with a cut-off at r_0, i.e.,

$$r_0 \ll l_0 \quad , \qquad \mathbf{a}_{\sigma\tilde{\sigma}} \equiv 0 \quad \text{for} \quad |\mathbf{r}_\sigma - \mathbf{r}_{\tilde{\sigma}}| \geq r_0 \quad . \tag{2.6a}$$

- ▷ Molecular chaos is equivalent to the absence of correlations, i.e.,

$$f^{(2)}_{\sigma\tilde{\sigma}}(t) = f_\sigma(\mathbf{r}_\sigma, \boldsymbol{\zeta}_\sigma, t) f_{\tilde{\sigma}}(\mathbf{r}_{\tilde{\sigma}}, \boldsymbol{\zeta}_{\tilde{\sigma}}, t) \quad \text{for} \quad |\mathbf{r}_\sigma - \mathbf{r}_{\tilde{\sigma}}| \geq r_0 \quad . \tag{2.6b}$$

- ▷ Three-body collisions may be neglected, i.e.,

$$f^{(2)}_{\sigma\tilde{\sigma}}(\mathbf{r}'_\sigma, \mathbf{r}'_{\tilde{\sigma}}, \boldsymbol{\zeta}'_\sigma, \boldsymbol{\zeta}'_{\tilde{\sigma}}, t - \delta t) \;=\; f^{(2)}_{\sigma\tilde{\sigma}}(\mathbf{r}_\sigma, \mathbf{r}_{\tilde{\sigma}}, \boldsymbol{\zeta}_\sigma, \boldsymbol{\zeta}_{\tilde{\sigma}}, t) \quad . \tag{2.6c}$$

These conditions correspond to the the limit (2.1).

The collision integral

In a one component system the collision integral

$$\mathcal{J}[f, f_*] \;:=\; \int d^3\zeta_* \int d\Omega \; |\Delta\boldsymbol{\zeta}| \, \sigma \, \{f' f'_* - f f_*\} \tag{2.7}$$

models the modification of the distribution function f due to collisions. Of course, this has to be in accordance with the fundamental conservation laws, i.e., the conservation of particle number, momentum, and energy.

The basic property of $\mathcal{J}[f, f_*]$ which assures these conservation laws is given by the symmetry $\mathcal{J}[f, g] = \mathcal{J}[g, f]$. The consequence of this symmetry is that, by means of simple transformations [57, 72], the convolution of an arbitrary function $\psi(\boldsymbol{\zeta})$ and $\mathcal{J}[f, f_*]$ in the velocity sub-space can be written as

$$\int d^3\zeta \; \psi(\boldsymbol{\zeta})\mathcal{J}[f, f_*] \; = \\ \frac{1}{4}\int d^3\zeta \int d^3\zeta_* \int d\Omega \; |\Delta\boldsymbol{\zeta}| \, \sigma\big\{\psi(\boldsymbol{\zeta}) + \psi(\boldsymbol{\zeta}_*) - \psi(\boldsymbol{\zeta}') - \psi(\boldsymbol{\zeta}'_*)\big\} \, \{f' f'_* - f f_*\} \quad . \tag{2.8}$$

According to this relation the function $\psi(\boldsymbol{\zeta})$ represents a collision invariant, i.e., a quantity which is not changed by a collision, if

$$\psi(\boldsymbol{\zeta}) + \psi(\boldsymbol{\zeta}_*) \; = \; \psi(\boldsymbol{\zeta}') + \psi(\boldsymbol{\zeta}'_*) \quad , \tag{2.9a}$$

which is equivalent to

$$\int d^3\zeta \; \psi(\boldsymbol{\zeta})\mathcal{J}[f, f_*] \; \equiv \; 0 \quad , \tag{2.9b}$$

for a non-vanishing collision integral $\mathcal{J}[f, f_*]$.

The relations (2.8) and (2.9) in combination with the fundamental conservation laws give rise to the algebraic structure of a collision invariant $\psi(\boldsymbol{\zeta})$,

$$\psi(\boldsymbol{\zeta}) \; = \; \sum_{\eta=0}^{4} a^{(\eta)} \, \psi^{(\eta)}(\boldsymbol{\zeta}) \quad , \tag{2.10}$$

which is an expansion in terms of the set $\left\{\psi^{(\eta)}(\boldsymbol{\zeta})\right\}$ of so-called fundamental collision invariants. The set is given by the quantities

$$\begin{aligned}
\psi^{(0)} &= \mathbb{1} && \text{(2.11a)}\\
\psi^{(i)} &= \zeta_i \quad \text{for} \quad i = 1, 2, 3 && \text{(2.11b)}\\
\psi^{(4)} &= \frac{1}{2}\zeta_i\zeta_i \quad , && \text{(2.11c)}
\end{aligned}$$

which reflect the fundamental conservation laws for particle number, momentum, and energy, respectively.

In case of a multi-component system and in the absence of chemical reactions the number conservation for particles of type σ corresponds to the term by term vanishing summation

$$\sum_{\tilde{\sigma}} \int d^3\zeta \; \psi_\sigma^{(0)} \mathcal{J}[f, f_*]_{\sigma\tilde{\sigma}} \;\equiv\; 0 \quad , \tag{2.12}$$

where $\mathcal{J}[f, f_*]_{\sigma\tilde{\sigma}}$ is given by (2.3). By means of the expansions

$$\psi_\sigma(\boldsymbol{\zeta}) \;=\; \sum_{\eta=0}^{4} a_\sigma^{(\eta)} \, \psi_\sigma^{(\eta)}(\boldsymbol{\zeta}) \quad , \tag{2.13}$$

where the sets $\left\{\psi_\sigma^{(\eta)}(\boldsymbol{\zeta})\right\}$ correspond to the set (2.11) labeled by σ, the conservation of the total particle number, the total momentum, and the total energy is given by the overall summation

$$\sum_{\sigma} \sum_{\tilde{\sigma}} \int d^3\zeta \; \psi_\sigma(\boldsymbol{\zeta}) \mathcal{J}[f, f_*]_{\sigma\tilde{\sigma}} \;\equiv\; 0 \quad . \tag{2.14}$$

The equilibrium distribution

In the equilibrium case the physical behaviour on a macroscopic scale is not affected by the single-particle collisions taking place on the kinetic level. Hence, the equilibrium distribution function $f^{(\mathrm{eq})}$ is stationary,

$$f^{(\mathrm{eq})} f_*^{(\mathrm{eq})} = f^{(\mathrm{eq})'} f_*^{(\mathrm{eq})'} \quad , \tag{2.15a}$$

which means that the collision integral vanishes,

$$\mathcal{J}[f^{(eq)}, f_*^{(eq)}] \;\equiv\; 0 \quad . \tag{2.15b}$$

The form of $f^{(\mathrm{eq})}$, is a matter of the basic symmetry of the collision integral $\mathcal{J}[f, f_*]$. Insertion of $\psi \overset{!}{=} \ln[f]$ into the convolution (2.8) yields

$$\int d^3\zeta \; \ln[f]\mathcal{J}[f, f_*] \;=\; \frac{1}{4}\int d^3\zeta \int d^3\zeta_* \int d\Omega \, |\Delta\boldsymbol{\zeta}| \, \sigma \ln\left[\frac{f f_*}{f' f_*'}\right] \{f' f_*' - f f_*\} \quad , \tag{2.16}$$

which implies that the system is in equilibrium if $\ln[f]$ is a collision invariant. Accordingly, $\ln[f^{(\mathrm{eq})}]$ is given by an expansion in terms of the set of fundamental collision invariants (2.11),

$$\ln[f^{(eq)}] \;\overset{!}{=}\; a + \mathbf{b}\cdot\boldsymbol{\zeta} - \frac{\zeta_i\zeta_i}{c^2} \quad . \tag{2.17}$$

On the other hand, the local equilibrium situation is characterized by a stationary velocity field $\mathbf{u}(\mathbf{r})$ which gives the ordered motion of the system on the macroscopic level[2]. The equilibrium distribution function $f^{(eq)}$ therefore should depend on the random deviation of the molecular velocity $\boldsymbol{\zeta}$ from a constant macroscopic velocity $\mathbf{u}_0$.

---

[2] A definition of $\mathbf{u}(\mathbf{r}, t)$ in terms of fluid-dynamic moments of $f(\mathbf{r}, \boldsymbol{\zeta}, t)$ will be given in section 2.2

With this physical picture in mind the choice for coefficients a and $\mathbf{b}$ in (2.17) is

$$\mathbf{b} \overset{!}{=} 2\frac{\mathbf{u}_0}{c^2} \quad , \tag{2.18a}$$

$$a \overset{!}{=} \ln[A] - \left(\frac{\mathbf{u}_0}{c}\right)^2 \quad . \tag{2.18b}$$

This yields the basic form of the equilibrium distribution function, given by a Maxwellian centered around the constant velocity[3] $\mathbf{u}_0$,

$$f^{(eq)} = A(\mathbf{r},t)\, \exp\left[-\frac{U(\mathbf{r})}{c^2} - \frac{(\boldsymbol{\zeta}-\mathbf{u}_0)^2}{c^2}\right] \quad , \tag{2.19}$$

where $U(\mathbf{r})$ is a potential related to the external body force per unit mass $\mathbf{a}$, i.e.,

$$\mathbf{a} := -\nabla U(\mathbf{r}) = \frac{d}{dt}\boldsymbol{\zeta} \quad , \tag{2.20}$$

and the parameters A and c may depend on $\mathbf{r}$ and t but not on $\boldsymbol{\zeta}$. By means of phenomenologic thermodynamics these parameters can be related to the equilibrium density $\varrho_0 = N/V$ and the temperature T.

In the multi component case one has

$$\sum_{\sigma}\sum_{\tilde{\sigma}} \int d^3\zeta \;\ln[f_\sigma^{(eq)}]\, \mathcal{J}_{\sigma\tilde{\sigma}}[f_\sigma^{(eq)}, f_{\tilde{\sigma}*}^{(eq)}] = 0 \tag{2.21}$$

---

[3] Of course, $\mathbf{u}_0$ is not significant here, since it can be removed by means of a Galileo transformation. The local Maxwellian, in which $\mathbf{u}_0$ is replaced by $\mathbf{u}(\mathbf{r})$, plays a role in the framework of the BGK-approximation, see section 2.3.

and

$$f_\sigma^{(eq)} = A_\sigma \exp\left[-\frac{\phi(\mathbf{r})}{c_\sigma^2} - \frac{(\boldsymbol{\zeta}_\sigma - \mathbf{u}_{0,\sigma})^2}{c_\sigma^2}\right] \quad . \tag{2.22}$$

The $\mathcal{H}$-theorem

The $\mathcal{H}$-theorem is a fundamental statement, which relates the level of disorder within a closed system to the irreversibility of relaxation processes.

The local level of disorder is expressed by means of the entropy density,

$$\mathcal{H}(\mathbf{r},t) \ := \ -\int d^3\zeta \ \ln[f]\, f \quad , \tag{2.23a}$$

and its corresponding flux,

$$\mathbf{H}(\mathbf{r},t) \ := \ -\int d^3\zeta \ \boldsymbol{\zeta} \ln[f]\, f \quad . \tag{2.23b}$$

The theorem is based on a fundamental property of the collision integral,

$$0 \ \geq \ \int d^3\zeta \ \ln[f]\, \mathcal{J}[f, f_*] \quad , \tag{2.24}$$

which directly follows from the convolution (2.16).

Multiplying the Boltzmann equation (2.2) by $\{\mathbb{1} + \ln[f]\}$, integrating out the velocity degrees of freedom, and taking into account the inequality (2.24) as well as the fact that $\mathbb{1}$ is a collision invariant, one finds the relation [72]

$$\partial_t \mathcal{H} + \nabla \cdot \mathbf{H} \ = \ \int d^3\zeta \ \mathcal{J}[f, f_*] \ln[f] \ \geq \ 0 \quad . \tag{2.25}$$

The overall entropy in the volume V,

$$\bar{\mathcal{H}}(t) := \int_V d^3r \, \mathcal{H} \quad , \tag{2.26}$$

then in case of a non-moving boundary $\partial(V)$ of V obeys

$$\frac{d\bar{\mathcal{H}}}{dt} - \int_{\partial(V)} dA \, \mathbf{n} \cdot \mathbf{H} \;\geq\; 0 \quad , \tag{2.27}$$

where the vector $\mathbf{n}$ is the inward unit normal on the surface element dA of $\partial(V)$.

Hence, the surface integral in (2.27) gives the influx of entropy into V and it can be shown that this influx of entropy is equivalent to an influx of energy [72], i.e.,

$$\int_{\partial(V)} dA \, \mathbf{n} \cdot \mathbf{H} \;=\; \int_{\partial(V)} dA \, \frac{1}{RT} \left(q_i + p_{ij} v_j\right) \quad . \tag{2.28}$$

All together, one has the $\mathcal{H}$-THEOREM formed by the equations

$$\frac{d\bar{\mathcal{H}}}{dt} \;\geq\; \int_{\partial(V)} dA \, \frac{1}{RT} \left(q_i + p_{ij} v_j\right) \tag{2.29a}$$

and

$$\partial_t \mathcal{H} + \nabla \cdot \mathbf{H} \;=\; \int d^3\zeta \;\ln[f] \, \mathcal{J}[f, f_*] \;\geq\; 0 \quad . \tag{2.29b}$$

The $\mathcal{H}$-theorem states, that according to (2.29a), the entropy of a closed system is not decreasing in time, and that, according to (2.29b), the entropy is constant in time only in equilibrium systems. Concisely, a closed system irreversibly relaxes towards an equilibrium state characterized by a maximum level of disorder. The $\mathcal{H}$-theorem is the fundamental kinetic statement underlying the second law of thermodynamics as formulated by Clausius, Kelvin, and Planck.

2.2 The fluid-dynamic limit of the Boltzmann equation

The framework of the Boltzmann equation (2.2) presented in the preceeding section provides a statistical point of view on the kinetics of the particles in a dilute fluid via the distribution function $f(\mathbf{r}, \boldsymbol{\zeta}, t)$ of the independent, microscopic positions $\mathbf{r}$ and velocities $\boldsymbol{\zeta}$.

From a macroscopic point of view however, a fluid may be characterized by an ordered motion, i.e., a whole fluid element with a certain particle density $\varrho(\mathbf{r}, \boldsymbol{\zeta})$ travels within a macroscopic velocity field $\mathbf{u}(\mathbf{r}, t)$ and the kinetic energy per unit mass associated with this ordered motion of a fluid element is

$$E_{\text{kin}} := \frac{1}{2} u_i u_i \quad . \tag{2.30}$$

Within such a fluid element the particles perform a random motion characterized by the microscopic velocities $\boldsymbol{\zeta}$. Hence, the internal energy per unit mass, i.e., the contribution of a single particle whirring around at $\boldsymbol{\zeta}$ to the internal energy, is given by the expression

$$\mathcal{E} := \frac{1}{2} |\zeta_i - u_i|^2 := \frac{1}{2} c_i c_i \quad . \tag{2.31}$$

The vector $\mathbf{c}$ is the so-called random velocity deviation. To obtain the internal energy E of a whole fluid element centered around $\mathbf{r}$ the distribution of the microscopic velocities encoded in the distribution function $f(\mathbf{r}, \boldsymbol{\zeta}, t)$ has to be taken into account.

The fluid-dynamic level of the Boltzmann equation is given by a set of dynamic equations for the quantities ϱ, $\mathbf{u}$, E_{kin}, and E. This set of equations, the Navier-Stokes equations, is obtained by means of a local averaging procedure applied to the Boltzmann equation.

The fluid-dynamic moments

The quantities which bridge the gap between the kinetic theory governed by the Boltzmann equation (2.2) and fluid dynamics governed by the Navier-Stokes equations are given by velocity moments of adequate physical quantities, the so-called fluid-dynamic moments. Generally, such a velocity moment is a local average of a function $q(\mathbf{r}, \boldsymbol{\zeta}, t)$, defined as a convolution in the velocity sub-space of the phase space $\mu := \text{span}[\mathbf{r}, \boldsymbol{\zeta}]$.

The definitions of the zeroth, first, and second fluid-dynamic moment of an arbitrary microscopic quantity $q(\mathbf{r}, \boldsymbol{\zeta}, t)$ read

$$\mathcal{M}^{(0)}[q] \quad := \quad \int_\mu d^D\zeta \; qf \quad , \tag{2.32a}$$

$$\mathcal{M}_i^{(1)}[q] \quad := \quad \int_\mu d^D\zeta \; \zeta_i q f \quad , \tag{2.32b}$$

$$\mathcal{M}_{ij}^{(2)}[q] \quad := \quad \int_\mu d^D\zeta \; \zeta_i \zeta_j \, qf \quad , \tag{2.32c}$$

whereas the integration range covers the whole velocity sub-space of μ.

The fluid-dynamic moments are local objects given at a certain position $\mathbf{r}$

and time t. The mean value of the quantity $q(\mathbf{r},\boldsymbol{\zeta},t)$ therefore reads

$$\langle\, q\,\rangle \;:=\; \int_\mu d^D r \mathcal{M}^{(0)}[q] \;=\; \int_\mu d^D r \int_\mu d^D\zeta\; qf \quad , \tag{2.33}$$

and the normalization of the distribution function f to the particle number N,

$$N \;\overset{!}{=}\; \langle\, \mathbb{1}\,\rangle \;=\; \int d^D r \int d^D\zeta\; f \quad , \tag{2.34}$$

yields the number density

$$\varrho(\mathbf{r}) \;=\; \int d^D\zeta\; f \;=\; \mathcal{M}^{(0)}[\mathbb{1}] \quad . \tag{2.35}$$

The physical meaning of the zeroth and first moment, $\mathcal{M}^{(0)}[q]$ and $\mathcal{M}^{(1)}_i[q]$, is the local density and the flux of q, respectively. Since in the definitions (2.32) the higher moments are not unique, their corresponding mean values may be interpreted by means of the relation

$$\mathcal{M}^{(2)}_{ij}[q] \;=\; \mathcal{M}^{(1)}_i[\zeta_j q] \;=\; \mathcal{M}^{(0)}[\zeta_i\zeta_j q] \quad .$$

The fluid-dynamic moments decisive for the derivation of the fluid-dynamic level equations are those of the fundamental collision invariants $\psi^{(\eta)}$ (2.11), i.e.,

$$\begin{aligned} \mathcal{M}^{(0)}[\psi^{(0)}] &= \varrho(\mathbf{r}) \quad , && (2.36a) \\ \mathcal{M}^{(0)}[\psi^{(i)}] &= \varrho(\mathbf{r})u_i(\mathbf{r}) \quad , && (2.36b) \\ \mathcal{M}_i^{(1)}[\psi^{(j)}] &= p_{ij} + \varrho u_i u_j \quad , && (2.36c) \\ \mathcal{M}^{(0)}[\psi^{(4)}] &= \varrho E + \frac{1}{2}\varrho\, u_j u_j \quad , && (2.36d) \\ \mathcal{M}_i^{(1)}[\psi^{(4)}] &= Q_i + u_j\, p_{ij} + \frac{1}{2} u_i\, p_{jj} + \frac{1}{2}\varrho\, u_i u_j u_j \quad . && (2.36e) \end{aligned}$$

The quantities ϱu_i in (2.36) are the components of the momentum density or, according to (2.2), the components of the particle flux. The quantities

$$p_{ij} := \mathcal{M}^{(0)}[c_i c_j] \tag{2.37}$$

in (2.36c) and (2.36e) are the components of the stress tensor, also called the pressure tensor, where the components c_i of the random velocity deviation are given by (2.31). The internal energy density ϱE and the components of the heat flux $\mathbf{Q}$ in (2.36d) and (2.36e) are defined as

$$\varrho E := \mathcal{M}^{(0)}[\mathcal{E}] \quad , \tag{2.38a}$$

and

$$Q_i := \mathcal{M}_i^{(1)}[\mathcal{E}] \quad , \tag{2.38b}$$

where the internal energy per unit mass $\mathcal{E}$ is given by (2.31). The expressions (2.36d) and (2.36e) thus are the total energy density and the total energy flux, respectively.

For the kernel $\mathbf{a} \cdot \nabla_\zeta = a_k \partial_{\zeta_k}$, partial integration yields

$$\begin{aligned} \mathcal{M}^{(0)}[a_k \partial_{\zeta_k}] &= 0 \quad , && (2.39a) \\ \mathcal{M}_i^{(1)}[a_k \partial_{\zeta_k}] &= -\varrho a_i \quad , && (2.39b) \\ \mathcal{M}_{ij}^{(2)}[a_k \partial_{\zeta_k}] &= -\varrho \left(a_i u_j + a_j u_i \right) \quad . && (2.39c) \end{aligned}$$

The expressions (2.39b) and (2.39c) are components of the local density and the corresponding flux associated with the external field $\mathbf{a}$.

The fluid-dynamic level equations

By means of the definitions (2.32) of fluid-dynamic moments, the Boltzmann equation for a one-component system,

$$[\partial_t + \boldsymbol{\zeta} \cdot \nabla + \mathbf{a} \cdot \nabla_{\boldsymbol{\zeta}}] f(\mathbf{r}, \boldsymbol{\zeta}, t) = \mathcal{J}[f, f_*] \quad , \tag{2.40}$$

can be transformed into an equation of zeroth moments of a microscopic quantity $q(\mathbf{r}, \boldsymbol{\zeta}, t)$,

$$\mathcal{M}^{(0)}[\partial_t q] + \mathcal{M}^{(0)}[\zeta_i \partial_i q] + \mathcal{M}^{(0)}[a_k \partial_{\zeta_k} q] = \int_\mu d^3\zeta \; q \mathcal{J}[f, f_*] \quad . \tag{2.41}$$

The kernels on the left hand side of this equation reflect the analytic structure of the underlying Boltzmann equation. Taking into account, firstly, the properties (2.11) of the collision integral with respect to the fundamental collision invariants $\psi^{(\eta)}$, and secondly, that $\mathbf{r}$ and $\boldsymbol{\zeta}$ are independent variables, the assignments $q \overset{!}{=} \mathbb{1}$, $q \overset{!}{=} c_i$, and $q \overset{!}{=} \frac{1}{2} c_i c_i$ in (2.41) yield

$$\partial_t \varrho + \partial_i \varrho u_i \quad = \quad 0 \quad , \tag{2.42a}$$

$$[\partial_t + u_j \partial_j] \; \varrho u_i \quad = \quad -\partial_j \, p_{ij} + \varrho a_i \quad , \tag{2.42b}$$

$$[\partial_t + u_j \partial_j] \, \varrho E \quad = \quad -\partial_j (p_{ij} u_i + Q_j) + \varrho a_i u_i \quad , \tag{2.42c}$$

respectively. This set of equations expresses the fundamental conservation laws. The continuity equation (2.42a) corresponds to number conservation. The equations (2.42b) and (2.42c) corresponds to the balance of momentum and the conservation of internal energy, respectively. The set (2.42) is formally equivalent to the phenomenological Navier-Stokes equations [61, 69, 70].

According to (2.31), (2.37), and (2.38b), the quantities p_{ij} and Q_i within (2.42) are given in terms of the random velocity $\mathbf{c}$,

$$p_{ij} \quad = \quad \mathcal{M}^{(0)}[c_i c_j] \quad , \tag{2.43a}$$

$$Q_i \quad = \quad \mathcal{M}^{(1)}_i[\mathcal{E}] \; = \; \frac{1}{2} \mathcal{M}^{(1)}_i[c_j c_j] \quad , \tag{2.43b}$$

which reflects the microscopic point of view of the underlying kinetic theory. From the point of view of the phenomenological Navier-Stokes equations, however, constitutive equations have to be postulated, which relate these quantities to the macroscopic variables ϱ, $\mathbf{u}$, and the temperature T:

▷ In a non-viscous and thermally non-conducting fluid, a so-called Euler fluid, the transport of momentum and energy mainly happens due to the transport of mass. The constitutive equations thus read

$$
\begin{aligned}
p_{ij} &\overset{!}{=} p(\varrho, T)\delta_{ij} \quad , && (2.44a)\\
Q_i &\overset{!}{=} 0 \quad . && (2.44b)
\end{aligned}
$$

▷ In a viscous and thermally conducting fluid, a so-called Navier-Stokes-Fourier fluid, the transport of momentum and energy happens due to a combination of mass transport, internal friction, and thermal conduction. Assuming linear response, the constitutive equations in this case read

$$
\begin{aligned}
p_{ij} &\overset{!}{=} p(\varrho, T)\delta_{ij} - \mu\left[\partial_j u_i + \partial_i u_j\right] - \nu \partial_k u_k \delta_{ij} \quad , && (2.45a)\\
Q_i &\overset{!}{=} -\kappa \partial_i T \quad . && (2.45b)
\end{aligned}
$$

In the framework of thermodynamics, the pressure $p(\varrho, T)$ is given via an equation of state, whereas the dynamic viscosity μ, the second viscosity ν, and the thermal conductivity κ are material parameters, which are supposed to picture intrinsic fluid properties as functions of ϱ and T. The kinetic theory by itself, however, does not provide any expressions, which in the fluid-dynamic limit directly correspond to $p(\varrho, T)$ and the material parameters μ, ν, and κ.

Via the Chapman-Enskog analysis of the Boltzmann equation with the BGK-operator, see sections 2.3 and 2.4, both, the thermodynamic equation of state is recovered, and the material parameters are related to microscopic parameters defined on the kinetic level.

Thermodynamic relations

The internal energy per unit mass E in (2.42c) is a quantity specified in terms of the microscopic variable c_i. From the point of view of thermodynamics, E is given as a function of the temperature T. Further, there are equations of state, which relate the internal energy E, the hydrostatic pressure p_0, and the temperature T to each other.

In a general equilibrium case, (2.31), (2.37), and (2.45) suggest that in a D-dimensional system the hydrostatic pressure p_0 may be identified by the trace of the isotropic part of the stress tensor, i.e.,

$$p_0 \overset{!}{=} \frac{1}{D}\,\mathrm{tr}[p\delta_{ij}] = p(\varrho, T) \quad . \tag{2.46}$$

Thus, the general form of the equation of state reads

$$p_0 = \frac{2}{D}\varrho E \quad . \tag{2.47}$$

On the other hand, the conditions (2.1) for the derivation of the Boltzmann equation from the Liouville theorem correspond to an ideal gas with the thermodynamic equation of state

$$p_0 = \varrho\frac{k_B T}{m} \quad . \tag{2.48}$$

Accordingly, the internal energy E obeys

$$E = \frac{D}{2}\frac{k_B T}{m} \quad . \tag{2.49}$$

By means of (2.48) the width c of the equilibrium distribution function $f^{(\mathrm{eq})}$ (2.19) can be specified, i.e.,

$$f^{(eq)} \;=\; \frac{1}{z}\varrho_0(2\pi c_T^2)^{-D/2}\exp\left[-\frac{\mathcal{E}+U(\mathbf{r})}{c_T^2}\right] \quad , \tag{2.50}$$

with the thermal velocity,

$$c_T^2 \;:=\; (\partial_\varrho p_0)_{|\mathrm{adiabat}} \;=\; \frac{k_B T}{m} \quad , \tag{2.51}$$

as the scaling parameter for the internal energy[4] per unit mass $\mathcal{E}$, the equilibrium density distribution ϱ, and the potential $U(\mathbf{r})$ related to the external body force per unit mass $\mathbf{a}$, i.e.,

$$\mathbf{a} \;:=\; -\nabla U(\mathbf{r}) \;=\; \frac{d}{dt}\boldsymbol{\zeta} \quad . \tag{2.52}$$

Finally, the normalization (2.34) yields

$$z \;=\; \frac{1}{V}\int d^D r\,\exp\left[-\frac{U(\mathbf{r})}{c_T^2}\right] \quad . \tag{2.53}$$

According to equation (2.51) the width of the equilibrium distribution function $f^{(eq)}$ (2.50) in equilibrium, as in any isothermal system, is equal at any point in space. In case of an inhomogeneous system, the equilibrium density distribution ϱ_0 minimizes the Helmholtz free energy density

$$\Psi(\varrho) \;=\varrho E\int d\varrho\,\frac{1}{\varrho} \;=\; \varrho E\ln\varrho \quad , \tag{2.54}$$

---

[4] In statistical mechanics the temperature T is defined via the change of entropy S with respect to the internal energy E in a closed system, i.e., $\frac{1}{T} := \left(\frac{\partial S}{\partial E}\right)_{|V,N}$.

which itself follows from a Legendre transformation of the hydrostatic pressure p_0,

$$p_0 \ = \ \varrho \frac{d\Psi}{d\varrho} - \Psi \quad , \tag{2.55}$$

and the equation of state (2.47).

2.3 The BGK-model

The collision integral $\mathcal{J}[f, f_*]$ (2.7) forming the right hand side of the Boltzmann equation of a one-component system contains detailed information on the kinetic level and its structure thus is very complicated to deal with. On the other hand, the whole fine structure of the collision integral is averaged out at the fluid-dynamic level and therefore the details of the interactions expressed in $\mathcal{J}[f, f_*]$ are not likely to influence the fluid dynamics qualitatively.

With this situation in mind, the idea behind the so-called BGK-model [72, 77], named by its developers P.L. Bhatnagar, E.P. Gross, and M. Krook[5], is, to replace the collision integral $\mathcal{J}[f, f_*]$ by a model operator, which spares insignificant details and retains the essential average properties of $\mathcal{J}[f, f_*]$ only, in order to obtain a model equation which has an algebraic structure suitable for an iterative treatment.

According to the expressions (2.9) and (2.16) discussed in section 2.1, the essential average properties of $J[f, f_*]$ are the following:

- ▷ The convolution of $J[f, f_*]$ with a collision invariant ψ in the velocity sub-space vanishes, i.e.,

$$\int d^3\zeta \ \psi(\boldsymbol{\zeta})\mathcal{J}[f, f_*] \ \equiv \ 0 \quad . \tag{2.56}$$

According to the expansion (2.10), ψ thereby is given in terms of the set $\left\{\psi^{(\eta)}\right\}$ of fundamental collision invariants. The property (2.56) ensures the validity of the fundamental conservation laws of particle number, momentum, and energy.

---

[5] P. Welander [78] independently proposed the model at about the same time.

▷ The collision integral generally obeys

$$\int d^3\zeta \; \mathcal{J}[f, f_*] \ln[f] \;\leq\; 0 \quad , \tag{2.57}$$

whereupon the equality sign holds in the equilibrium case. Based on the relation (2.57) the $\mathcal{H}$-theorem shows that the collision integral models an irreversible relaxation of the system towards the equilibrium state determined by the Maxwellian $f^{(\mathrm{eq})}$ (2.19).

In a straightforward way, the BGK-operator maps the average effect of the interactions encoded in the collision integral $\mathcal{J}[f, f_*]$ by a change of the distribution function $f(\mathbf{r}, \boldsymbol{\zeta}, t)$ proportional to its deviation from a local Maxwellian

$$\phi \;:=\; A(\mathbf{r}, t)\, \exp\left[-\frac{U(\mathbf{r})}{c_T^2} - \frac{\big(\boldsymbol{\zeta} - \mathbf{u}(\mathbf{r}, t)\big)^2}{c_T^2}\right] \quad , \tag{2.58}$$

with the density $\varrho(\mathbf{r}, t)$, the average velocity $\mathbf{u}(\mathbf{r}, t)$, and the potential $U(\mathbf{r})$ related to the external body force per unit mass $\mathbf{a}$ via

$$\mathbf{a} \;:=\; -\nabla U(\mathbf{r}) \;=\; \frac{d}{dt}\boldsymbol{\zeta} \quad . \tag{2.59}$$

The BGK-operator is defined as

$$\mathcal{J}_{\mathrm{BGK}}[f] \;:=\; -\frac{1}{\lambda}\left[f(\mathbf{r}, \boldsymbol{\zeta}, t) - \phi_{|(\mathbf{r}, \boldsymbol{\zeta}, t)}\right] \quad , \tag{2.60}$$

and thus, the Boltzmann equation is replaced by the BGK-model equation

$$[\partial_t + \boldsymbol{\zeta} \cdot \nabla + \mathbf{a} \cdot \nabla_{\boldsymbol{\zeta}}]\, f(\mathbf{r}, \boldsymbol{\zeta}, t) \;=\; -\frac{1}{\lambda}\left[f(\mathbf{r}, \boldsymbol{\zeta}, t) - \phi_{|(\mathbf{r},\boldsymbol{\zeta},t)}\right] \quad , \qquad (2.61)$$

whereupon the parameter λ plays the role of a relaxation time.

According to (2.56), the fundamental conservation laws require

$$\int d^3\zeta \;\psi(\boldsymbol{\zeta})\mathcal{J}_{\mathrm{BGK}}[f] \;\overset{!}{=}\; 0 \quad , \qquad (2.62a)$$

which implies

$$\mathcal{M}^{(0)}[\psi^{(\eta)}] \;:=\; \int d^2\zeta \;\psi^{(\eta)} f(\mathbf{r}, \boldsymbol{\zeta}, t) \;\overset{!}{=}\; \int d^2\zeta \;\psi^{(\eta)} \phi(\varrho, \mathbf{u}, c_T) \quad . \qquad (2.62b)$$

This means that the local Maxwellian ϕ (2.58) is constrained by $f(\mathbf{r}, t)$ at any position $\mathbf{r}$ and time instant t, i.e., the quantities $\varrho(\mathbf{r}, t)$, $\mathbf{u}(\mathbf{r}, t)$, and c_T are calculated from the distribution function $f(\mathbf{r}, \boldsymbol{\zeta}, t)$ via the relations (2.36a), (2.36b), (2.38a), and (2.49).

Following (2.57), the requirement for irreversibility is

$$\int d^3\zeta \;\ln[f]\mathcal{J}_{\mathrm{BGK}} \;\overset{!}{\leq}\; 0 \quad . \qquad (2.63)$$

This requirement is automatically fulfilled since ϕ is a Maxwellian, i.e.,

$$\int d^3\zeta \;\mathcal{J}_{\mathrm{BGK}} \ln[\phi] \;\equiv\; 0 \quad , \qquad (2.64)$$

and hence,

$$\begin{aligned}\int d^3\zeta\ \ln[f]\mathcal{J}_{\rm BGK} &= \int d^3\zeta\ \mathcal{J}_{\rm BGK}\ln\left[\frac{f}{\phi}\right] + \int d^3\zeta\ \mathcal{J}_{\rm BGK}\ln[\phi] = \\ &= \frac{1}{\lambda}\int d^3\zeta\ \phi\left(1-\frac{f}{\phi}\right)\ln\left[\frac{f}{\phi}\right] \le 0 \quad . \end{aligned} \tag{2.65}$$

Integral solution

An integration of (2.61) over a time interval Δt along an approximated phase space trajectory yields a formal integral solution of the BGK-model equation [73],

$$\begin{aligned} f(\mathbf{r}+\boldsymbol{\zeta}\Delta t+\frac{1}{2}\mathbf{a}\Delta t^2, \boldsymbol{\zeta}+\mathbf{a}\Delta t, t+\Delta t) &= e^{-\frac{g_{r_0}}{\lambda}\Delta t}\ \big[\, f(\mathbf{r},\boldsymbol{\zeta},t) \\ &\quad + \frac{g_{r_0}}{\lambda}\int_0^{\Delta t} dt'\, e^{-\frac{g_{r_0}}{\lambda}t'}\ \phi_{|(t+t')} \\ &\quad + \mathbf{a}\cdot\int_0^{\Delta t} dt'\, e^{-\frac{g_{r_0}}{\lambda}t'}\ \nabla_\zeta f(t+t')\ \big] \quad , \end{aligned} \tag{2.66}$$

where $\mathbf{r}' = \mathbf{r}+\boldsymbol{\zeta}t'+\frac{1}{2}\mathbf{a}t'^2$ and $\boldsymbol{\zeta}' = \boldsymbol{\zeta}+\mathbf{a}t'$.

An application of the mean-value theorem, and a Taylor expansion in time up to the linear order yields a time-discrete version of (2.66),

$$f(\mathbf{r}+\boldsymbol{\zeta}\Delta t, \boldsymbol{\zeta}, t+\Delta t) - f(\mathbf{r},\boldsymbol{\zeta},t) = -\frac{1}{\tau}\left[f(\mathbf{r},\boldsymbol{\zeta},t) - \phi_{|(\mathbf{r},\boldsymbol{\zeta},t)}\right] - \mathbf{a}\cdot\nabla_\zeta f(\mathbf{r},\boldsymbol{\zeta},t)\Delta t \quad , \tag{2.67}$$

where $\tau := \lambda/\Delta t$ is the dimensionless relaxation time.

In the limit of small Mach numbers, $|\mathbf{u}|/c_T \ll 1$, both the local Maxwellian ϕ (2.58) and the forcing-term $\mathbf{a}\cdot\nabla_\zeta f(\mathbf{r},\boldsymbol{\zeta},t)$ can be expanded up to the order $\mathbf{u}^2$. For the local Maxwellian ϕ one finds

$$\phi(\boldsymbol{\zeta},\mathbf{u}) \;\approx\; \varrho(\mathbf{r})\,\omega(\boldsymbol{\zeta})\left\{1+\frac{1}{c_T^2}(\boldsymbol{\zeta}\cdot\mathbf{u})+\frac{1}{2c_T^4}(\boldsymbol{\zeta}\cdot\mathbf{u})^2-\frac{1}{2c_T^2}\mathbf{u}^2\right\} \quad , \tag{2.68}$$

with

$$\omega(\boldsymbol{\zeta}) \;=\; \frac{(2\pi c_T^2)^{-D/2}}{z}\exp\left[-\frac{1}{c_T^2}\left(\frac{1}{2}\boldsymbol{\zeta}^2+U\right)\right] \tag{2.69}$$

and the normalization factor

$$z \;=\; \frac{1}{V}\int d^D r\,\exp\left[-\frac{U(\mathbf{r})}{c_T^2}\right] \quad . \tag{2.70}$$

Via the relations (2.39) and the constraint (2.62), an expansion of the forcing term $\mathbf{a}\cdot\nabla_\zeta f$ up to the order $\boldsymbol{\zeta}^2$,

$$\mathbf{a}\cdot\nabla_\zeta f \;\approx\; \varrho(\mathbf{r})\omega(\boldsymbol{\zeta})\left[c^{(0)}+c_i^{(1)}\zeta_i+c_{ij}^{(2)}\zeta_i\zeta_j\right] \quad , \tag{2.71}$$

yields the low Mach number expression [56]

$$\mathbf{a}\cdot\nabla_\zeta f \;\approx\; F \;:=\; -\omega(\boldsymbol{\zeta})\,\varrho(\mathbf{r})\left[\frac{1}{c_T^2}(\boldsymbol{\zeta}-\mathbf{u})+\frac{1}{c_T^4}(\boldsymbol{\zeta}\cdot\mathbf{u})\boldsymbol{\zeta}\right]\cdot\mathbf{a} \quad . \tag{2.72}$$

Both, the local Maxwellian ϕ (2.58) and the forcing term F on the right hand side of (2.67) are constrained by $f(\mathbf{r},\boldsymbol{\zeta},t)$ for any $\mathbf{r}$ and t via (2.36a), (2.36b), (2.38a), (2.49), and (2.51). This means that the time-discrete BGK-model equation (2.67) in the small Mach number limit can be solved iteratively, since the change of the distribution function $f(\mathbf{r}, \boldsymbol{\zeta}, t)$ due to convection during the time step Δt is fully determined by $f(\mathbf{r}, \boldsymbol{\zeta}, t)$ itself.

2.4 The Chapman-Enskog analysis

In section 2.2, the fluid-dynamic level equations (2.42) of the Boltzmann equation (2.40) have been presented. Further, the stress tensor p_{ij} and the heat conduction Q_i therein, which are given by fluid-dynamic moments of the random velocity deviation c_i (2.31),

$$
\begin{aligned}
p_{ij} &= \mathcal{M}^{(0)}[c_i c_j] \quad , && (2.73\text{a}) \\
Q_i &= \mathcal{M}_i^{(1)}[\mathcal{E}] = \frac{1}{2}\mathcal{M}_i^{(1)}[c_j c_j] \quad , && (2.73\text{b})
\end{aligned}
$$

have been opposed to the phenomenological, constitutive equations of a viscous, thermally conducting fluid,

$$
\begin{aligned}
p_{ij} &= p\delta_{ij} - \mu\left[\partial_j u_i + \partial_i u_j\right] - \nu \partial_k u_k \delta_{ij} \quad , && (2.74\text{a}) \\
Q_i &= -\kappa \partial_i T \quad . && (2.74\text{b})
\end{aligned}
$$

This has been done in order to reveal the conceptual gap between the macroscopic and the kinetic approach to fluid dynamics, which is given by a missing link between microscopic quantities defined on the kinetic level and the transport coefficients μ, ν, and κ within the constitutive equations (2.74).

In case of an incompressible and isothermal fluid, i.e.,

$$
\begin{aligned}
p_{ij} &= p\delta_{ij} - \mu\left[\partial_j u_i + \partial_i u_j\right] \quad , && (2.75\text{a}) \\
Q_i &= 0 \quad , && (2.75\text{b})
\end{aligned}
$$

this conceptual gap can be bridged by the Chapman-Enskog analysis of the BGK-model equation (2.61). The Chapman-Enskog analysis is based on the idea that the characteristic fluid dynamic properties encoded in (2.75b) emerge on two well-separated time scales: A microscopic time scale is associated with the ballistic regime, in which the transport of momentum due to advection leads to the pressure p, whereas a macroscopic time scale is associated with the viscous regime, in which the transport of momentum due to internal friction is modeled by the viscosity μ.

The starting point of the Chapman-Enskog analysis is the time-discrete BGK-model equation (2.67),

$$f(\mathbf{r}+\boldsymbol{\zeta}\Delta t,\boldsymbol{\zeta},t+\Delta t)-f(\mathbf{r},\boldsymbol{\zeta},t) \;=\; -\frac{1}{\tau}\left[f(\mathbf{r},\boldsymbol{\zeta},t)-\phi_{|(\mathbf{r},\boldsymbol{\zeta},t)}\right]-F\Delta t \quad , \tag{2.76}$$

with the finite time interval Δt, the dimensionless relaxation time $\tau := \lambda/\Delta t$, and the low Mach number expression (2.72) for the forcing term $\mathbf{a}\cdot\nabla_{\zeta} f(\mathbf{r},\boldsymbol{\zeta},t)$,

$$F \;=\; \varrho(\mathbf{r})\,\omega(\boldsymbol{\zeta})\;\mathbf{a}\cdot\left[\frac{1}{c_T^2}(\boldsymbol{\zeta}-\mathbf{u})+\frac{1}{c_T^4}(\boldsymbol{\zeta}\cdot\mathbf{u})\boldsymbol{\zeta}\right] \quad . \tag{2.77}$$

The essential element of the analysis is a multi-scaling expansion scheme for equation (2.76). Within this scheme, the microscopic and macroscopic time scales t_0 and t_1, respectively, are separated by a dimensionless small parameter ϵ, which is to be specified by a ratio of characteristic scales within the system, e.g., the relaxation time versus a characteristic fluid-dynamic time scale.

With

$$t \;\overset{!}{=}\; t_0+\epsilon^{-1}t_1 \quad , \tag{2.78a}$$

one obtains the time derivative,

$$\partial_t \;=\; \partial_{t_0}+\epsilon\,\partial_{t_1} \quad . \tag{2.78b}$$

For, e.g., $\epsilon = 1/60$ this means, that the time scale t_0 is measured in seconds if the scale t_1 is given in minutes.

Upon introducing expansions in terms of the parameter ϵ for the distribution function $f(\mathbf{r}, \boldsymbol{\zeta}, t)$ and the advanced distribution function $f(\mathbf{r} + \boldsymbol{\zeta}\Delta t, \boldsymbol{\zeta}, t + \Delta t)$,

$$f \overset{!}{=} f^{(0)} + \epsilon f^{(1)} + \epsilon^2 f^{(2)} \tag{2.79a}$$

and

$$f(\mathbf{r} + \boldsymbol{\zeta}\Delta t, \boldsymbol{\zeta}, t + \Delta t) \overset{!}{=} \sum_{n=0} \frac{\epsilon^n}{n!} \mathcal{D}_t^n \, f(\mathbf{r}, \boldsymbol{\zeta}, t) \quad , \tag{2.79b}$$

respectively, with the derivative

$$\mathcal{D}_t := [\partial_t + \boldsymbol{\zeta} \cdot \nabla] \quad , \tag{2.79c}$$

the time-discrete Boltzmann equation (2.76) can be broken down to equations in consecutive orders $\mathcal{O}(\epsilon^n)$:

▷ $\mathcal{O}(\epsilon^0)$:

$$f^{(0)} = \phi \quad , \tag{2.80a}$$

▷ $\mathcal{O}(\epsilon^1)$:

$$\mathcal{D}_{t_0} f^{(0)} = -\frac{1}{\tau} f^{(1)} - F \quad , \tag{2.80b}$$

▷ $\mathcal{O}(\epsilon^2)$:

$$\left\{ \frac{1}{2} \mathcal{D}_{t_0}^2 + \partial_{t_1} \right\} f^{(0)} + \mathcal{D}_{t_0} f^{(1)} = -\frac{1}{\tau} f^{(2)} \quad . \tag{2.80c}$$

In the scheme (2.80), the time step Δt as well as the relaxation time λ thereby are supposed to be of the order ϵ, hence, the dimensionless relaxation time $\tau := \lambda/\Delta t$ is of order one.

At the lowest order $\mathcal{O}(\epsilon^0)$ (2.80a) the local Maxwellian ϕ is associated with the lowest order $f^{(0)}$ of the distribution function. The kinetic behaviour on the time scales t_0 and t_1 at the orders $\mathcal{O}(\epsilon^0)$ (2.80b) and $\mathcal{O}(\epsilon^0)$ (2.80c), respectively, thus is determined by the deviations $f^{(1)}$ and $f^{(2)}$ from the local Maxwellian ϕ. This reflects the structure of the BGK-operator (2.60). The orders $f^{(n>0)}$ therefore have to be constrained such, that they do not contribute to the fluid-dynamic moments, i.e.,

$$\mathcal{M}^{(0)}[\psi^{(\eta)}] \equiv \int d^2\zeta \; \psi^{(\eta)} f^{(0)} \quad , \tag{2.81a}$$

and, following (2.62), the fundamental conservation laws require

$$\int d^3\zeta \; \psi^{(\eta)} \, f^{(n>0)} \overset{!}{=} 0 \quad . \tag{2.81b}$$

Taking the constraints (2.81) into account, the fluid-dynamic level equations for the time scales t_0 and t_1 follow from the fluid-dynamic averaging procedure described in section 2.2. Briefly reviewed, the assignments $q \overset{!}{=} \mathbb{1}$ and $q \overset{!}{=} c_i$ for an arbitrary kernel q in the equations of zeroth moments obtained from (2.80b) and (2.80c) yield the fluid-dynamic level equations,

▷ $\mathcal{O}(\epsilon^1)$:

$$\partial_{t_0}\varrho + \partial_j(\varrho u_j) \quad = \quad 0 \quad , \tag{2.82a}$$

$$\left[\partial_{t_0} + u_j\partial_j\right](\varrho u_i) \quad = \quad -\partial_j\,\varrho c_T^2\delta_{ij} + \varrho a_i \quad , \tag{2.82b}$$

▷ $\mathcal{O}(\epsilon^2)$:

$$\partial_{t_1}\varrho \quad = \quad 0 \quad , \tag{2.83a}$$

$$\varrho\,\partial_{t_1}u_i \quad = \quad \partial_j\Big\{\varrho c_T^2\left(\tau - \frac{1}{2}\right)\big(\partial_j u_i + \partial_i u_j\big)\Big\} \quad . \tag{2.83b}$$

As implied, the microscopic time scale t_0 corresponds to the ballistic regime, i.e., the transport of momentum due to advection is governed by the Euler equations (2.82). The pressure in the momentum balance equation (2.82b),

$$p \; := \; \varrho c_T^2 \quad , \tag{2.84}$$

exactly corresponds to the equation of state (2.48).

The vanishing partial time derivative (2.83a) means that there is no additional mechanism for mass transport in the viscous regime associated with the macroscopic time scale t_1. The transport of momentum due to internal friction is modeled by the dynamic viscosity

$$\mu \; := \; \varrho c_T\left(\tau - \frac{1}{2}\right) \tag{2.85}$$

in the momentum balance equation (2.83b). Via the dimensionless relaxation time $\tau := \lambda/\Delta t$, the viscosity is related to the underlying kinetic operator (2.60).

The orders $\mathcal{O}(\epsilon^1)$ and $\mathcal{O}(\epsilon^2)$ combined result in the complete fluid-dynamic level equations for an isothermal, incompressible system,

$$\partial_t \varrho + \partial_j (\varrho u_j) = 0 \tag{2.86a}$$

$$\varrho \left[\partial_t + u_j \partial_j\right] u_i = -\partial_j \, p_{ij} + \varrho a_i \quad . \tag{2.86b}$$

The stress tensor therein,

$$p_{ij} := p \, \delta_{ij} - \mu \left(\partial_j u_i + \partial_i u_j\right) \quad , \tag{2.87}$$

is formally equivalent to the phenomenological constitutive equation (2.75a).

Chapter 3

The Lattice Boltzmann Approach

Historically, the lattice Boltzmann equation emanated from the evolution equation of the lattice gas cellular automata [35, 36, 79]. In the small Mach number limit, $|\mathbf{u}|/c_T \ll 1$, where the macroscopic velocity $\mathbf{u}$ of fluid motion is small compared to the thermal velocity c_T, it has been shown that the lattice Boltzmann equation is equivalent to a fully discrete version of the continuous Boltzmann equation with the BGK-approximation [56, 80]. The discretization of the phase space in the lattice Boltzmann approach is such, that the positional subspace is discrete by a spatial lattice and the velocity subspace is discrete by the set of velocity vectors which, within one time step, would transfer a particle from a certain site of the positional lattice to one of the neighbouring sites. Two examples of this discretization scheme are given by the unit cells in the figures 3.1 and 3.2. The lattice Boltzmann equation is a designated tool in order to simulate fluid behaviour for very complex situations with high efficiency, since it allows for highly parallel numerical algorithms and an easy implementation of boundary conditions.

There are two prominent numerical implementations of the lattice Boltzmann equation, the so-called Shan-Chen model, named after its developers X. Shan and H. Chen [81–83], and the free-energy model, developed by J. M. Yeomans and collaborators [84–86]. These models have been set up in order to simulate the behaviour of non-ideal fluids, i.e., fluids which in equilibrium would be characterized by a non-ideal equation of state. However, following the description of the continuous Boltzmann equation in chapter 2, the lattice Boltzmann equation per se leads to ideal fluid behaviour in the above sense. In order to obtain non-ideal fluid behaviour, effective particle interactions therefore have been introduced into the lattice Boltzmann equation in the frame of both, the Shan-Chen model and the free energy model.

Conceptually, the free energy model is a top-down approach in the sense that non-ideal fluid behaviour is generated via mean-field arguments on the fluid-dynamic level, from which constraints on the kinetic level governed by the lattice Boltzmann equation arise. Specifically, the stress tensor is derived from a Cahn-Hilliard free energy functional by means of the Noether theorem such, that its diagonal part corresponds to a desired non-ideal equation of state.

The connection to the kinetic level is then established by imposing constraints on the the BGK-operator.

In contrast, the Shan-Chen model has been set up as a bottom up approach in which, analog to the Ising model, a particle interaction is defined on the positional lattice. In the fluid-dynamic limit this interaction results in a potential term within the Navier-Stokes-Fourier stress tensor, which leads to non-ideal fluid behaviour, i.e., intrinsic particle interactions on the kinetic level are modeled by a mean field on the fluid-dynamic level [56].

The discretization scheme leading from the continuous Boltzmann equation to the lattice Boltzmann equation is presented in section 3.1, together with a brief discussion of the corresponding fluid-dynamics level equations. A presentation of the Shan-Chen model and the free energy model follows in the sections 3.2 and 3.3, respectively.

3.1 The lattice Boltzmann equation

The Lattice-Boltzmann equation described in the following is the fully discrete version of the time-discrete BGK-model equation (2.67) in the small Mach number limit,

$$f(\mathbf{r}+\boldsymbol{\zeta}\Delta t,\boldsymbol{\zeta},t+\Delta t)-f(\mathbf{r},\boldsymbol{\zeta},t) \;=\; -\frac{1}{\tau}\left[f(\mathbf{r},\boldsymbol{\zeta},t)-\phi_{|(\mathbf{r},\boldsymbol{\zeta},t)}\right]-F\Delta t \quad , \tag{3.1}$$

with the dimensionless relaxation time $\tau := \lambda/\Delta t$ and the low Mach number expressions for the local Maxwellian (2.68) and the forcing-term (2.72),

$$\phi(\boldsymbol{\zeta},\mathbf{u}) \;=\; \varrho(\mathbf{r})\,\omega(\boldsymbol{\zeta})\left\{1+\frac{1}{c_T^2}(\boldsymbol{\zeta}\cdot\mathbf{u})+\frac{1}{2c_T^4}(\boldsymbol{\zeta}\cdot\mathbf{u})^2-\frac{1}{2c_T^2}\mathbf{u}^2\right\} \tag{3.2a}$$

and

$$F \;=\; -\varrho(\mathbf{r})\,\omega(\boldsymbol{\zeta})\;\mathbf{a}\cdot\left[\frac{1}{c_T^2}(\boldsymbol{\zeta}-\mathbf{u})+\frac{1}{c_T^4}(\boldsymbol{\zeta}\cdot\mathbf{u})\boldsymbol{\zeta}\right] \quad , \tag{3.2b}$$

respectively, see (2.68), (2.72), and (2.69).

More generally, the lattice Boltzmann equation is an explicite finite-difference scheme for the evaluation of the integral solution (2.66) of the BGK-model equation (2.61) in the low Mach number limit.

Discretization in time an phase space

The discretization schema for the six-dimensional phase space, $\mu = \mathrm{span}[\mathbf{r},\boldsymbol{\zeta}]$, which yields the lattice Boltzmann equation as a fully discrete version of (3.1), is depicted by the unit cells in figures 3.1 and 3.2. The continuous variable

$\boldsymbol{\zeta}$ therein is replaced by a set of discrete velocities, $\{\mathbf{c}_\alpha\}$, in which the zero-velocity of particles at rest is contained. The set $\{\mathbf{c}_\alpha\}$ corresponds to the three-dimensional unit cell of the positional lattice in such a way, that the possibilities of particle transfer the set $\{\mathbf{c}_\alpha\}$ offers between neighbouring lattice sites $\mathbf{r}$ and $\mathbf{r} + \Delta\mathbf{r}_\alpha$ within one time step Δt is defined by the relation

$$\Delta\mathbf{r}_\alpha \;=\; \mathbf{c}_\alpha \Delta t \quad . \tag{3.3}$$

The lattice constant a of the cubic unit cells in the figures 3.1 and 3.2 is related to the thermal velocity c_T via [56, 87]

$$\frac{a}{\Delta t} \;=:\; c \;=\; \sqrt{3}c_T \quad . \tag{3.4}$$

Of course, Galilean invariance as well as isotropy per se are broken by any discrete lattice symmetry and these violations show up as higher order error terms in the fluid-dynamic level equations. However, in case of the cubic $D3Q19$- and $D3Q15$-lattices these error terms are negligible in the low Mach number regime underlying the expressions (3.2a) and (3.2b) [56, 88]. In principle, any lattice can be chosen for the phase space discretization, which to a reasonable approximation yields isotropic and Galilean invariant fluid-dynamic level equations.

The phase space discretization described above means that any continuous quantity $q(\mathbf{r}, \boldsymbol{\zeta}, t)$ is replaced by a set $\{q_\alpha(\mathbf{r}, \mathbf{c}_\alpha, t)\}$. The discrete versions of the local Maxwellian (3.2a) and the forcing-term (3.2b) therefore read

$$\phi_\alpha(\mathbf{c}_\alpha, \tilde{\mathbf{u}}) \;=\; \omega_\alpha(\mathbf{c}_\alpha)\varrho_\alpha(\mathbf{r}) \left[1 + \frac{1}{c_T^2}\mathbf{c}_\alpha \cdot \tilde{\mathbf{u}} + \frac{1}{2c_T^4}\left(\mathbf{c}_\alpha \cdot \tilde{\mathbf{u}}\right)^2 - \frac{1}{2c_T^2}\tilde{\mathbf{u}}^2\right] \tag{3.5a}$$

and

$$F_\alpha \;=\; -\omega_\alpha(\mathbf{c}_\alpha)\varrho(\mathbf{r})\left[\frac{1}{c_T^2}\left(\mathbf{c}_\alpha-\mathbf{u}\right)+\frac{1}{c_T^4}\left(\mathbf{c}_\alpha\cdot\mathbf{u}\right)\mathbf{c}_\alpha\right]\cdot\mathbf{a}\quad , \tag{3.5b}$$

respectively, and hence, the phase-space discretization of the time-discrete BGK-model equation (2.76) results in the lattice Boltzmann equation,

$$f_\alpha(\mathbf{r}+\mathbf{c}_\alpha\Delta t, t+\Delta t)-f_\alpha(\mathbf{r},t) \;=\; -\frac{1}{\tau}\left[f_\alpha(\mathbf{r},t)-\phi_\alpha(\mathbf{u})_{|\mathbf{r},t}\right]-F_\alpha\Delta t\quad . \tag{3.6}$$

The fluid-dynamic limit and thermodynamic relations

In order to obtain the fluid-dynamic level equations of the lattice Boltzmann equation (3.6), an integration over the velocity subspace is represented by a summation over the index α. In case of the fluid-dynamic moments one has, e.g.,

$$\mathcal{M}^{(0)}[q] \;:=\; \int d^D\zeta\, qf \quad\longrightarrow\quad \sum_\alpha q_\alpha f_\alpha \tag{3.7a}$$

$$\mathcal{M}_i^{(0)}[q] \;:=\; \int d^D\zeta\;\zeta_i\, qf \quad\longrightarrow\quad \sum_\alpha c_{i,\alpha}\, q_\alpha f_\alpha \tag{3.7b}$$

$$\mathcal{M}_{ij}^{(2)}[q] \;:=\; \int d^D\zeta\;\zeta_i\zeta_j\, qf \quad\longrightarrow\quad \sum_\alpha c_{i,\alpha}c_{j,\alpha}\, q_\alpha f_\alpha\quad . \tag{3.7c}$$

The flud-dynamic level equations of the lattice Boltzmann equation (3.6) are obtained via a Chapman-Enskog analysis as described in section 2.4, followed by a fluid-dynamic averageing procedure as described in 2.2. The fluid-dynamic behaviour in the ballistic regime at the microscopic time scale t_0 is governed by the Euler equations,

$$\partial_{t_0}\varrho + \partial_j(\varrho u_j) = 0 \tag{3.8a}$$

$$\left[\partial_{t_0} + u_j\partial_j\right](\varrho u_i) = -\partial_j\, p\delta_{ij} + \varrho a_i \quad , \tag{3.8b}$$

whereas the full fluid-dynamic behaviour incorporating ballistic as well as viscous effects is governed by the Navier-Stokes equations,

$$\partial_t\varrho + \partial_j\left(\varrho u_j\right) = 0 \tag{3.9a}$$

$$\left[\partial_t + u_j\partial_j\right](\varrho u_i) = -\partial_j\, p_{ij} + \varrho a_i \quad , \tag{3.9b}$$

with the stress tensor p_{ij}, the dynamic viscosity μ, and the equation of state for the pressure p given by the well-know expressions,

$$p_{ij} = p\delta_{ij} + \mu\left(\partial_j u_i + \partial_i u_j\right) \quad , \tag{3.10a}$$

$$\mu = \varrho c_T\left(\tau - \frac{1}{2}\right) \quad , \tag{3.10b}$$

$$p = \varrho c_T^2 \quad . \tag{3.10c}$$

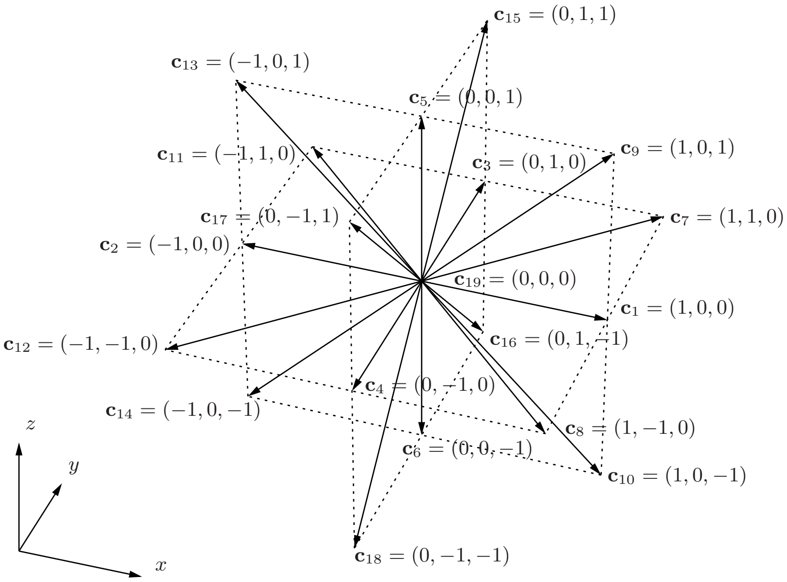
$\mathbf{c}_{15} = (0,1,1)$
$\mathbf{c}_{13} = (-1,0,1)$
$\mathbf{c}_{5} = (0,0,1)$
$\mathbf{c}_{11} = (-1,1,0)$
$\mathbf{c}_{9} = (1,0,1)$
$\mathbf{c}_{3} = (0,1,0)$
$\mathbf{c}_{17} = (0,-1,1)$
$\mathbf{c}_{7} = (1,1,0)$
$\mathbf{c}_{2} = (-1,0,0)$
$\mathbf{c}_{19} = (0,0,0)$
$\mathbf{c}_{1} = (1,0,0)$
$\mathbf{c}_{16} = (0,1,-1)$
$\mathbf{c}_{12} = (-1,-1,0)$
$\mathbf{c}_{4} = (0,-1,0)$
$\mathbf{c}_{14} = (-1,0,-1)$
$\mathbf{c}_{8} = (1,-1,0)$
$\mathbf{c}_{6} = (0,0,-1)$
$\mathbf{c}_{10} = (1,0,-1)$
$\mathbf{c}_{18} = (0,-1,-1)$
z
y
x

Figure 3.1: The set of 19 velocity vectors situated in the xy-plane, the xz-plane, and the yz-plane, defining the $D3Q19$-lattice. The velocities are scaled by $\sqrt{3}c_T$, where c_T is the thermal velocity.

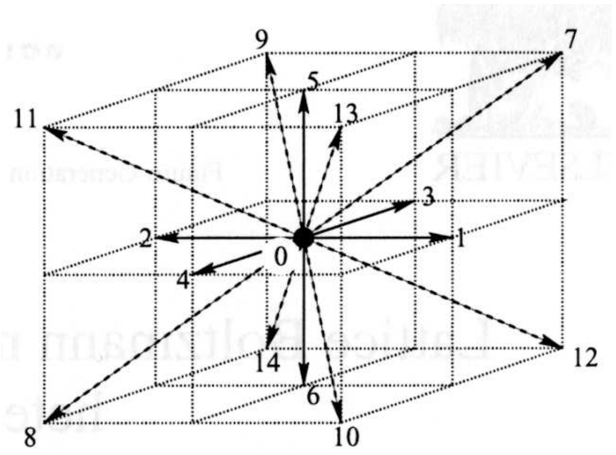
9
7
5
13
11
3
2
1
0
4
12
14
6
8
10

Figure 3.2: The set of 15 velocity vectors defining the $D3Q15$-lattice.

3.2 The Shan-Chen model

The so-called Shan-Chen model is a lattice Boltzmann scheme for the simulation of multi-phase and multi-component fluid flow. Originally developed by X. Shan and H. Chen [81, 82], it was extended later on by H. Chen and B. M. Boghosian [83] in order to model the dynamics of interacting amphiphilic fluids. The key feature of the model is an intrinsic particle interaction, which is given by a self-consistently generated force acting between neighbouring sites of the positional lattice. This intrinsic force is not based on physical considerations on the level of the continuous Boltzmann equation, instead, it is introduced in a phenomenological way into the lattice Boltzmann equation, such that the equation of state on the fluid-dynamic level has a tunable, non-ideal form.

The Shan-Chen model is based on the lattice Boltzmann equation (3.6) for multiple components labeled by σ,

$$f_\alpha^{(\sigma)}(\mathbf{r}+\mathbf{c}_\alpha\Delta t, t+\Delta t)-f_\alpha^{(\sigma)}(\mathbf{r},t) \;=\; -\frac{1}{\tau^{(\sigma)}}\left[f_\alpha^{(\sigma)}(\mathbf{r},t)-\phi_\alpha^{(\sigma)}(\tilde{\mathbf{u}})_{|(\mathbf{r},t)}\right]-F_\alpha^{(\sigma)}\Delta t \quad , \tag{3.11a}$$

with the small Mach number expressions for the local Maxwellian and the external forcing-term,

$$\phi_\alpha^{(\sigma)}(\mathbf{c}_\alpha,\tilde{\mathbf{u}}) \;=\; \omega_\alpha\varrho_\alpha^{(\sigma)}\left[1+\frac{1}{c_T^2}\mathbf{c}_\alpha\cdot\tilde{\mathbf{u}}+\frac{1}{2c_T^4}\left(\mathbf{c}_\alpha\cdot\tilde{\mathbf{u}}\right)^2-\frac{1}{2c_T^2}\tilde{\mathbf{u}}^2\right] \quad , \tag{3.11b}$$

and

$$F_\alpha^{(\sigma)} \;=\; -\omega_\alpha\varrho_\alpha^{(\sigma)}\left[\frac{1}{c_T^2}\left(\mathbf{c}_\alpha-\mathbf{u}\right)+\frac{1}{c_T^4}\left(\mathbf{c}_\alpha\cdot\mathbf{u}\right)\mathbf{c}_\alpha\right]\cdot\mathbf{a}^{(\sigma)} \quad , \tag{3.11c}$$

respectively.

The so-called common velocity $\tilde{\mathbf{u}}$ in (3.11) is defined as the mean velocity of all components weighted by the local particle number,

$$\tilde{\mathbf{u}} := \frac{\sum_\sigma \frac{1}{\tau^{(\sigma)}} \mathcal{M}_i^{(1,\sigma)}[\psi^{(0)}]}{\sum_\sigma \frac{1}{\tau^{(\sigma)}} \mathcal{M}^{(0,\sigma)}[\psi^{(0)}]} = \frac{\sum_\sigma \frac{1}{\tau^{(\sigma)}} \varrho^{(\sigma)} \mathbf{u}^{(\sigma)}}{\sum_\sigma \frac{1}{\tau^{(\sigma)}} \varrho^{(\sigma)}} \quad . \tag{3.12}$$

According to the discrete form (3.7), the fluid-dynamic moments of a quantity $q^{(\sigma)}$ related to the component σ read

$$\mathcal{M}^{(0,\sigma)}[q^{(\sigma)}] = \sum_\alpha q_\alpha^{(\sigma)} f_\alpha^{(\sigma)} \quad , \tag{3.13a}$$

$$\mathcal{M}_i^{(1,\sigma)}[q^{(\sigma)}] = \sum_\alpha c_{\alpha,i}\, q_\alpha^{(\sigma)} f_\alpha^{(\sigma)} \quad , \tag{3.13b}$$

$$\vdots \quad .$$

The number of the fundamental collision invariants $\{\psi^{(\eta)}\}$ (2.11) is multiplied by the number of components and one has

$$\mathcal{M}^{(0,\sigma)}[\psi^{(0)}] = \varrho^{(\sigma)} \quad , \tag{3.14a}$$

$$\mathcal{M}_i^{(1,\sigma)}[\psi^{(0)}] = \varrho^{(\sigma)} \mathbf{u}^{(\sigma)} \quad , \tag{3.14b}$$

$$\vdots \quad .$$

In the frame of the BGK-model, the local conservation of both, the particle number for each type σ and the total momentum of all types, is ensured by constraints on the local Maxwellian $\phi_\alpha^{(\sigma)}$,

$$\mathcal{M}^{(0,\sigma)}[\psi^{(0)}] \; = \; \sum_\alpha f_\alpha^{(\sigma)}(\mathbf{r},t) \; \equiv \; \sum_\alpha \phi_\alpha^{(\sigma)}(\tilde{\mathbf{u}})_{|(\mathbf{r},t)} \quad , \tag{3.15a}$$

and

$$\sum_\sigma \mathcal{M}^{(0,\sigma)}[\psi^{(i)}] \; = \; \sum_\sigma \sum_\alpha c_{\alpha,i}\, f_\alpha^{(\sigma)}(\mathbf{r},t) \; \equiv \; \sum_\sigma \sum_\alpha c_{\alpha,i}\, \phi_\alpha^{(\sigma)}(\tilde{\mathbf{u}})_{|(\mathbf{r},t)} \quad , \tag{3.15b}$$

respectively.

Lattice interactions

Like in the Ising model, one introduces an interaction between neighbouring lattice sites, i.e., between the sites $\{\mathbf{r} + \mathbf{c}_\alpha \Delta t\}$ accessible from a certain site $\mathbf{r}$ within one time step Δt.

The force a particle of type σ on a certain lattice site $\mathbf{r}$ feels due to particles of types $\{\tilde{\sigma}\}$ at the neighbouring sites is defined as [83]

$$\mathbf{F}_{\text{int}}^{(\sigma)}(\mathbf{r},t) \; = \; -\xi^{(\sigma)}_{|(\mathbf{r},t)} \sum_{\{\tilde{\sigma}\}} \sum_\alpha \mathcal{G}_{\sigma\tilde{\sigma}} \xi^{(\tilde{\sigma})}_{|(\mathbf{r}+\mathbf{c}_\alpha \Delta t,t)} \mathbf{c}_\alpha \Delta t \quad . \tag{3.16}$$

The sign of the coupling constant $\mathcal{G}_{\sigma\tilde{\sigma}}$ determines attraction (negative sign) and repulsion (positive sign) between the types σ and $\tilde{\sigma}$, whereas the interaction strength for single particles is given by its absolute value. The non-negative quantity $\xi^{(\sigma)}$ is an effective density as a function of the real particle density $\varrho^{(\sigma)}$,

$$\xi^{(\sigma)} \; \overset{!}{=} \; \xi^{(\sigma)}\big(\varrho^{(\sigma)}\big) \quad . \tag{3.17}$$

It will be shown later on, that the equation of state in the fluid-dynamic limit can be tuned by choosing a certain form for $\xi^{(\sigma)}\left(\varrho^{(\sigma)}\right)$.

The intrinsic force $\mathbf{F}_{\text{int}}^{(\sigma)}$ (3.16) is incorporated into the lattice Boltzmann scheme by adding an increment $\delta\tilde{\mathbf{u}}^{(\sigma)}$ to the common velocity $\tilde{\mathbf{u}}$,

$$\delta\tilde{\mathbf{u}}^{(\sigma)} \;:=\; \frac{\mathbf{F}_{\text{int}}^{(\sigma)}}{\varrho^{(\sigma)}}\lambda^{(\sigma)} \;=\; \mathbf{a}_{\text{int}}^{(\sigma)}\tau^{(\sigma)}\Delta t \quad , \tag{3.18}$$

where $\mathbf{a}_{\text{int}}^{(\sigma)}$ is the acceleration associated with $\mathbf{F}_{\text{int}}^{(\sigma)}$. This means, that the local Maxwellian $\phi_\alpha^{(\sigma)}$ on the right hand side of the lattice Boltzmann equation (3.11) is shifted, i.e.,

$$\begin{aligned} f_\alpha^{(\sigma)}(\mathbf{r}+\mathbf{c}_\alpha\Delta t, t+\Delta t) - f_\alpha^{(\sigma)}(\mathbf{r},t) \;&\overset{!}{=}\; -\frac{1}{\tau^{(\sigma)}}\left[f_\alpha^{(\sigma)}(\mathbf{r},t) - \phi_\alpha^{(\sigma)}(\tilde{\mathbf{u}}+\delta\tilde{\mathbf{u}})_{|(\mathbf{r},t)}\right] \\ =\; -\frac{1}{\tau^{(\sigma)}}\left[f_\alpha^{(\sigma)}(\mathbf{r},t) - \phi_\alpha^{(\sigma)}(\tilde{\mathbf{u}})_{|(\mathbf{r},t)}\right] &- \; F_\alpha^{(\sigma)}\Delta t - \; \mathcal{F}_\alpha^{(\sigma)}\Delta t + \; \mathcal{T}_\alpha^{(\sigma)}\Delta t^2 \quad . \end{aligned} \tag{3.19a}$$

The second line of (3.19a) shows, that the velocity shift of the local Maxwellian due to the intrinsic force $\mathbf{F}_{\text{int}}^{(\sigma)}$ is equivalent to a modification of the original lattice Boltzmann equation (3.11) by additional terms

$$\mathcal{F}_\alpha^{(\sigma)} \;=\; -\omega_\alpha\varrho^{(\sigma)}\left[\frac{1}{c_T^2}\left(\mathbf{c}_\alpha - \tilde{\mathbf{u}}\right) + \frac{1}{c_T^4}\left(\mathbf{c}_\alpha\cdot\tilde{\mathbf{u}}\right)\mathbf{c}_\alpha\right]\cdot\mathbf{a}_{\text{int}}^{(\sigma)} \tag{3.19b}$$

and

$$\mathcal{T}_\alpha^{(\sigma)} \;=\; -\frac{1}{2}\omega_\alpha\varrho^{(\sigma)}\left[\frac{1}{c_T^2}\mathbf{a}_{\text{int}}^{(\sigma)2} - \frac{1}{c_T^4}\left(\mathbf{c}_\alpha\cdot\mathbf{a}_{\text{int}}^{(\sigma)}\right)^2\right]\tau^{(\sigma)} \quad . \tag{3.19c}$$

A comparison of expression (3.19b) and the forcing-term (3.2b) shows, that, to the order $\mathbf{a}_{\mathrm{int}}^{(\sigma)}$, an incorporation of intrinsic particle interactions into the lattice Boltzmann equation as described above is formally equivalent to an applied external body force field in the low Mach number limit. This means that for sufficiently small absolute values of $\mathbf{a}_{\mathrm{int}}^{(\sigma)}$, i.e., $(\mathbf{a}_{\mathrm{int}}^{(\sigma)})^2 \to 0$ in (3.19c), the form of the particle interactions in the Shan-Chen model corresponds to a mean field approximation.

Fluid dynamics and equilibrium properties

For a one component system[1] and the neglect of the term $\mathcal{T}_\alpha$ (3.19c), the Chapman-Enskog analysis of equation (3.19a) as described in section 2.4, followed by a fluid-dynamic averageing procedure as described in 2.2, yields the fluid-dynamic level equations [81, 82],

$$\partial_t \varrho + \nabla \cdot (\varrho \mathbf{u}) \;=\; 0 \tag{3.20a}$$

and

$$\varrho \left[\partial_t + \mathbf{u} \cdot \nabla\right] \mathbf{u} \;=\; -\nabla \left(\frac{(1-d_0)}{D} c_T^2 \varrho \right) + \nabla \cdot (\mu \nabla \mathbf{u}) + \varrho \mathbf{a} + \varrho \mathbf{a}_{\mathrm{int}} \quad . \tag{3.20b}$$

In (3.20b), d_0 denotes the equilibrium fraction of particles with zero speed, D is the dimension, and the shear viscosity is given by

$$\mu \;=\; \varrho c_T \left(\tau - \frac{1}{2} \right) \quad . \tag{3.21}$$

---

[1] Since $\sigma \equiv \tilde{\sigma}$ the indices σ and $\tilde{\sigma}$ will be skipped in the following

The intrinsic particle interaction $\mathbf{F}_{\text{int}}$ appears as a mean field forcing-term $\varrho\mathbf{a}_{\text{int}}$ in the momentum balance equation (3.20b), while the shear viscosity μ (3.21) is independent of $\mathbf{F}_{\text{int}}$. Expanding the effective density ξ in $\mathcal{F}_\alpha$ (3.19b) up to the linear order in the lattice constant, i.e.,

$$\xi(\mathbf{r} + \mathbf{c}_\alpha \Delta t) \overset{!}{\approx} \xi(\mathbf{r}) + \nabla\xi \cdot \mathbf{c}_\alpha \Delta t \quad , \tag{3.22}$$

the mean field forcing-term $\varrho\mathbf{a}$ can be interpreted as a discrete gradient,

$$\varrho\mathbf{a}_{\text{int}} = -\nabla \frac{b}{2D} \mathcal{G} c_T^2 \xi^2 =: -\nabla V \quad , \tag{3.23}$$

which leads to a non-ideal equation of state in the momentum balance equation (3.20b),

$$p := \frac{(1-d_0)}{D} c_T^2 \varrho + V \quad . \tag{3.24a}$$

In the weak interaction limit, $\mathcal{G} \to 0$, the equation of state (3.24a) approaches an ideal form with

$$\frac{(1-d_0)}{D} c_T^2 = \frac{(1-d_0)}{D} \frac{k_B T}{m} \tag{3.24b}$$

as a temperature scale. This temperature scale does not match the width c_T^2 of the equilibrium distribution function (2.19), which appears as a scaling parameter in the small Mach number expansion (3.11b). Nevertheless, the equation of state (3.24a) is consistent if the equilibrium fraction of resting particles, d_0, does not vary in space.

For $\mathcal{G} \neq 0$, the non-ideal part of the equation of state (3.24a),

$$V = \frac{b}{2D} \mathcal{G} c_T^2 \xi^2 \tag{3.24c}$$

specifies the equilibrium properties of the system. The choice

$$\xi(\varrho) \overset{!}{=} \xi_0 \left(1 - \exp\left[-\varrho/\varrho_0\right]\right) \tag{3.25}$$

with arbitrary constants ξ_0 and ϱ_0 leads to a van der Waals loop for (3.24a).

Wetting

As explained in section 1.1, the wetting behaviour of two fluid components on a solid substrate in principle arises from an interplay of cohesive fluid-fluid and adhesive fluid-substrate interactions.

In the frame of the Shan-Chen model, the wetting behaviour thus is determined by the sets of coupling constants and effective densities, $\{\mathcal{G}_{\sigma\tilde{\sigma}}\}$, $\{\xi^{(\sigma)}\}$, and $\{\xi^{(\tilde{\sigma})}\}$, respectively, within the intrinsic force $\mathbf{F}_{\mathrm{int}}^{(\sigma)}(\mathbf{r},t)$ (3.16) between particles of the type σ and particles of other types $\{\tilde{\sigma}\}$,

$$\mathbf{F}_{\mathrm{int}}^{(\sigma)}(\mathbf{r},t) = -\xi^{(\sigma)}_{|(\mathbf{r},t)} \sum_{\{\tilde{\sigma}\}} \sum_{\alpha} \mathcal{G}_{\sigma\tilde{\sigma}} \xi^{(\tilde{\sigma})}_{|(\mathbf{r}+\mathbf{c}_\alpha \Delta t, t)} \mathbf{c}_\alpha \Delta t \quad . \tag{3.26}$$

Cohesive fluid-fluid and adhesive fluid-substrate interactions thereby correspond to a negative sign of the corresponding coupling constants, whereas a positive sign of the latter would correspond to a repulsive interaction.

Technically, a planar solid substrate can be modeled by a layer of particles which are pinned to their lattice sites, i.e, the distribution function for the zero velocity for the solid component is fixed to a constant value at a certain layer of lattice sites, while the distribution functions for non-zero velocities vanish. A no-slip boundary condition at the substrate then is obtained by means of a particle bounce-back [34, 89, 90], which means that particles arriving at the substrate layer at a certain time-step are sent back to the lattice point they came from in a consecutive time-step, instead of undergoing specular reflection.

There is no means of defining interfacial tensions in the Shan-Chen model, i.e, the macroscopic contact angle θ of a sessile droplet on a homogeneous substrate is not a direct input parameter. Measured geometrically from simulation results, it can be related to a certain initial set of coupling constants and effective densities, $\{(\mathcal{G}_{\sigma\tilde{\sigma}}, \xi^{(\sigma)}, \xi^{(\tilde{\sigma})})\}$.

Naively, a sessile droplet on a solid substrate surrounded by a different fluid component would correspond to a three-component system. However, the interplay of cohesive fluid-fluid and adhesive fluid-substrate interactions leading to a certain macroscopic contact angle can be modeled effectively by means of a two-component system, in which particles of the same type do not interact whereas particles of different types have a repulsive interaction, i.e, $\mathcal{G}_{\sigma\sigma} \equiv 0$ and $\mathcal{G}_{\sigma\tilde{\sigma}} > 0$. A way to implement such a system of two immiscible fluids on a chemically patterned solid substrate by specifying two different components only is described in section 4.2.

3.3 The free energy model

The free energy model is a lattice Boltzmann scheme developed by J.M. Yeomans and collaborators in order to model the dynamics of phase separation and two phase fluid flow. The model is a top-down approach in the sense that, following the Cahn-Hilliard theory of non-equilibrium dynamics [59, 64, 91, 92], the stress tensor on the fluid-dynamic limit is constructed from a free energy density Ψ as a function of the particle density ϱ.

The free energy density $\Psi(\varrho)$ is chosen in the frame of the van der Waals theory of quasi-local thermodynamics, i.e.,

$$\Psi(\varrho) \;=\; \Psi_b(\varrho, T) + \frac{\kappa}{2}|\partial_k \varrho|^2 \quad . \tag{3.27}$$

where $\Psi_b(\varrho, T)$ is the bulk free energy density and the gradient term describes the contribution necessary to build up an interface within the system. The integral of $\Psi(\varrho)$ over the fluid volume is minimized by the equilibrium density. The bulk free energy density,

$$\Psi_b(\varrho, T) \;=\; W(\varrho, T) - p_b(T) + \mu_b(T)\varrho \quad , \tag{3.28}$$

incorporates an excess free energy density $W(\varrho, T)$, the bulk pressure $p_b(T)$, and the chemical potential of the bulk, $\mu_b(T)$. The excess free energy density $W(\varrho, T)$ has a double well structure with respect to the density ϱ such, that both $W(\varrho)$ and its partial derivative vanish in the bulk,

$$W(\varrho)_{|\varrho_b} \;=\; 0 \quad , \tag{3.29a}$$

$$\partial_\varrho W(\varrho)_{|\varrho_b} \;=\; 0 \quad . \tag{3.29b}$$

The connection to the underlying kinetic level is established by imposing constraints on the fluid-dynamic moments obtained from the single-particle phase space distribution function f such, that the desired fluid-dynamic level equations are obtained.

The free energy model is based on the single-component lattice Boltzmann equation[2]

$$f_\alpha(\mathbf{r}+\mathbf{c}_\alpha\Delta t, t+\Delta t) - f_\alpha(\mathbf{r},t) \;=\; -\frac{1}{\lambda}\left[f_\alpha(\mathbf{r},t) - \phi_\alpha\left(\mathbf{c}_\alpha, \mathbf{u}\right)_{|(\mathbf{r},t)}\right]\Delta t \quad . \qquad (3.30)$$

The local Maxwellian ϕ_α is given by an expansion in the local velocity $\mathbf{u}$,

$$\phi_\alpha \;\overset{!}{=}\; \frac{A_\alpha}{c_T^2} + \frac{B_\alpha}{c_T^2}\left(\boldsymbol{\zeta}_\alpha \cdot \mathbf{u}\right) + \frac{C_\alpha}{c_T^2}\mathbf{u}^2 + \frac{D_\alpha}{c_T^4}\left(\boldsymbol{\zeta}_\alpha \cdot \mathbf{u}\right)^2 + \frac{G_{\alpha,ij}}{c_T^4}\zeta_{\alpha,i}\zeta_{\alpha,j} \quad , \qquad (3.31)$$

where, according to (2.51), the thermal velocity c_T is proportional to the lattice constant. The coefficients, A_α, B_α, C_α, and $G_{\alpha,ij}$, within the expansion (3.31) are determined via the fluid dynamic moments of the fundamental collision invariants $\{\psi^{(\eta)}\}$ (2.11),

$$\mathcal{M}^{(0)}\left[\psi^{(0)}\right] \;=\; \varrho \quad , \qquad (3.32a)$$

$$\mathcal{M}^{(0)}\left[\psi^{(i)}\right] \;=\; \varrho u_i \quad , \qquad (3.32b)$$

$$\mathcal{M}_i^{(1)}\left[\psi^{(j)}\right] \;=\; P_{ij} + \varrho u_i u_j \quad , \qquad (3.32c)$$

$$\mathcal{M}_{ij}^{(2)}\left[\psi^{(k)}\right] \;=\; \frac{1}{3}\varrho\left(u_i\delta_{jk} + u_j\delta_{ik} + u_k\delta_{ij}\right) \quad . \qquad (3.32d)$$

---

[2] A forcing-term due to an external field is not taken into account in the following.

In the framework of the BGK-model, the above fluid-dynamic moments correspond to constraints on the local Maxwellian ϕ_α, i.e, according to (2.62),

$$\begin{aligned} \mathcal{M}^{(0)}[\psi^{(\eta)}] \quad &:= \sum_\alpha \psi_\alpha^{(\eta)} f_\alpha \;\equiv\; \sum_\alpha \psi_\alpha^{(\eta)} \phi_\alpha \quad , && \text{(3.33a)} \\ \mathcal{M}_i^{(1)}[\psi^{(\eta)}] \quad & \dots \quad , && \text{(3.33b)} \\ \vdots \qquad & \qquad . \end{aligned}$$

The free energy density $\Psi(\varrho)$ enters into this scheme via the stress tensor P_{ij} in (3.32c). Following Cahn-Hilliard theory, the stress tensor reads

$$P_{ij} \;\overset{!}{=}\; \Pi_{ij}[\psi] + \mu\,(\partial_j u_i + \partial_i u_j) \quad . \tag{3.34a}$$

Since the free energy density Ψ does not explicitely depend on the positional degrees of freedom, the tensor Π_{ij} follows from the Noether theorem, i.e.,

$$\Pi_{ij}[\psi] \;\overset{!}{=}\; \left[\delta_{ij} - (\partial_i\varrho)\,\partial_{(\partial_j\varrho)}\right](\Psi - \mu_b\varrho) \;=\; \tilde{p}\delta_{ij} + \kappa(\partial_i\varrho)(\partial_j\varrho) \quad , \tag{3.34b}$$

where

$$\tilde{p} \;=\; p - \kappa\varrho\,\partial_i^2\varrho - \frac{\kappa}{2}(\partial_i\varrho)^2 \quad . \tag{3.34c}$$

The expression $\tilde{p}$ (3.34c) is the local pressure and the quantity p therein is associated with the bulk free energy density Ψ_b via Legendre transformation,

$$p \;\overset{!}{=}\; \left(1 - \varrho\frac{d}{d\varrho}\right)\Psi_b \quad . \tag{3.35}$$

Hence, in the equilibrium case one has $p = p_b$ in the bulk regions, according to (3.27), (3.28), and (3.29), and the conservation of momentum takes the form $\partial_i \Pi_{ij} = 0$.

In the low Mach number regime, the fluid-dynamic momentum equation obtained from the lattice Boltzmann equation reads [88]

$$\varrho \left[\partial_t + u_j \partial_j\right] u_i \;=\; -\partial_j \left\{\Pi_{ij} - \mu \left(\partial_j u_i + \partial_i u_j\right)\right\} \quad , \tag{3.36}$$

with the dynamic viscosity,

$$\mu \;=\; \varrho c_T \left(\tau - \frac{1}{2}\right) \quad , \tag{3.37}$$

equivalent to the expression (2.85).

Wetting

The local interfacial tension σ_{ff} of an interface separating two fluids in equilibrium may be obtained via an integration of the free energy density Ψ_b along the direction $r_\perp$ perpendicular to the interface,

$$\sigma_{\mathrm{ff}} \;:=\; \int dr_\perp \left\{ \Psi_b(\varrho, T) + \frac{\kappa}{2} |\partial_k \varrho|^2 \right\}_{\mathrm{eq}} \quad . \tag{3.38}$$

In order to model the formation of a three-phase contact line due to the presence of a solid substrate, the surface free energy density of the solid $\Psi_s(\varrho_s)$ has to be taken into account, which, according to the Cahn theory [93, 94], is given by an expansion in powers of the fluid density ϱ_s at the substrate.

In the free energy model, the linear order is taken into account exclusively,

$$\Psi_s(\varrho_s) \;:=\; -p_\mathrm{w}\varrho_s \quad , \tag{3.39a}$$

where the constant p_w is called the wetting potential.

Accordingly, the general expression for the solid-fluid interfacial tension is

$$\sigma_\mathrm{sf} \;:=\; \left[\, \int dr_\perp \left\{ \Psi_b(\varrho, T) + \frac{\kappa}{2}|\partial_{r_\perp}\varrho|^2 \right\} \;+\; p_\mathrm{w}\varrho_s \,\right]_\mathrm{eq} \quad . \tag{3.39b}$$

The minimization of the kernel in (3.39b) with respect to the fluid density ϱ yields an Euler-Lagrange equation for the fluid region,

$$\partial_\varrho \Psi_b \;-\; \kappa\,(\partial^2_{r_\perp}\varrho) \;\overset{!}{=}\; 0 \quad , \tag{3.40a}$$

and a natural boundary condition [93, 94] on the substrate,

$$\kappa\,(\partial_{r_\perp}\varrho) \;\overset{!}{=}\; \frac{d\Psi_s}{d\varrho_s} \;=\; -p_\mathrm{w} \quad . \tag{3.40b}$$

By means of a first integral of (3.39a) and the boundary condition (3.39b), the density ϱ_s follows from the wetting potential p_w, and thus, the solid-fluid interfacial tension σ_sf and the fluid-fluid (liquid-gas) interfacial tension σ_{lg} are specified by the wetting potential p_w, the bulk free energy density Ψ_b, and the bulk density of the fluid ϱ_b, i.e.,

$$\sigma_\mathrm{sf} \;=\; -p_\mathrm{w}\varrho_s \;+\; \int_{\varrho_b}^{\varrho_s} d\varrho\;\sqrt{2\kappa\Psi_b} \quad , \tag{3.41a}$$

and

$$\sigma_{\mathrm{lg}} \;=\; \int_{\varrho_g}^{\varrho_s} d\varrho\, \sqrt{2\kappa\Psi_b} \quad . \tag{3.41b}$$

According to the relations (3.41) and Young 's Law (1.7b), the macroscopic contact angle θ plays the role of an input parameter within the free energy model.

Chapter 4

Macroscopic Fluid Properties

In the following, the numerical determination of fluid morphologies on chemical channels is presented. The calculations include both, the formation of equilibrium morphologies, and the morphologic behaviour in the presence of driving body forces. The length-scale regime is defined by (1.3), i.e., the equilibrium morphologies are well described by the capillary model.

Inspired by the detection of a morphologic transition of fluid droplets on straight chemical channels [38–41], the equilibrium morphologies of fluid droplets on straight and branched chemical channels have been investigated based on the free energy (1.5),

$$F = \underbrace{\int dA_{lg}\, \sigma_{lg} + \int dA_{sl}\, (\sigma_{sl} - \sigma_{sg})}_{:=\tilde{F}} - \Delta p \int dV_l \quad , \tag{4.1}$$

i.e., the interfacial free energy $\tilde{F}$ is minimized under the constraint of a fixed fluid volume V_l by means of the finite element algorithm described in section 1.3.

Under certain conditions, the morphologic behaviour of a fluid droplet on a straight chemical channel is more complex than it might appear at first sight. If the fluid volume and the wettability on the channel are chosen such, that a sufficiently large part of the three-phase contact line is pinned at the channel edges, the minimization problem of the interfacial free energy exhibits a bifurcation depending on the fluid volume and the wettability on the channel, which means that the droplet may undergo a so-called morphologic transition. This scenario is shown to be a matter of the smoothness of the channel edges, i.e., the smoothness of a corresponding wettability profile.

The morphologic transition matters if the fluid is placed in the vicinity of a junction of chemical channels. In terms of the interfacial free energy $\tilde{\mathcal{F}}$, this may be explained by the topology of the energetic landscape with respect to the lateral coordinates the fluid is subject to at the junction.

The relaxation and the driven dynamics of fluid droplets on chemical channels have been investigated by means of lattice Boltzmann simulations. The algorithm used is based on a numerical implementation of the Shan-Chen model

[83, 87, 95, 96] described in section 3.2. In the lattice Boltzmann simulations on the relaxation of fluid droplets on straight chemical channels, the abovementioned bifurcation detected in the free energy approach was reproduced qualitatively. The simulations of fluid droplets driven by an external body force reveal a morphologic behaviour which is reminiscent of the Landau-Levich effect [97–100].

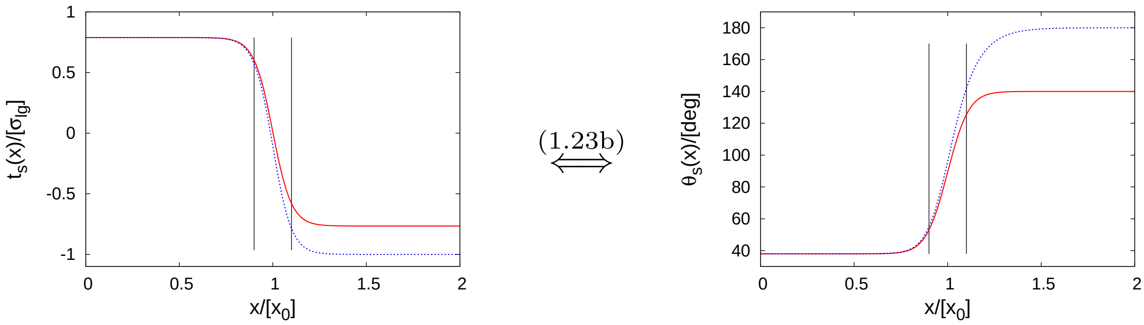

Figure 4.1: Chemical steps modeled by smooth wettability profiles $t_s(x)$ of the line integral kernel (1.23b) according to (4.3). The profiles $t_s(x)$ translate into corresponding profiles $\theta_s(x)$ of the macroscopic contact angle. The wettability contrast corresponds to plateau values $\theta_{\text{phob}} = 140^\circ$ and $\theta_{\text{phob}} = 180^\circ$, and the common plateau value corresponds to $\theta_{\text{phil}} = 38^\circ$. The smoothness is $s/[w] = 0.05$ and the range $[x - f(y)] = \pm s$ is marked by the black vertical lines.

4.1 Morphologic transitions on chemical channels

Numerical calculations of the equilibrium morphology of fluid droplets on straight and branched chemical channels are presented within this section. A straight chemical channel is defined by two parallel, confining chemical steps. In terms

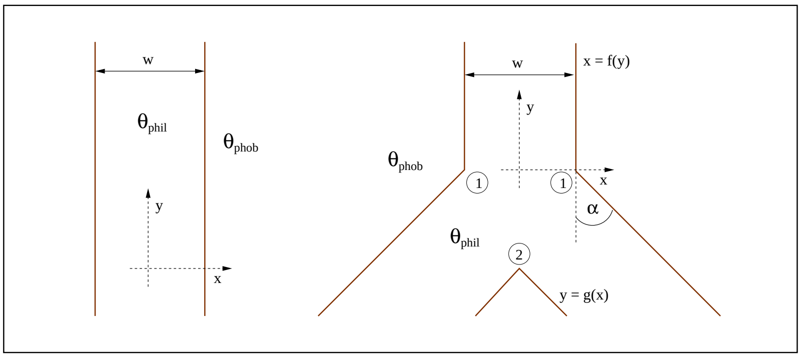

Figure 4.2: Sketch of the channel geometries in the xy-plane. The parameters θ_{phil} and θ_{phob} correspond to the plateau values of the macroscopic contact angle. The transtion between the plateau values which characterizes the channel edges may be given by (4.2) or (4.3), i.e., the edges may be sharp or smooth, respectively. The opening angle α of the y-junction is 45°. The shape of the corners (1) and (2) is determined by the parameters b and c in (4.4).

---

of the interfacial free energy $\tilde{F}$ (1.23a), a chemical step is represented by a modification of the line integral kernel $\mathbf{k}$ (1.23b) such, that the expression $t := (\sigma_{lg}/x)\mathbf{k}\cdot\mathbf{e}_y = \sigma_{lg}\cos\theta$ interpolates between a lyophilic plateau value t_{phil} and a lyophobic plateau value t_{phob}.

In the discontinuous border case, the wettability profile is given by a jump

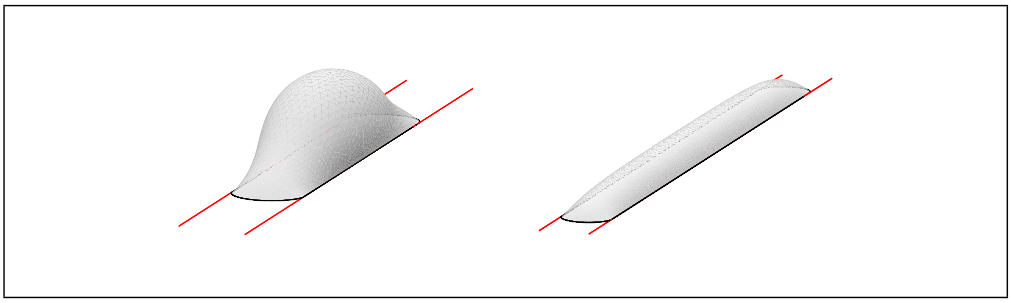

Figure 4.3: Stable bulge-like and metastable ridge-like morphology on a sharp chemical channel. The lyophilic contact angle and the specific volume are $\theta_{\mathrm{phil}} = 38°$ and $V_l/[w^3] = 4.0$, respectively. The configurations are obtained via the numerical minimization of the interfacial free energy $\tilde{F}$ (1.23a) as an output of the finite element algorithm described in section 1.3. The channel edges are indicated by the red lines and the black line indicates the three-phase contact line.

$\Delta t := t_{\mathrm{phob}} - t_{\mathrm{phil}}$ between the plateau values t_{phil} and t_{phob}, i.e.,

$$t(x,y) \overset{!}{=} t_{\mathrm{phil}} + \Delta t\, \Theta\big(x - f(y)\big) \quad , \tag{4.2}$$

where the analytic function $x = f(y)$ parameterizes the position of the step in the xy-plane. A smooth wettability transition can be parameterized by

$$t_s(x,y) = t_{\mathrm{phil}} + \frac{\Delta t}{2} \left\{ \tanh\left[\frac{(x - f(y))}{s} \right] + 1 \right\} \quad , \tag{4.3}$$

where $s = |x - f(y)|$ defines the range in which the slope of the profile can chosen to be constant. The parameter s thus is a measure for the smoothness of a channel edge. According to (1.23b) the profile $t_s(x)$ translates into a profile $\theta_s(x)$ for the macroscopic contact angle with plateau values θ_{phil} and θ_{phob}, see figure 4.1. Concisely, chemical channel edges modeled by (4.2) and (4.3) are called “sharp” and “smooth”, respectively.

The investigated channel patterns are depicted in figure 4.2. In case of the y-shaped junction one has

$$f(y) \;=\; \frac{b}{2}\left(\sqrt{1+\left(\frac{y}{b}\right)^2}\right)\tan\alpha + \frac{w}{2} \tag{4.4a}$$

and

$$g(x) \;=\; -c\sqrt{1+\left(\frac{y}{c}\right)^2}\tan\alpha - w\left(\frac{1}{\sin\alpha} + \frac{1}{2\tan\alpha}\right) \quad , \tag{4.4b}$$

where the parameters b and c define the shape of the corners (1) and (2), respectively.

The uniform channel width w serves as a scaling parameter, hence, the specific liquid volume on a chemical channel and the relative smoothness of the channel edges are defined as $V_l/[w^3]$ and $s/[w]$, respectively. The parameter space for the investigation of liquid morphologies on straight chemical channels is spanned by $V_l/[w^3]$, $s/[w]$, and the lyophilic contact angle θ_{phil}.

Droplets on straight chemical channels

The geometrically simplest system to look at is a straight chemical channel with sharp edges, a so-called sharp channel. For a lyophilic contact angle $\theta_{\text{phil}} = 38^\circ$ and a specific liquid volume $V_l/[w^3] = 4.0$, the configurations shown in figure 4.3 are the equilibrium liquid morphologies on such a channel.

The bulge-like morphology on the left is energetically stable whereas the ridge-like morphology on the right is metastable, i.e., these morphologies correspond to a global and a local minimum of $\tilde{F}$, respectively. In case of a specific volume $V_l/[w^3] = 3.0$ however, the situation changes and a ridge-like morphology is the only stable configuration.

In order to unfold this energetic behaviour, the interfacial free energy $\tilde{F}$ is minimized under the additional constraint of a fixed center of mass height, denoted $\bar{z}$, where the substrate at $z = 0$ is the plane of reference. The constraint on the center of mass corresponds to a homogeneous body force acting in the z-direction perpendicular to the substrate. Hence, fixing $\bar{z}$ successively during the minimization of $\tilde{F}$ means pushing or pulling the liquid onto or away from the substrate.

In figure 4.4, the interfacial free energy $\tilde{F}$ (4.1) as a function of $\bar{z}$ is shown for different values of the specific volume, $3.0 \leq V_l/[w^3] \leq 4.0$. The two well pronounced energetic minima in the graph for $V_l/[w^3] = 4.0$ correspond to the equilibrium morphologies shown in figure 4.3.

Starting from large values, the change of $\tilde{F}$ as a function of $\bar{z}$ for decreasing values of $V_l/[w^3]$ illustrates the morphologic transition between bulge-like and ridge-like morphologies, i.e., stable bulges at $V_l/[w^3] = 4.0$ first become metastable and finally unstable, while simultaneously the ridges switch from metastability at $V_l/[w^3] = 4.0$ to stability at $V_l/[w^3] = 3.0$. The position of the energetic minima of the ridge-like morphologies hardly depends on $\bar{z}$, which means that the ridges only become longer when increasing $V/[w^3]$. For very large values of $V/[w^3]$, however, the ridges become unstable.

Based on this scenario for a fixed lyophilic contact angle θ_{phil}, the bifurcation diagramm in figure 4.5 gives the regions of stability and metastability of liquid bulges and ridges on a sharp chemical channel in the parameter space spanned by θ_{phil} and $V_l/[w^3]$, [40, 41].

The line marked by θ_* separates the region of stable ridges (II) from the region of stable bulges (III), i.e., $\tilde{F}$ as a function of $\bar{z}$ has two equally deep minima on this line. In the regions between the line marked by θ_* and the border lines marked by θ_{bu} and θ_{ch}, the bulge-like and ridge-like morphologies, respectively, are metastable. On these border lines no local minimum exists, instead, $\tilde{F}$ is characterized by an inflection point and a single global minimum. Hence, only one stable configuration exists, either bulge-like or ridge-like. Beyond, $\tilde{F}$ has only one global minimum. In the region (I) corresponding to low specific volumes $V_l/[w^3]$, the liquid collects in spherical caps, which do not touch the channel edges. The plots of the interfacial free energy $\tilde{F}$ as a function of $\bar{z}$ may be seen as a deconvolution of the bifurcation diagram along an axis of constant θ.

The analysis of the interfacial free energy $\tilde{\mathcal{F}}$ for smooth channel edges modeled by (4.3) shows, that the morphologic transition is strongly influenced by the relative smoothness $s/[w]$. The impact of $s/[w]$ on the interfacial free energy $\tilde{F}$ as a function of $\bar{z}$ is shown in figures 4.6 and 4.7. Enhancing $s/[w]$ destabilizes the ridges, i.e., there is a gain in interfacial free energy accompanied by a disappearance of the energy barrier with respect to liquid bulges.

Figure 4.6 illustrates the destabilization of an initially metastable ridge with a specific volume $V_l/[w^3] = 4.0$, and figure 4.7 illustrates the same for an initially stable ridge with $V_l/[w^3] = 3.0$. In principle, this can be understood by means of the border case $s \to \infty$ of infinitely smooth channel edges. This case asymptotically approximates a homogeneous substrate on which the equilibrium liquid morphology has the shape of a spherical cap and liquid ridges are not stable. However, this point of view is not very satisfying since the relative smoothness $s/[w]$ needed to destabilize the ridges is rather far from this border case. Instead, it is more instructive to have a look at the behaviour of the three-phase contact line. The figure 4.8 shows the three-phase contact lines at the tongue of liquid ridges for different values of the relative smoothness $s/[w]$, and for specific volumina $V_l/[w^3] = 3.0$ and $V_l/[w^3] = 4.0$. The parameters in figure 4.8 correspond to the parameters in the figures 4.6 and 4.7 , i.e., the ridges correspond to the left minima. The channel is aligned with the y-axis, which means that the channel edges are at $x = \pm w/2$ and the niveau $x = 0$ corresponds to the longitudinal symmetry axis of the channel.

In the case of sharp channel edges, the three-phase contact line is pinned at the channel edge, i.e., it exactly follows the edge at $x = w/2$ and it exhibits a kink when entering the channel area. The contact angle at the pinned part of the three-phase contact line may take any value between θ_{phil} and θ_{phob}.

In the case of a smooth wettability profile $\mathbf{t}_s(x)$, the three-phase contact line depins from the edge for increasing values of the relative smoothness $s/[w]$, i.e., it does not follow the niveau $x = w/2$ any longer.

The depinning of the three-phase contact line has two effects. Firstly, the contact angle along the entire three-phase contact line is given by the locally varying contact angle $\theta_s(x)$, and secondly, the specific volume effectively increases for increasing values of the smoothness $s/[w]$, since the ridges are compressed at the base. For $V_l/[w^3] = 4.0$ and $s/[w] = 1/50$ the effective value of the specific volume is approximated by $V_l/[(0.9w)^3] \approx 5.487$. A look on the bifurcation diagram 4.5 shows, that this effective increase of the specific volume by itself does not cause the ridge to be unstable. Hence, the local contact angle profile $\theta_s(x)$ has to be taken into account in order to explain the instability.

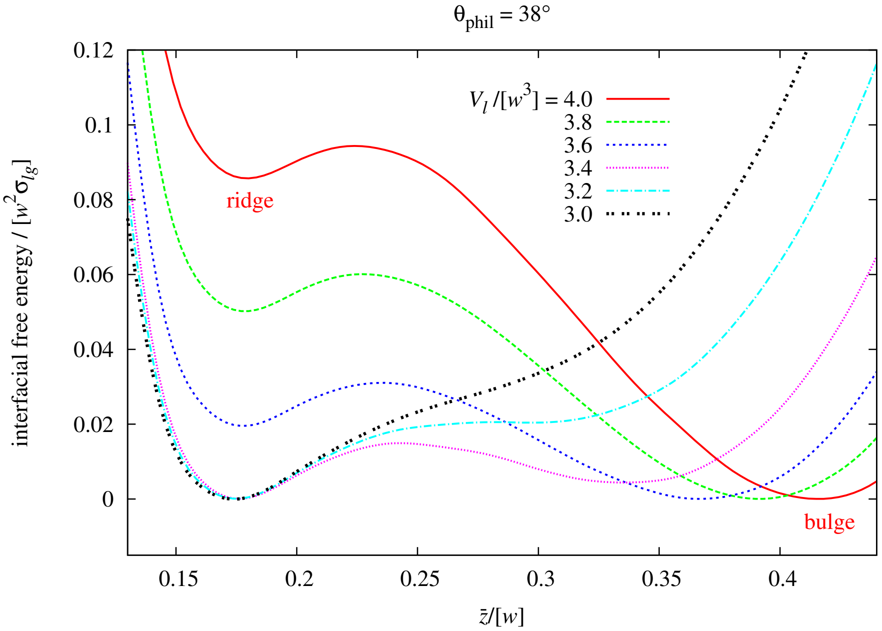

Figure 4.4: Morphologic transition between bulge-like and ridge-like liquid morphologies on a sharp chemical channel illustrated by the behaviour of the interfacial free energy $\tilde{F}$ with respect to the center of mass height $\bar{z}$ for different specific volumina $V_l/[w^3]$ and a fixed contact angle $\theta = 38°$. Equivalent calculations are described in [40, 41].

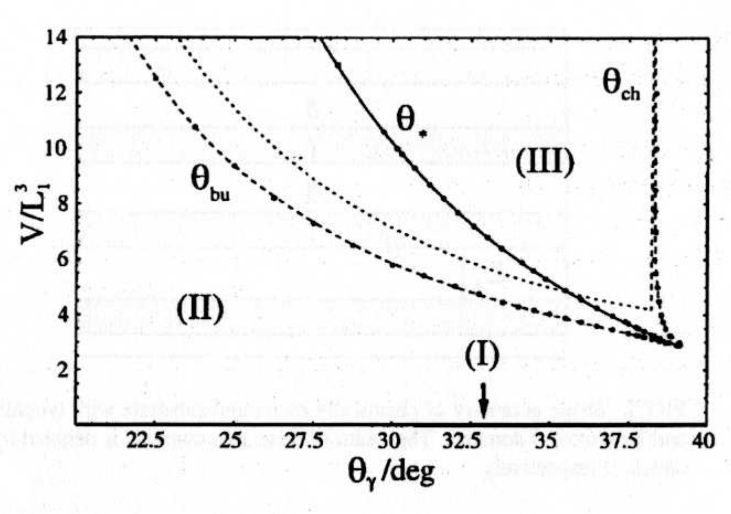

Figure 4.5: Bifurcation diagram [40, 41] displaying the regions of (meta)stability of liquid ridges (II) and bulges (III) in the parameter space spanned by the lyophilic contact angle and the specific volume. The figure 4.4 unfolds this diagram along the ordinate at $\theta_{\rm phil} \equiv \theta_\gamma = 38°$

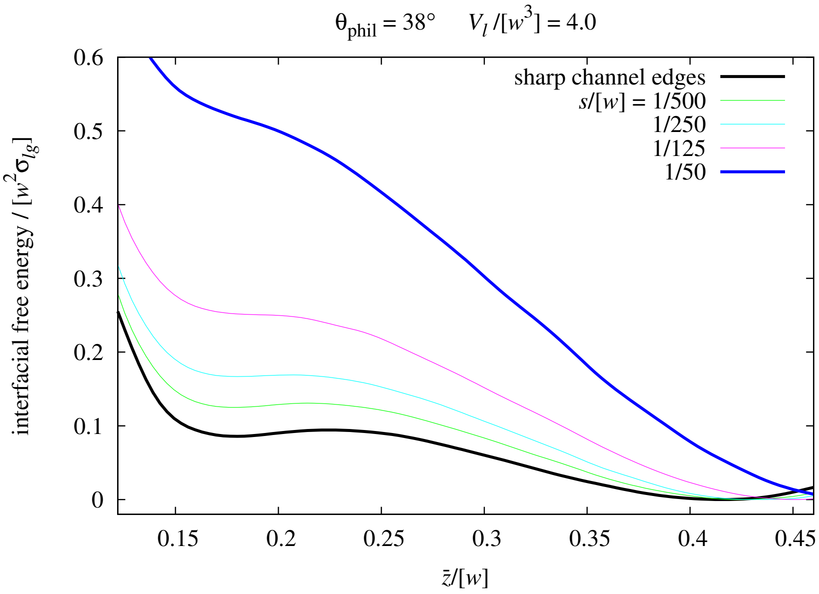

Figure 4.6: Destabilization of an initially metastable liquid ridge with a specific volume $V_l/[w^3] = 4.0$ on a chemical channel due to a certain relative smoothness $s/[w]$ of the channel edges. The smoothness parameter s is defined in (4.3).

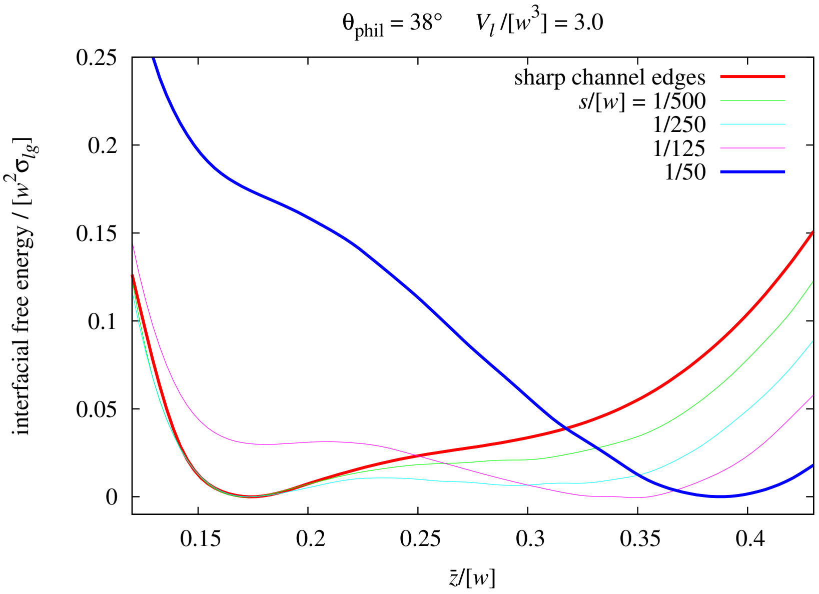

Figure 4.7: Destabilization of an initially stable liquid ridge with a specific volume $V_l/[w^3] = 3.0$ on a chemical channel due to a certain relative smoothness $s/[w]$ of the channel edges. The smoothness parameter s is defined in (4.3).

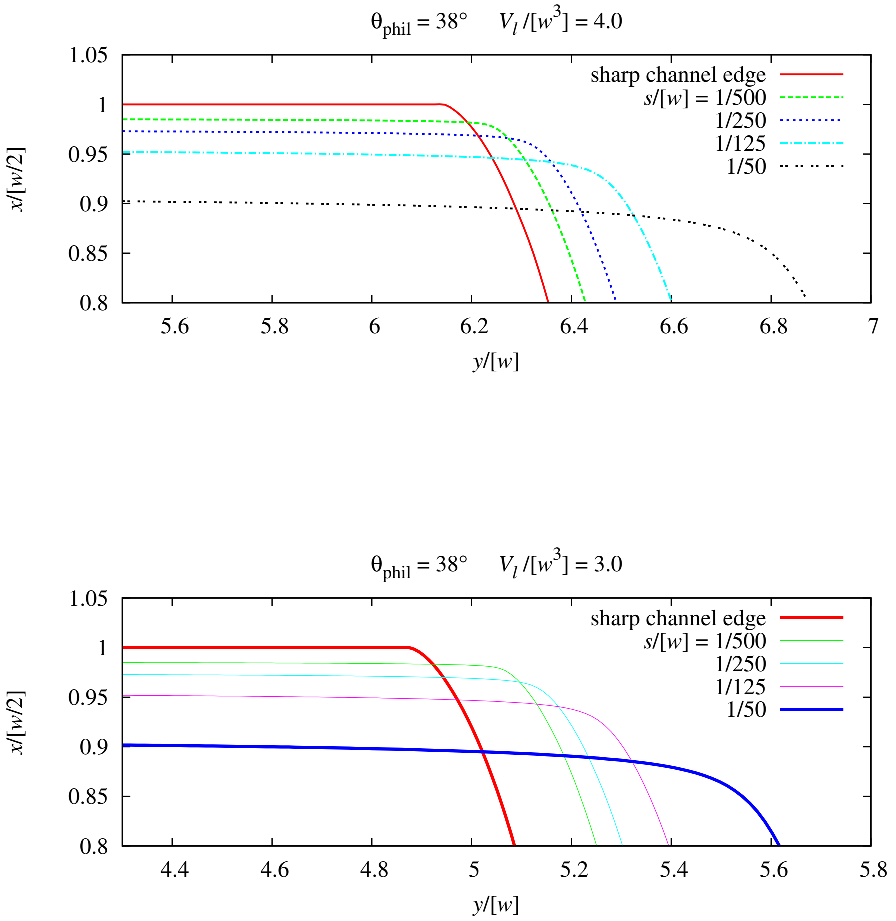

Figure 4.8: Three-phase contact lines at the tongue of a liquid ridge on a chemical channel for different values of the relative smoothness $s/[w]$. The ordinate is the lateral direction perpendicular to the channel and the channel edge is at $w/2$. The plots for the specific volumina $V_l/[w^3] = 3.0$ and $V_l/[w^3] = 4.0$ correspond to the plots of the interfacial free energy $\tilde{F}(\bar{z})$ in the figures 4.6 and 4.7, respectively. For sharp channel edges, the three-phase contact line is pinned at the edge at $x = w/2$, which gives rise to a minimum of the interfacial free energy $\tilde{F}$. In the case of smooth channel edges given by profiles $\mathbf{t}_s(x)$ (4.3), the three-phase contact line depins.

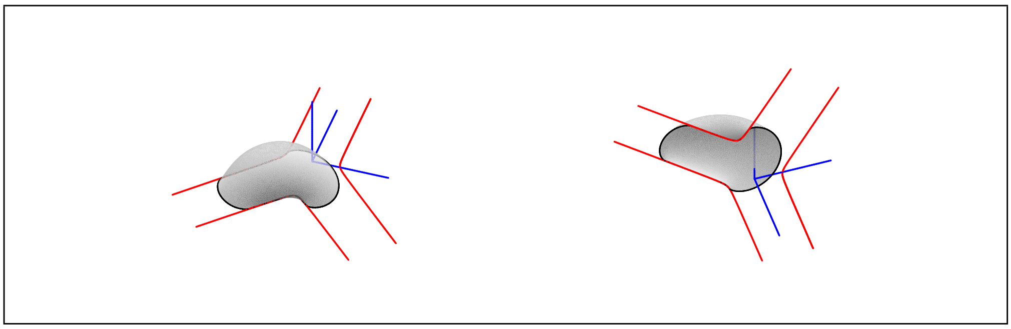

Figure 4.9: Top and bottom view of a droplet sitting on a chemical junction. The geometry of the junction is given in figure 4.2 and the blue lines denote the coordinate axes. The center of mass components $\bar{x}$ and $\bar{y}$ have been fixed during the minimization of $\tilde{F}$ in order to keep the droplet at a fixed position. The lyophilic contact angle and the specific liquid volume are $\theta_{\text{phil}} = 60°$ and $V_l/[w^3] = 1.2$, respectively.

Droplets on branched chemical channels

A consequence of the morphologic transition on straight chemical channel described above is, that an energetically stable bulge-like morphology may be transformed into the metastable ridge if the fluid passes an intersection of channels. This is shown in the following for the case of the y-junction depicted in figure 4.2.

Apart from spilling, a droplet sitting on a straight channel can spread only along the channel axis, while lateral spreading is facilitated for a droplet sitting in the junction area. Hence, there is a reduced specific volume in the junction area compared to the value $V_l/[w^3]$ out on the channels. This kind of inhomogeneity transforms into a global minimum of the free energy landscape the droplet is subject to, since a droplet sitting in the junction area is enabled to approximate a spherical shape a little bit better than a droplet sitting on a channel.

The free energy landscape for a droplet on the y-junction may be obtained via the minimization of the interfacial free energy under a constraint on the center of mass of the fluid in such a way, that the center of mass components in the xy-plane, $\bar{x}$ and $\bar{y}$, are fixed while $\bar{z}$ remains unconstrained. Effectively, this corresponds to a two-component, homogeneous body force which keeps the droplet at a certain lateral position on the junction while it is taking a shape of minimal interfacial free energy. The free energy landscape $\tilde{F}(x, y)$ then is scanned by minimizing $\tilde{F}$ (1.23) for given parameters θ_{phil} and $V_l/[w^3]$ while moving the center of mass around in the xy-plane.

The figures 4.10 and 4.11 show the free energy landscape and the corresponding contour plot of the y-junction, respectively, and the figure 4.9 shows a top and bottom view of the probing droplet as it expands into the channel region. The chemical steps defining the junction, indicated by the thick red lines, are sharp, the lyophilic contact angle is $\theta_{\text{phil}} = 60°$, and the specific fluid volume is $V_l/[w^3] = 1.2$.

The energetic minimum clearly shows up at the center of the junction. For a given value of $V_l/[w^3]$ and a decreasing contact angle contrast, the energy landscape evidently flattens. This is shown in figure 4.12 via cuts of $\tilde{F}(\bar{x}, \bar{y})$ for different lyophilic contact angles θ_{phil}. The cuts along $\bar{x}$ show an overshoot at the channel edges. This overshoot occurs due to the pinning of the three-phase contact line at the channel edges if the center of mass components $\bar{x}$ and $\bar{y}$ are fixed in the lyophobic vicinity of the channel edge. If they are fixed sufficiently far away from the channel edges, the three-phase contact line is forced to depin and the energy landscape is flat.

The figures 4.13 and 4.14 depict the scenario when an initially stable droplet, characterized by $V/[w^3] = 4.0$ and $\theta_{\text{phil}} = 38°$, passes the y-junction. Therefore, the droplet sitting on the ingoing channel has been guided through the junction onto one of the outgoing branches such, that the center of mass projection on the substrate follows the bottom of the energetic valley of the free energy landscape.

The interfacial free energy $\tilde{F}$ has been minimized for successively fixed values of $\bar{y}$ while $\bar{x}$ was left unconstrained, i.e., $\bar{y}$ defines the position on the junction and $\bar{x}$ is adjusted self-consistently during the minimization process. Via an additional constraint on the center of mass height $\bar{z}$ the energetic behaviour of the liquid has been unfolded analog to the plots in figure 4.4.

The graph for $\bar{y}/[w] = 10.0$ in the upper part of figure 4.13 is congruent with the graph for $V/[w^3] = 4.0$ in figure 4.4. Hence, the droplet in this case is too far away from the junction to be aware of the energetic minimum. Upon approaching the junction, i.e., for $\bar{y}/[w] \to 2.0$, ridge-like configurations are energetically stabilized and bulges are destabilized. This is due to the fact that a certain amount of fluid in the ridge is sucked into the energetic minimum at the center of the junction, while the bulge is not influenced significantly. Evidently, the liquid takes a state of lowest interfacial free energy possible if it is sucked completely into the junction.

The process when a liquid bulge initially sitting at $\bar{y} = 0.0$ is pulled onto one of the outgoing branches, i.e., $\bar{y} \rightarrow -10.0$, is depicted in the lower part of figure 4.13. In this case the effect of the energetic minimum is to retain some liquid in the junction while the rest is pulled out, hence, only meta-stable bulges are possible in the vicinity of the junction. Figure 4.14 shows stable and metastable liquid morphologies at different positions $\bar{y}/[w]$ on the junction corresponding to global and local energetic minima in figure 4.13, respectively.

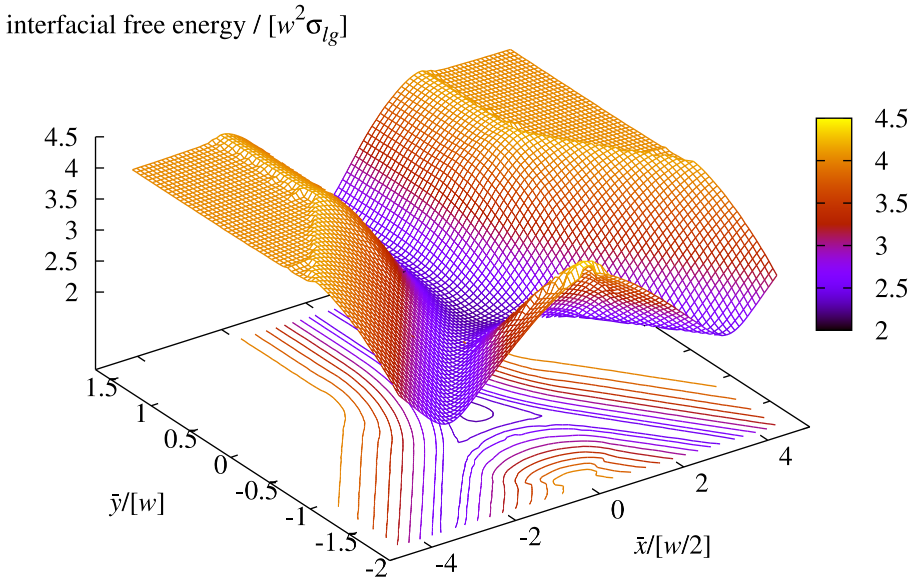

Figure 4.10: Free energy landscape given by $\tilde{F}$ versus $\bar{x}/[w/2]$ and $\bar{y}/[w]$ for the droplet shown in figure 4.9.

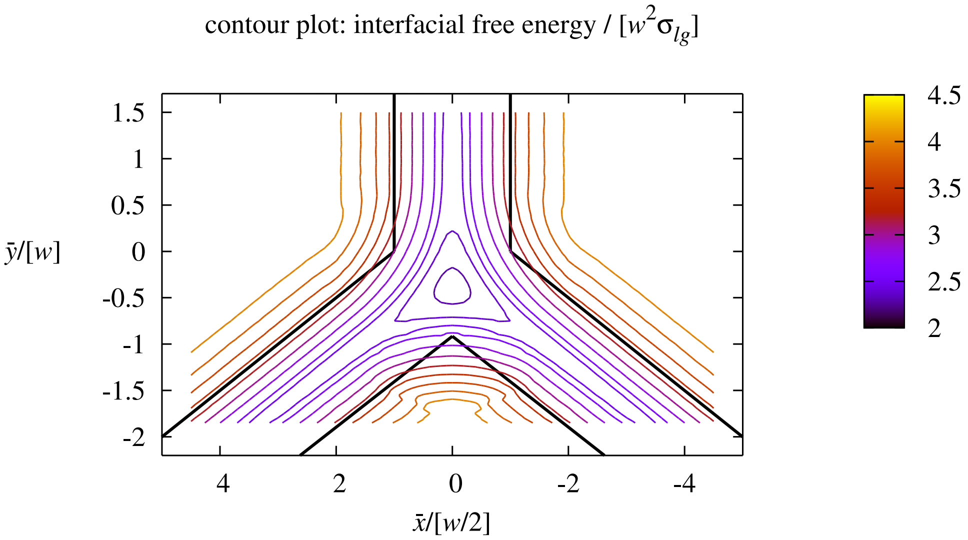

Figure 4.11: Contour plot corresponding to the free energy landscape in figure 4.10.

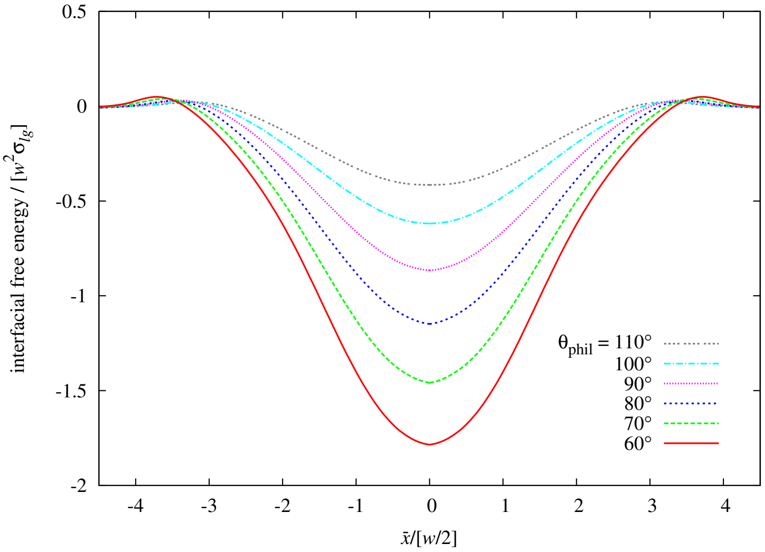
0.5
0
-0.5
-1
-1.5
-2
-4
-3
-2
-1
0
1
2
3
4
interfacial free energy / [w²σ_lg]
x̄/[w/2]
θ_phil = 110°
100°
90°
80°
70°
60°

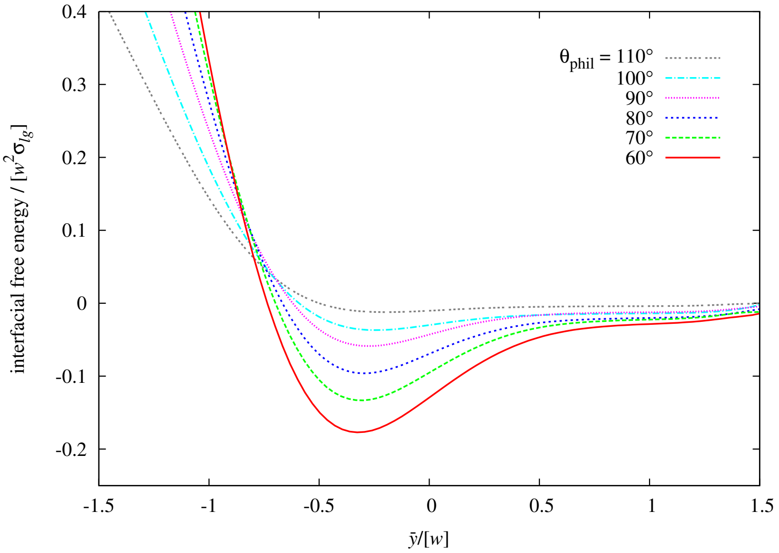
0.4
0.3
0.2
0.1
0
-0.1
-0.2
-1.5
-1
-0.5
0
0.5
1
1.5
interfacial free energy / [w²σ_lg]
ȳ/[w]
θ_phil = 110°
100°
90°
80°
70°
60°

Figure 4.12: Cuts of free energy landscapes along $\bar{x}$ through the global minimum and along $\bar{y}$ at $\bar{x} \equiv 0$. The cuts are taken for a decreasing maximum contact angle contrast, i.e., for different values of θ_{phil} and $\theta_{\text{phob}} \equiv 180°$. The cuts along $\bar{y}$ are shifted such, that they are at the level zero at high values $\bar{y}$.

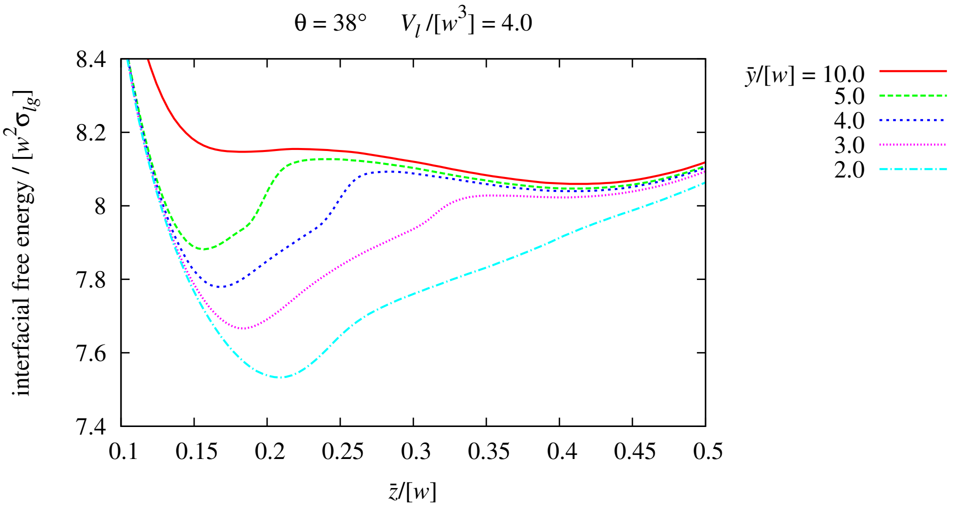
θ = 38° $V_l/[w^3] = 4.0$
interfacial free energy / $[w^2\sigma_{lg}]$
8.4
8.2
8
7.8
7.6
7.4
0.1
0.15
0.2
0.25
0.3
0.35
0.4
0.45
0.5
$\bar{z}/[w]$
$\bar{y}/[w]$ = 10.0
5.0
4.0
3.0
2.0

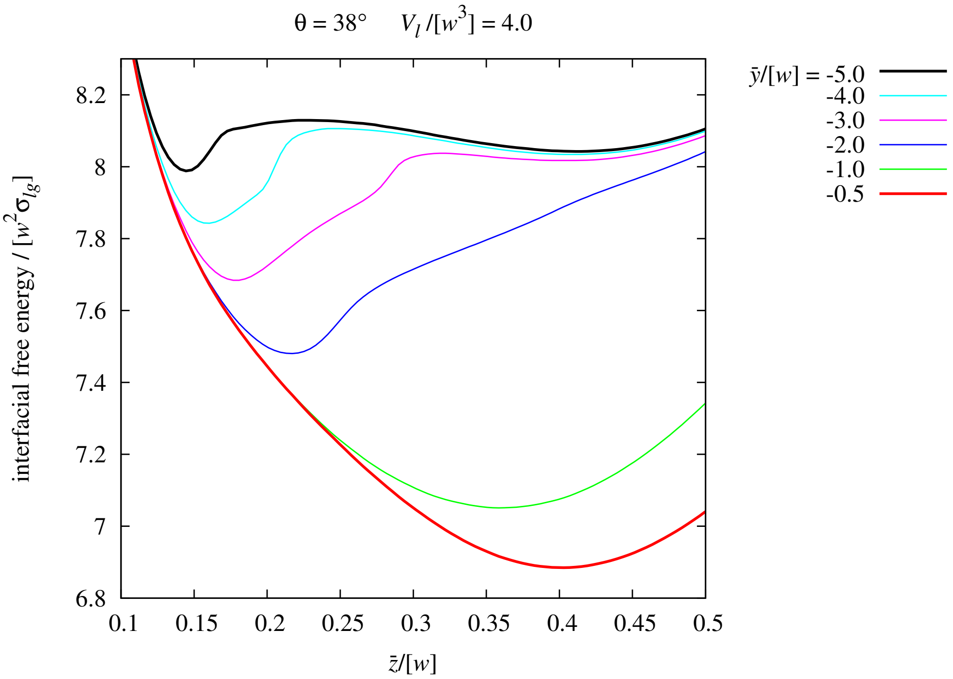
θ = 38° $V_l/[w^3] = 4.0$
interfacial free energy / $[w^2\sigma_{lg}]$
8.2
8
7.8
7.6
7.4
7.2
7
6.8
0.1
0.15
0.2
0.25
0.3
0.35
0.4
0.45
0.5
$\bar{z}/[w]$
$\bar{y}/[w]$ = -5.0
-4.0
-3.0
-2.0
-1.0
-0.5

Figure 4.13: Quasi-stationary picture of a liquid droplet driven into and out of a chemical junction. The geometry of the junction is given by figure 4.2. The interfacial free energy $\tilde{F}$ is plotted versus $\bar{z}$ for $\theta_{\mathrm{phil}} = 38°$, $V_l/[w^3] = 4.0$, and different positions $\bar{y}$ of the droplet.

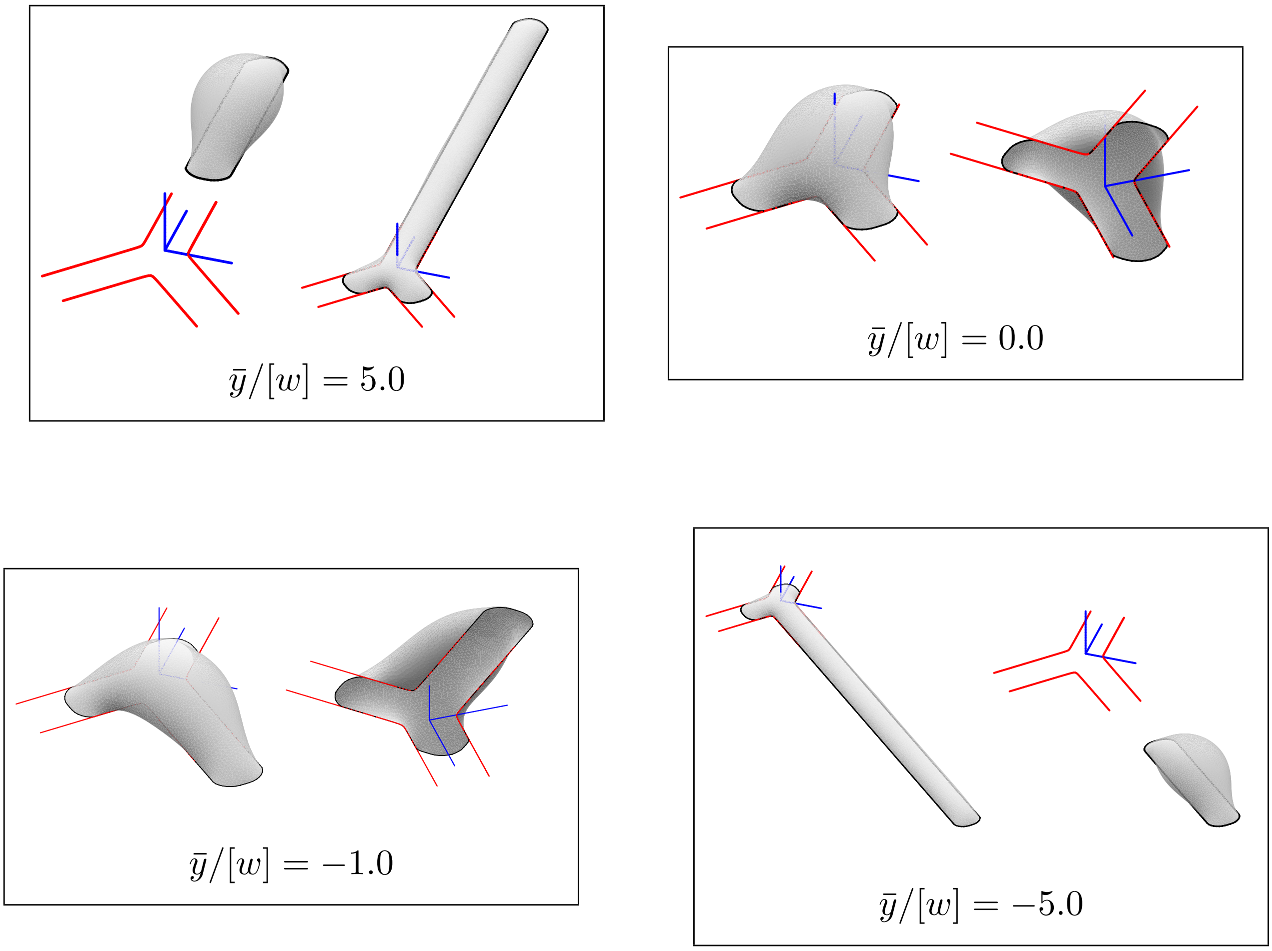

$\bar{y}/[w] = 5.0$

$\bar{y}/[w] = 0.0$

$\bar{y}/[w] = -1.0$

$\bar{y}/[w] = -5.0$

Figure 4.14: Stabilized ridge morphologies and metastable bulge morphologies on the junction at different positions $\bar{y}/[w]$.

4.2 Dynamics on chemical channels

Within this section, lattice Boltzmann simulations on the time evolution of fluid morphologies on chemical channels are presented. The numerical algorithm used for the simulations is version 5.0 of the LB3D-algorithm [83, 87, 95, 96], a three-dimensional, parallel implementation of the Shan-Chen model. The simulations have been performed on a system of two immiscible fluids in contact with a solid substrate. The fluid system corresponds to, e.g., a droplet of oil surrounded by water.

According to (3.16), the immiscibility between oil and water (indices “o” and “w”) is modeled by an interaction defined on neighbouring lattice sites $\mathbf{r}$ and $\mathbf{r} + \mathbf{c}_\alpha \Delta t$,

$$\mathbf{F}^{(\mathrm{o})}_{\mathrm{int}}(\mathbf{r},t) \;=\; -\xi^{(\mathrm{o})}_{|(\mathbf{r},t)} \sum_\alpha \mathcal{G}_{\mathrm{ow}}\, \xi^{(\mathrm{w})}_{|(\mathbf{r}+\mathbf{c}_\alpha\Delta t,t)} \mathbf{c}_\alpha \Delta t \quad , \tag{4.5}$$

with effective densities $\xi^{(\mathrm{o})}$ and $\xi^{(\mathrm{w})}$ depending on the actual oil and water densities $\varrho^{(\mathrm{o})}$ and $\varrho^{(\mathrm{w})}$, respectively, according to (3.25),

$$\xi^{(\mathrm{o,w})} \;=\; 1 - \exp[\varrho^{(\mathrm{o,w})}] \quad . \tag{4.6}$$

A positive value of the oil-water coupling constant $\mathcal{G}_{\mathrm{ow}}$ leads to a repulsion between oil and water particles. Particles of the same type are supposed to interact via elastic collisions only. Hence, there are no oil-oil and water-water interaction terms in (4.5), i.e., $\mathcal{G}_{\mathrm{oo}} = \mathcal{G}_{\mathrm{ww}} \equiv 0.0$. Further, oil and water are characterized by equal values of the particle mass, the relaxation time, and, according to (3.21), the viscosity, i.e., $m_\mathrm{o} = m_\mathrm{w} \equiv m$, $\tau_\mathrm{o} = \tau_\mathrm{w} \equiv \tau$, and $\mu_\mathrm{o} = \mu_\mathrm{w} \equiv \mu$, respectively. The choice of parameters in the simulations was $\mathcal{G}_\mathrm{ow} = 0.2$, $m = 1.0$, and $\tau = 1.0$. The viscosity therefore is $\mu/[mc_T^2] = 1/6$ with the thermal velocity c_T related to the lattice constant a via (3.4), i.e., $a = \sqrt{3}\, c_T/\Delta t$.

Since one-component-two-phase systems modeled by lattice Boltzmann algorithms generally are characterized by quite diffuse interfaces prone to instabilities under drive like, e.g., the Kelvin-Helmholtz instability, the oil-water set-up described above has been chosen in order to guarantee a well-defined and stable fluid-fluid interface [101–104].

Figure 4.15 depicts a droplet of oil sitting on a chemical channel close to equilibrium[1]. The simulation box in figure 4.15 has a length of $600a$, a width of $200a$, and a height of $100a$, where a is the periodicity of the positional lattice. The chemical channel marked red has a width $w/[a] = 20$ and the specific volume of the droplet is $V_\mathrm{o}/[w^3] = 4.0$. The channel is defined by a sharp wettability contrast to the non-wetting vicinity, i.e, the wettability jumps between plateau values on the red and blue areas within one lattice unit a. The substrate is posed as the bottom of the simulation box, and the box is capped by a homogeneous solid plate with the same wettability as the non-wetting blue parts of the substrate.

Both, the substrate, and the top plate consist of a layer of oil particles which are pinned to their lattice sites, i.e., in collisions these layers act as solid walls unable to take neither momentum nor energy. No-slip boundary conditions at these layers are modeled via a particle bounce-back [89, 90], i.e, particles arriving at the substrate layers are sent back to the lattice point they came from instead of undergoing specular reflection. Periodic boundary conditions are applied at the lateral front ends of the box.

---

[1] The initial configuration and the relaxation process will be discussed later on.

The wettability of a layer of fixed oil particles imitating a solid substrate is specified via the density of the pinned oil $\varrho^{(o)}_{|\text{substrate}}$ within the oil-water interaction $\mathbf{F}^{(o)}_{\text{int}}$ (4.5), i.e., chemical patterns are given by a certain dependence of $\varrho^{(o)}_{|\text{substrate}}$ on lateral coordinates. There is no means of defining interfacial tensions in the Shan-Chen model, i.e, the macroscopic contact angle θ as a measure of wettability is not a direct simulation input parameter. Measured from separate simulations on a homogeneous substrate for a given oil-water coupling $\mathcal{G}_{\text{ow}}$, the contact angle θ has to be related to the initial set-up of the densities of fixed oil, mobile oil, and water, respectively.

The set-up of initial densities for the system in figure 4.15 has been chosen such, that the macroscopic contact angle in equilibrium on and beyond the channel is $\theta_{\text{phil}} \approx 38^\circ$ and $\theta_{\text{pob}} \approx 140^\circ$, respectively [105]. The oil droplet in figure 4.15 is displayed by a contour corresponding to half the value of the maximum density of mobile oil. Figure 4.16 shows vertical cuts of the droplet along and perpendicular to the symmetry axis of the channel and figure 4.17 shows lateral cuts of the droplet given by the first and second layer of lattice points above the substrate. The color code assigned to the lattice points refers to the local mass density of the oil. The top plate and the surrounding water are not shown in the figures. The droplet has a well defined interface of about three to four lattice points in thickness and a homogeneous density inside. In contrast to the pinning of the three-phase contact line to the channel edges observed in the free energy picture, see figure 4.8, there is a spillage onto the lyophobic part of the substrate. The snapshot of the droplet in figure 4.15 has been taken after 10^4 time-steps Δt. Since at this simulation time there has not been any appreciable changes in the density distribution with respect to the situation a several hundred Δt ago, the configuration is considered close to equilibrium.

Relaxation of droplets on chemical channels

It has been shown in the preceding sections, that for a specific volumes $V_l/[w^3] = 4.0$ and $V_l/[w^3] = 3.0$ liquid bulges and ridges, respectively, are energetically stable configurations on a sharp chemical channel with a macroscopic contact angle $\theta = 38°$, see figures 4.3 and 4.4. Accordingly, configurations like these should be given as the endpoint of a relaxation process governed by the Navier-Stokes equations, i.e., the underlying Boltzmann equation.

The droplet in figure 4.15 therefore corresponds to the stable bulge-like equilibrium morphology in figure 4.3. The relaxation process of the droplet is depicted on the left hand side of figure 4.18. The initial configuration is a sphere of oil with a density $\varrho_o = 0.7$, which touches the stripe. The relaxation happens very fast, due to the fact that the bulge-like equilibrium configuration is quite similar to the initial sphere. The initial set-up on the right hand side of figure 4.18 as well as the sequence of time-steps is the same as on the left. However, the specific volume is reduced to $V_o/[w^3] = 3.0$. The oil now approaches a ridge-like equilibrium configuration and the relaxation process is much slower. The scenario shown in figure 4.18 qualitatively confirms the bifurcation detected in the free energy picture underlying the figures 4.3 and 4.4.

Driven droplet dynamics on chemical channels

The figures 4.19 show body-force driven droplets with $V_o/[w^3] = 4.0$ on straight chemical channels. There is a homogeneous acceleration aligned with the channel axis acting on both, the oil and the water. Since the simulation box is capped, this leads to a non-linear Poiseuille-type flow profile. No-slip boundary conditions modeled by a particle bounce-back are applied at the substrate and the top plate, whereas the system is periodic with respect to the lateral, open ends of the box. On the left hand side, the acceleration has an absolute value $a/[mc_T\tau^{-1}] = 1.7 \cdot 10^{-6}$ and the time window of the simulation spans $10^5\ \Delta t$. The droplet moves along the channel without a considerable change of its morphology, i.e, the thermal velocity c_T characteristic for the relaxation process is much higher than the macroscopic velocity field due to the drive. On the right, the acceleration is increased, $a/[mc_T\tau^{-1}] = 1.4 \cdot 10^{-5}$, and the time window spans $4 \cdot 10^4\ \Delta t$. The morphologic behaviour of the moving droplet reminds of the Landau-Levich effect [97–100], i.e., the tailing contact line falls back behind the droplet and a thin film is formed on the channel. This is a purely hydrodynamic effect studied in detail for coating problems.

The figures 4.20 - 4.22 show the driven case on a branched channel system for $V_o/[w^3] = 4.0$. The acceleration is aligned along the axis of the straight channel with an absolute value $a/[mc_T\tau^{-1}] = 1.4 \cdot 10^{-5}$ and the time window spans $10^5\ \Delta t$. The patterning is asymmetric in the sense that one of the branches forming the ring is slightly broader. In the symmetric case, the liquid is either trapped at the junction or driven off the pattern onto the lyophobic area depending on the strength of the driving force. The free energy landscape of a y-junction shown in figure 4.10 has a global minimum, which acts as a trap for the liquid. The situation qualitatively is the same in the figures 4.20 - 4.22. In the lattice Boltzmann simulations, the droplet would be trapped for an acceleration $a/[mc_T\tau^{-1}] < 1.7 \cdot 10^{-6}$.

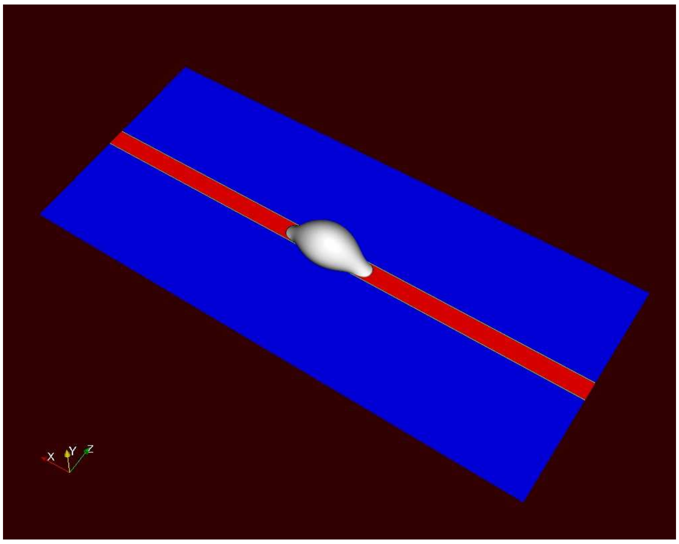

Figure 4.15: Lattice Boltzmann simulation of an oil droplet immersed in water (not shown) on a chemical channel close to equilibrium. The macroscopic contact angle on the channel is $\theta_{\rm phil} \approx 38^\circ$ and the specific volume of the oil droplet is $V_0/[w^3] = 4.0$.

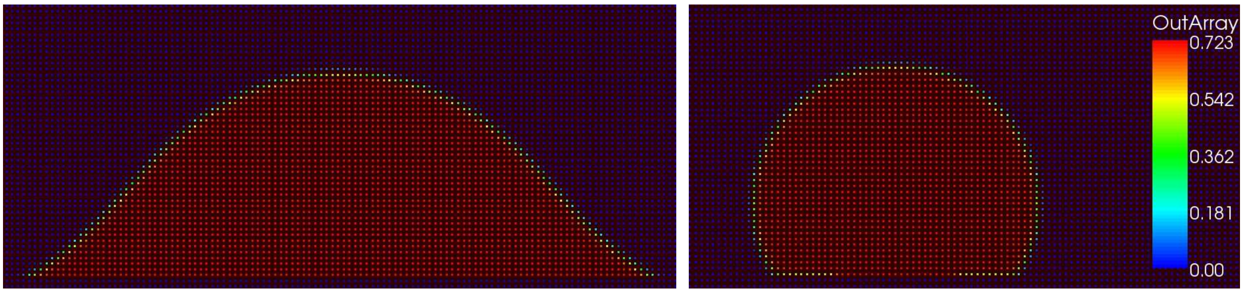

Figure 4.16: Vertical cuts of the droplet in figure 4.15 along and perpendicular to the symmetry axis of the channel. The color code assigned to the lattice points refers to the mass density of the oil. The substrate is not shown.

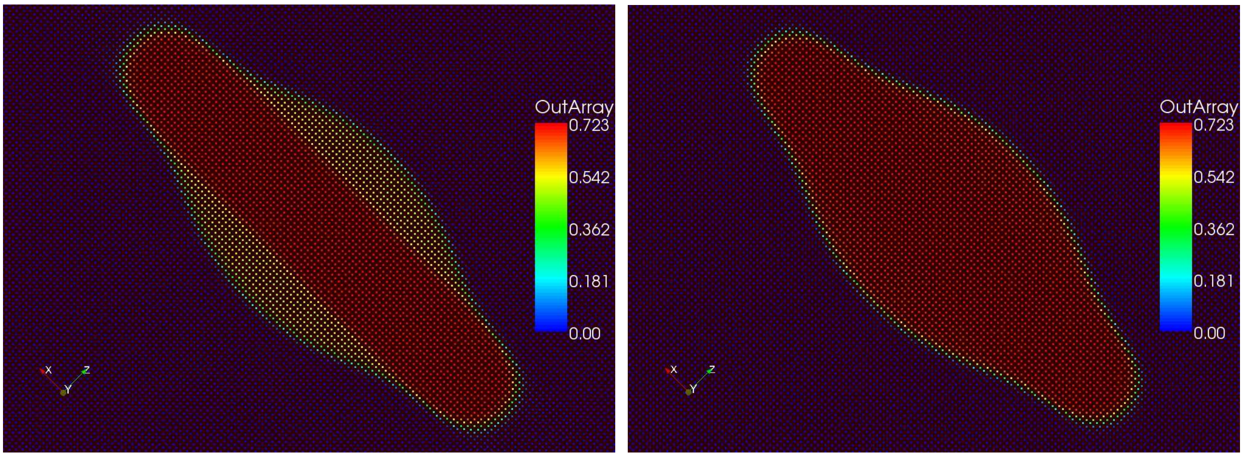

Figure 4.17: Lateral cuts of the droplet in figure 4.15 showing first (left) and second (right) layer of lattice points above the substrate. The color code assigned to the lattice points refers to the mass density of the oil.

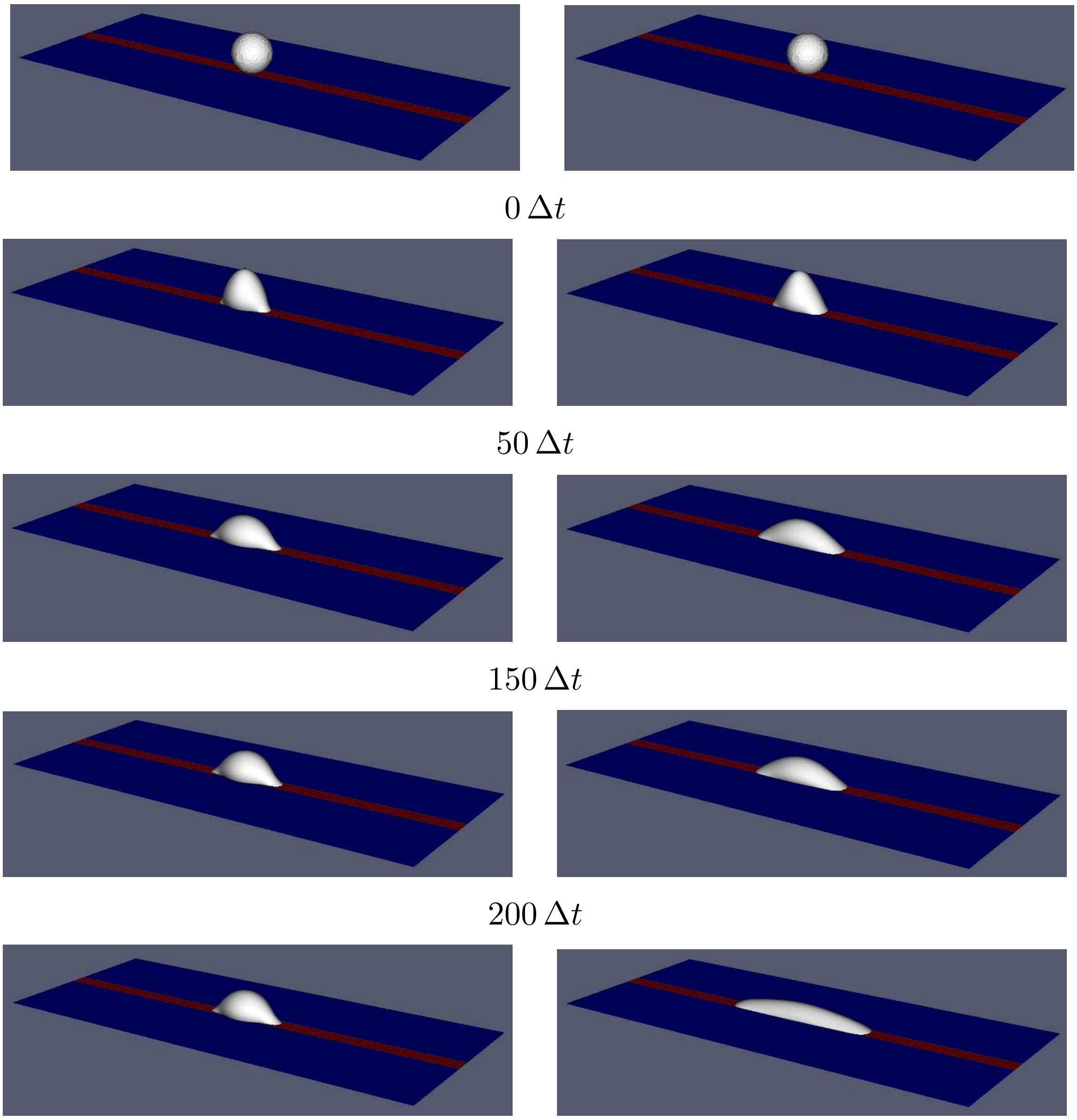

$0\,\Delta t$

$50\,\Delta t$

$150\,\Delta t$

$200\,\Delta t$

$5000\,\Delta t$

Figure 4.18: Relaxation process of a droplet of oil immersed in water on a chemical channel. The macroscopic contact angle on the channel is $\theta_{\text{phil}} \approx 38^\circ$ and the specific volume of the oil droplet is $V_0/[w^3] = 4.0$ (left hand side) and $V_0/[w^3] = 3.0$ (right hand side). In both cases, the sequence of time-steps Δt is the same.

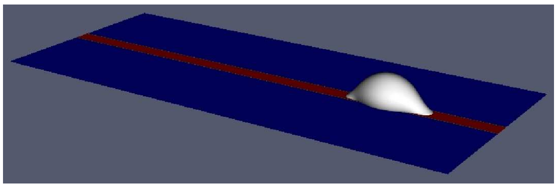

$2 \cdot 10^4\,\Delta t$

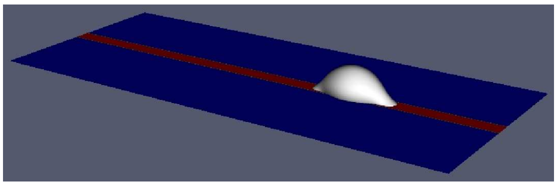

$4 \cdot 10^4\,\Delta t$

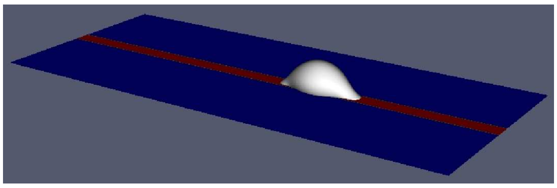

$6 \cdot 10^4\,\Delta t$

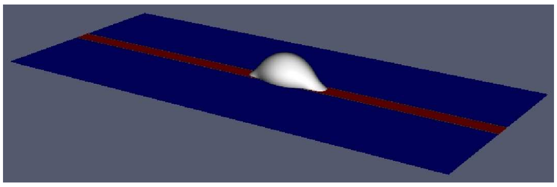

$8 \cdot 10^4\,\Delta t$

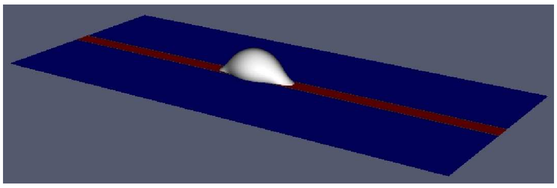

$10^5\,\Delta t$

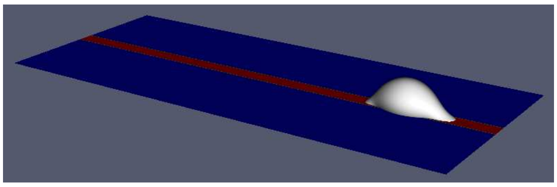

$2 \cdot 10^3\,\Delta t$

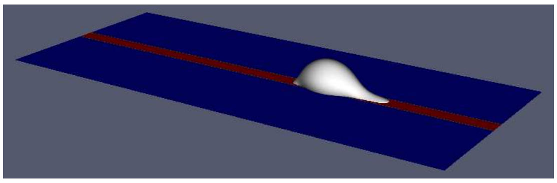

$10^4\,\Delta t$

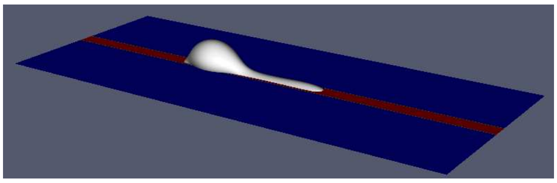

$2 \cdot 10^4\,\Delta t$

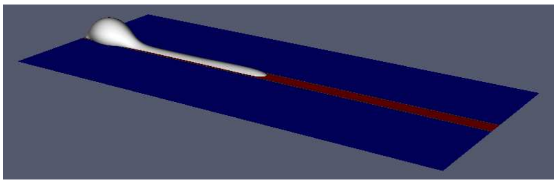

$3 \cdot 10^4\,\Delta t$

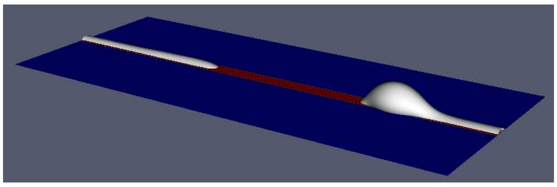

$4 \cdot 10^4\,\Delta t$

Figure 4.19: Droplet driven along a chemical channel for $V_l/[w^3] = 4.0$ and $\theta_{\text{phil}} \approx 38°$. The acceleration is aligned parallel to channel axis with an absolute value $a/[mc_T\tau^{-1}] = 1.7 \cdot 10^{-6}$ (left hand side) and $a/[mc_T\tau^{-1}] = 1.4 \cdot 10^{-5}$ (right hand side).

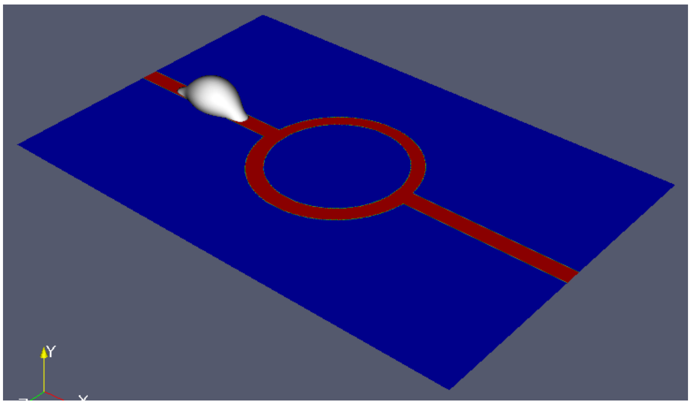

$2 \cdot 10^3\ \Delta t$

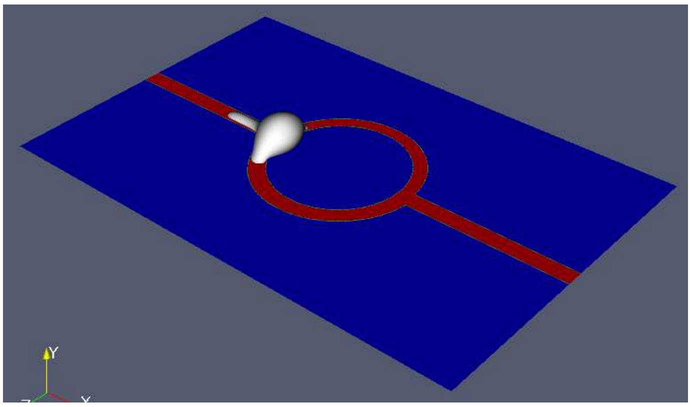

$10^4\ \Delta t$

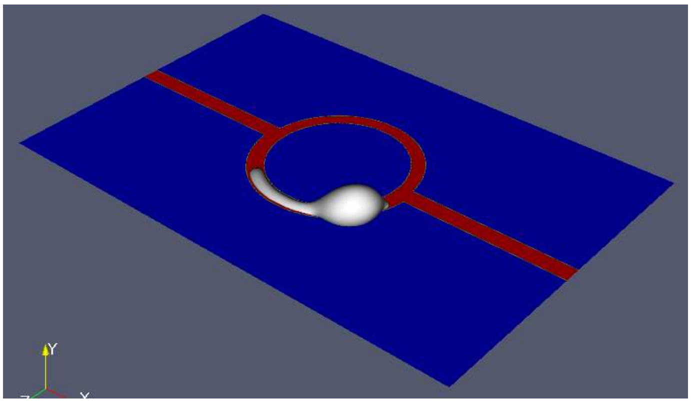

$3 \cdot 10^4\ \Delta t$

Figure 4.20: Droplet driven along a branched channel system for $V_l/[w^3] = 4.0$ and $\theta_{\mathrm{phil}} \approx 38°$. The acceleration is aligned parallel to the axis of the straight channel with an absolute value $a/[mc_T\tau^{-1}] = 1.7 \cdot 10^{-5}$.

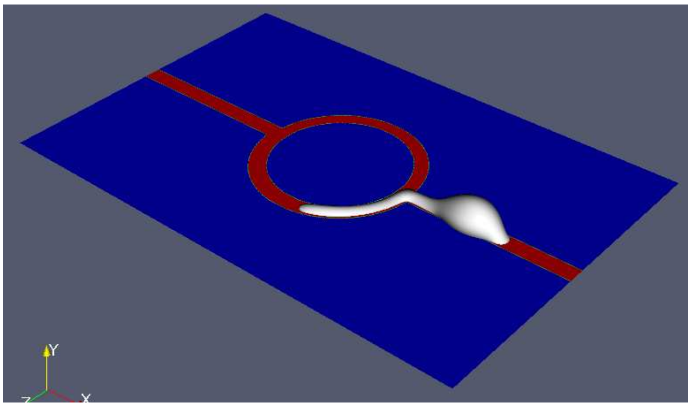

$4 \cdot 10^4 \, \Delta t$

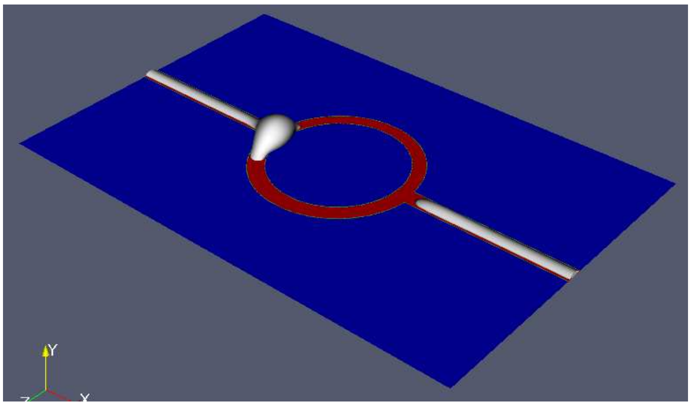

$6 \cdot 10^4 \, \Delta t$

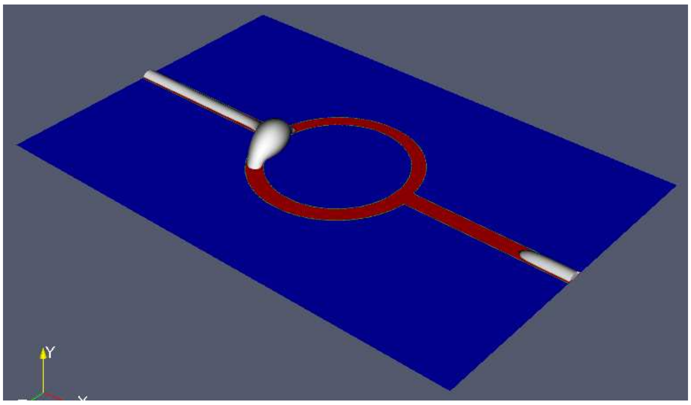

$7.5 \cdot 10^4 \, \Delta t$

Figure 4.21: Droplet driven along a branched channel system for $V_l/[w^3] = 4.0$ and $\theta_{\text{phil}} \approx 38^\circ$. The acceleration is aligned parallel to the axis of the straight channel with an absolute value $a/[mc_T\tau^{-1}] = 1.7 \cdot 10^{-5}$.

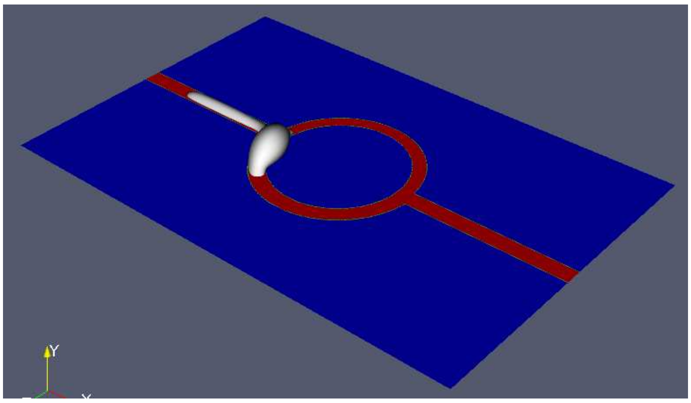

$9 \cdot 10^4 \, \Delta t$

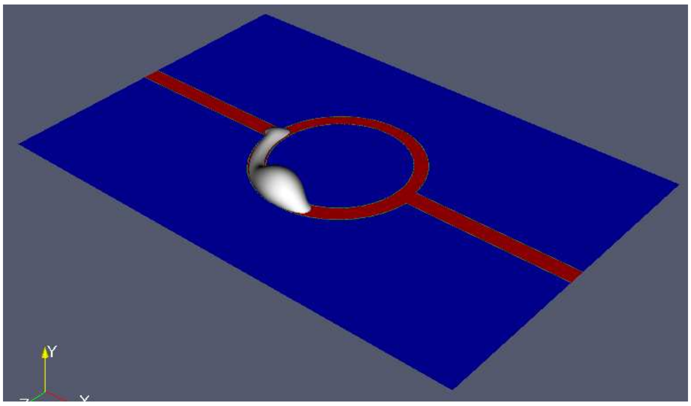

$10.5 \cdot 10^4 \, \Delta t$

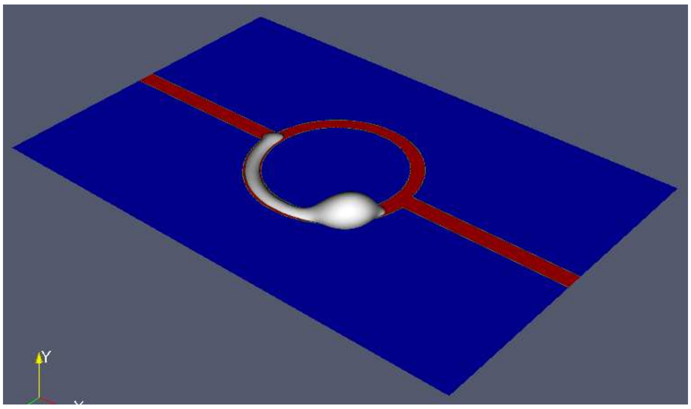

$11 \cdot 10^4 \, \Delta t$

Figure 4.22: Droplet driven along a branched channel system for $V_l/[w^3] = 4.0$ and $\theta_{\mathrm{phil}} \approx 38°$. The acceleration is aligned parallel to the axis of the straight channel with an absolute value $a/[mc_T\tau^{-1}] = 1.7 \cdot 10^{-5}$.

Chapter 5

Mesoscopic Fluid Properties

The matter of interest in the following is the energetic stability of mesoscopically thin wetting films and the formation of mesoscopic fluid droplets. The investigation is based on the effective free energy $\mathcal{F}$ (1.13) introduced in section 1.2 with a generic form of the effective interface potential $\phi(h)$.

Briefly reviewed, the effective interface potential $\phi(h)$ (1.12b) captures the net effect of long-ranged fluid-fluid and fluid-substrate interactions as a function of the fluid-fluid interfacial height h. The local not-overhanging interfacial height profile $h(\mathbf{R}_{\|})$ parameterized by lateral coordinates $\mathbf{R}_{\|}$ on a planar solid

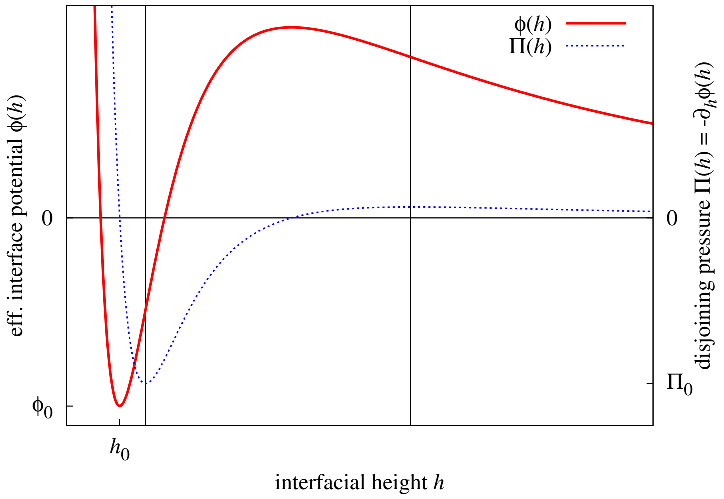

Figure 5.1: Generic form of the effective interface potential $\phi(h)$ and the disjoining pressure $\Pi(h) := -\partial_h \phi(h)$ as a function of the interfacial height h for a partially wetting substrate.

---

substrate is subject to the Euler-Lagrange equation (1.14),

$$\Delta p + \Pi(h) + \sigma_{lg} \nabla_{\|}^2 h \overset{!}{=} 0 \quad . \tag{5.1}$$

Solving equation (5.1) is equivalent to an extremization of the effective free

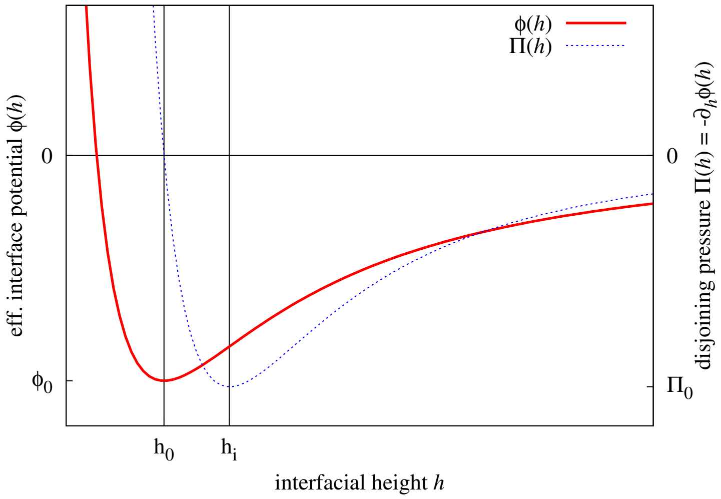

Figure 5.2: Effective interface potential $\phi(h)$, and disjoining pressure $\Pi(h) = -\partial_h\phi(h)$ as a function of the interfacial height h according to the model (5.4).

---

energy $\mathcal{F}$ (1.13),

$$\mathcal{F} \;=\; \underbrace{\int_{A_s} d^2R_{\|} \left\{ \sigma_{lg}\sqrt{1+|\nabla_{\|}h|^2} \;+\; \phi\left(h(\mathbf{R}_{\|})\right) \right\}}_{=:\tilde{\mathcal{F}}} \;-\; \Delta p \int_{A_s} d^2R_{\|}\;\, h(\mathbf{R}_{\|}) \quad , \tag{5.2}$$

with respect to the local interfacial height profile $h(\mathbf{R}_{\|})$, i.e., profiles which correspond to global or local minima of $\mathcal{F}$ are energetically stable or metastable equilibrium configurations, respectively, and profiles which correspond to maxima of $\mathcal{F}$ are energetically unstable equilibrium configurations.

In (5.1) and (5.2) Δp is the Laplace pressure, $\Pi(h)$ is the disjoining pressure, σ_{lg} is the liquid-gas interfacial tension, $\nabla_{||}$ is the two-dimensional gradient with respect to the lateral coordinates, A_s is the solid-liquid interfacial area, and $\tilde{\mathcal{F}}$ is the effective interfacial free energy.

For the case that the underlying molecular interactions are of Lennard-Jones type, the effective interface potential $\phi(h)$ has the algebraic form (1.16),

$$\phi(h) \; = \; \sum_{j \geq 2} a_j \, h^{-j} \quad . \tag{5.3}$$

The energetic stability of wetting films with a certain height h stems from the analytical properties of $\phi(h)$. The endpoint of a dewetting process driven by $\phi(h)$, i.e., the collapse of energetically unstable or metastable films into a set of droplets, is referred to as partial wetting. In case of unstable films, dewetting happens spontaneously and one speaks of spinodal dewetting whereas in case of metastable films the dewetting process has to be induced by the nucleation of holes. In section 1.2, dewetting has been discussed by means of the generic potential form displayed in figure 5.1. The finite equilibrium film height h_0 at which the effective interface potential $\phi(h)$ takes its global minimum ϕ_0, and hence, the disjoining pressure $\Pi(h) := -\partial_h \phi(h)$ vanishes, defines the characteristic mesoscopic scale. Unstable film prone to spinodal dewetting occur in the height regime between the two inflection points of $\phi(h)$ where $\partial_h^2 \phi(h) < 0$, and hence, $\Pi(h)$ increases for increasing local interfacial heights h.

The thickness of the wetting films investigated in the following lies in the range between h_0 and the height h_i of the subsequent inflection point. A suitable generic potential form therefore is

$$\phi(h) \overset{!}{=} \eta \left(\frac{1}{8\,h^8} - \frac{1}{2\,h^2} \right) \quad , \tag{5.4}$$

with an adjustable global minimum $\phi_0 = -3/8\eta$ at $h_0 = 1$, see figure 5.2.

The potential form (5.4) induces spinodal dewetting for any wetting film with a height above the level h_i, on the other hand, the level h_0 corresponds to a stable equilibrium wetting film at phase coexistence, i.e,

$$\Delta p = -\Pi_{|h_0} \equiv 0 \quad . \tag{5.5}$$

Accordingly, in the range of film heights between h_0 and h_i a morphologic transition takes place between a mesoscopically thin film and a set of mesoscopic droplets, which means that initially stable wetting films become metastable and finally unstable upon approaching the height h_i, while simultaneously an initially unstable configuration of mesoscopic droplets becomes stable.

The morphologic transition corresponds to a bifurcation with respect to the extremization of the effective interfacial free energy $\tilde{\mathcal{F}}$ (5.2), i.e, along a certain path in the parameter space spanned by V_l, A_s, and the relative potential depth $|\phi_0/\sigma_{lg}|$, there exist several solution branches of the Euler-Lagrange equation (5.1). One of these branches corresponds to wetting films with a certain height $h_f = V_l/A_s$ determined by the balance of a non-zero Laplace pressure and the disjoining pressure,

$$\Delta p \equiv -\Pi_{|h_f} \quad . \tag{5.6}$$

The other branches correspond to configurations of mesoscopic droplets with local interfacial height profiles $h(\mathbf{R}_{\|})$ determined by a non-trivial local balance of a non-zero Laplace pressure Δp, the disjoining pressure $\Pi(h)$, and the curvature term $\sigma_{lg}\nabla_{\|}^2 h$.

Within the following sections, the calculation of the height profile $h(\mathbf{R}_{\|})$ of mesoscopic droplets and the energetic deconvolution of the morphologic transition in the parameter space spanned by V_l, A_s, and $|\phi_0/\sigma_{lg}|$ is the matter of interest, based on the effective free energy $\mathcal{F}$ (5.2) with an effective interface potential $\phi(h)$ modeled by (5.4).

5.1 Mesoscopic droplet morphologies

As explained above, an extended wetting film with a height h_f within the range $h_0 < h_f < h_i$ might be stable or metastable with respect to the breakup into a set of droplets, where h_0 is the level of the global minimum ϕ_0 and h_i is the level of the inflection point of $\phi(h)$.

This means that a film sector covering a certain substrate area A_s with a certain interfacial height $h_f = V_l/A_s$, enclosing the volume V_l, might represent a local minimum of the interfacial free energy $\tilde{\mathcal{F}}$ (5.2), while for the same values of A_s and V_l a mesoscopic droplet given by a non-trivial local interfacial height profile $h(\mathbf{R}_{||})$ might represent a global minimum of $\tilde{\mathcal{F}}$, and vice versa.

The figure 5.3 shows the interfacial height profile of a mesoscopic droplet with a solid-liquid interfacial area $A_s/[\pi h_0^2] = 100^2$, a liquid volume $V_l/[A_s h_0] = 1.1273$, and a relative potential depth $|\phi_0/\sigma_{lg}| = 0.5$. The profile is given by a triangulated surface obtained via the numerical minimization of the effective free energy $\mathcal{F}$ (5.2) with the model potential (5.4) by means of the finite element algorithm described in section 1.3. Since the disjoining pressure $\Pi(h)$ strongly diverges at very small interfacial heights, see figure 5.2, the interfacial height profile $h(\mathbf{R}_{||})$ of the mesoscopic droplet is given by a cap smoothly evolving out of a surrounding film, i.e., the substrate never falls dry. The Laplace pressure Δp, which in the minimization of $\mathcal{F}$ plays the role of a Lagrange multiplier, in this case is a positive constant. The height $\tilde{h}$ of the surrounding film exceeds the equilibrium film height h_0 due to the fact that on flat interfacial domains a non-vanishing Laplace pressure has to be balanced by the disjoining pressure, i.e., $\Delta p = -\Pi_{|\tilde{h}}$.

Numerical minimization results for different ratios V_l/A_s indicate the morphologic transition between a wetting film and a mesoscopic droplet.

- ▷ For $V_l/A_s = h_0$, a wetting film is stable and a droplet does not exist as an equilibrium configuration.
- ▷ For increasing values $V_l/A_s \to h_i$, droplets become first metastable and finally stable with respect to flat wetting films.
- ▷ For $V_l/A_s > h_i$, flat wetting films are unstable, i.e., even the slightest bump in the triangulation causes a flat film to collapse into a droplet.

5.2 Analytical model

In order to unfold the morphologic transition energetically, the shape of the free energy barrier between stable and metastable interfacial profiles has to be calculated with respect to suitable parameters. Thereto, an approach is presented in the following, which allows for an analytic treatment of the effective free energy $\mathcal{F}$ (5.2).

Within this approach, see figure 5.4 for a schematic sketch, the interfacial height profile $h(\mathbf{R}_{||})$ of a mesoscopic droplet is associated with a model profile $\tilde{A}_{lg}$, which is given by a spherical cap intersecting the surrounding film with a height $\tilde{h} = h_0 + \Delta h$ at a certain angle α. The profile $\tilde{A}_{lg}$ covers the solid-fluid interfacial area A_s and the liquid volume V_l corresponds to the space enclosed

$V_{\text{ex}}/[A_s h_0]$	$\Delta h/[h_0]_{\text{anal.}}$	$\delta h/[h_0]_{\text{num.}}$	$\Delta p/[\sigma_{lg} h_0^{-1}]_{\text{anal.}}$	$\Delta p/[\sigma_{lg} h_0^{-1}]_{\text{num.}}$
0.05	0.02445	0.02501	0.16734	0.17110
0.1	0.01647	0.01583	0.11856	0.11442
0.5	0.01076	0.00836	0.08033	0.06221

$V_{\text{ex}}/[A_s h_0]$	$\tilde{\mathcal{F}}/[\phi_0 A_s]_{\text{anal.}}$	$\tilde{\mathcal{F}}/[\phi_0 A_s]_{\text{num.}}$
0.05	1.01580	1.01646
0.1	1.02928	1.03048
0.5	1.09557	1.09881

Table 5.1: Comparison of numerical results versus the analytical results corresponding to the profiles in figure 5.6.

---

by A_s and $\tilde{A}_{lg}$. With the equilibrium film height h_0 as the level of reference, the following parameters are specified:

- ▷ Δh denotes the excess height of the surrounding film.
- ▷ $V_{\text{ex}} := V_l - A_s h_0$ denotes the excess liquid volume.
- ▷ h_{cap} and V_{cap} denote the apex height and the volume of the cap, respectively.

By means of mechanical equilibrium arguments relying on $\phi_0 \approx \phi_{|(h_0=\Delta h)}$, the effective contact angle θ, at which the model profile $\tilde{A}_{lg}$ intersects the level h_0, can be related to the global minimum ϕ_0 of the effective interface potential,

$$\phi_0 \;=\; \sigma_{lg}\,(\cos\theta - 1) \quad . \tag{5.7}$$

The underlying idea of the approach is to associate the interfacial height profile $h(\mathbf{R}_{\|})$ of a mesoscopic droplet with a spherical cap, which is determined by the global minimum ϕ_0 of the effective interface potential and the liquid-gas interfacial tension σ_{lg}.

The angle α thereby is an integration parameter for the evaluation of the free energy $\mathcal{F}$ (5.2) on the profile $\tilde{A}_{lg}$, which for a given potential depth ϕ_0 is determined by the excess volume V_{ex} and the excess height Δh. This means, that for a given set (ϕ_0, V_{ex}) different sets $(V_{\text{cap}}, \Delta h)$, and thus, different model profiles $\tilde{A}_{lg}$ with different free energies $\mathcal{F}$ are possible. The set of possible profiles $\tilde{A}_{lg}$ for a given set (ϕ_0, V_{ex}) can be specified by means of the two limiting cases depicted in figure 5.5.

- ▷ The first limiting case for $\tilde{A}_{lg}$ is determined by $\Delta h = 0$. This means $V_{\text{cap}} \equiv V_{\text{ex}}$, i.e., the cap has a maximum apex height $h_{\text{cap}}^{(\text{max})}$. The profile $\tilde{A}_{lg}$ therefore consists of the spherical cap intersecting the surrounding film at the level h_0 under an angle $\alpha = \theta$. This case is depicted by the blue line in figure 5.5.
- ▷ The second limiting case for $\tilde{A}_{lg}$, depicted by the thick red line in figure 5.5, corresponds to a flat wetting film with a height $\Delta h_{\max} := V_{\text{ex}}/A_s$.

> The associated spherical cap in this case does not intersect but touches the film, i.e., the cap has has a minimum apex height $h_{\text{cap}}^{(\text{min})} \equiv \Delta h_{\text{max}}$ and a minimum volume $V_{\text{cap}}^{(\text{min})}$ while the angle α equals zero.

Accordingly, the model profiles $\tilde{A}_{lg}$ which for a given set (ϕ_0, V_{ex}) correspond to mesoscopic droplets are given by spherical caps with a volume V_{cap}, intersecting the surrounding film with an excess height Δh at an angle α, where

$$V_{\text{cap}}^{(\text{min})} < V_{\text{cap}} \leq V_{\text{ex}} \ , \qquad 0 \leq \Delta h < \Delta h_{\text{max}} \ , \qquad 0 < \alpha \leq \theta \quad .$$

The free energy $\mathcal{F}$ (5.2) now can be analyzed with respect to the parameter Δh as follows.

- ▷ For fixed values of V_{ex}, θ, and A_s, the parameters h_{cap} and Δh are calculated for a certain number of profiles $\tilde{A}_{lg}$.
- ▷ The interfacial free energy $\tilde{\mathcal{F}}$ integrated on those profiles $\tilde{A}_{lg}$ is plotted versus Δh.

The Figure 5.6 shows interfacial height profiles obtained by means of the analytical model compared to profiles obtained via numerical minimization by means of the finite element algorithm for different values of the excess volume V_{ex}. The numerical data points represent vertical cuts of triangulated surfaces, and the solid analytical curves are calculated by means of the parameter sets $(\Delta h, h_{\text{cap}})$ which correspond to minima of the interfacial free energy $\tilde{\mathcal{F}}$ for given values of A_s, V_{ex}, and θ. The numerical profiles are flattened due to the effective interface potential $\phi(h)$, which acts like an external field on the interfacial profile. A comparison of analytical and numerical values of the excess film height Δh, the Laplace pressure Δp, and the interfacial free energy $\tilde{\mathcal{F}}$ is given in table 5.1.

5.3 The morphologic transition of mesoscopic droplets

Based on the analytical approach introduced above, an investigation of the morphologic transition between a mesoscopic droplet and a flat wetting film in the parameter space spanned by the excess liquid volume V_{ex}, the solid-liquid interfacial area A_s, and the effective contact angle θ is presented in the following.

The figure 5.7 shows plots of the interfacial free energy $\tilde{\mathcal{F}}$ (5.2) as a function of the excess film height Δh for different values of V_{ex} and fixed values of A_s and θ. The excess film height Δh is scaled by its maximum value Δh_{max} and the interfacial free energy $\tilde{\mathcal{F}}$ is scaled by $(\phi_\Delta + \sigma_{lg})A_s$, where $\phi_\Delta := \phi_{|(h_0+\Delta h_{\text{max}})}$. Hence, the point $(1, 1)$ in which all plots coincide corresponds to flat wetting films with excess heights $\Delta h_{\text{max}} \in \{\, (V_{\text{ex}}/A_s) \,\}$, as given by the second limiting case of the analytical model, and the range $\Delta h/[\Delta h_{\text{max}}] < 1$ corresponds to mesoscopic droplets.

The plots for different values of the excess volume V_{ex} in figure 5.7 reveal a bifurcation leading to the morphologic transition: Below a certain threshold of V_{ex} a flat film is the only stable configuration. For increasing values of V_{ex}, first a local minimum, and then a global minimum develops for $\Delta h/[\Delta h_{\max}] < 1$, i.e, the mesoscopic droplet first becomes metastable while the flat film remains stable, then it becomes stable while the film becomes metastable, and finally, at high values of V_{ex}, the flat film becomes unstable. The insert in figure 5.7 depicts the same data in a different scaling and the graphs are shifted vertically such that the global minima have height zero.

The bifurcation revealed in figure 5.7 translates into a hysteresis of the Laplace pressure Δp with respect to the excess volume V_{ex}, as shown in figure 5.8. The graph consists of two branches. The lower one refers to mesoscopic droplets and the upper one refers to flat wetting films. Both branches have an endpoint at which the corresponding morphology becomes unstable. The red and blue squares correspond to stable and metastable configurations, respectively, i.e., local or global minima of $\tilde{\mathcal{F}}$ as shown in figure 5.7. The green squares correspond to unstable equilibria, i.e., local maxima of $\tilde{\mathcal{F}}$. The non-chained black squares are obtained via the numerical minimization of $\mathcal{F}$ with Δp as a Lagrange parameter. The value of the excess liquid volume $\tilde{V}_{\text{ex}}$ for which a morphology switches from stability to metastability is marked by a blue vertical line. In this case, the interfacial free energy $\tilde{\mathcal{F}}$ as a function of the excess height Δh has two equally deep minima.

The hysteresis may be described as follows. By increasing the liquid volume a flat film may be driven along the upper branch until at the endpoint it becomes unstable. Then, a jump happens to the lower branch, i.e., the film collapses and a mesoscopic droplet forms. By decreasing the liquid volume again, the system then can be driven on the lower branch until at the endpoint it jumps back again to the flat film morphology.

Figure 5.9 shows the morphologic transition with respect to the effective contact angle θ for a fixed ratio V_{ex}/A_s. There is a certain minimal value of θ, i.e., a certain threshold for the relative potential depth $|\phi_0/\sigma_{lg}|$, above which a mesoscopic droplet exists as a metastable configuration. For increasing values of θ an energy barrier successively grows in height, which means an increase of stability for both, mesoscopic droplets, and flat wetting films.

As already mentioned, the stability of the mesoscopic droplet is characterized by a local balance of Δp, $\Pi(h)$, and $\sigma_{lg}\nabla_{\|}^2$ on the interfacial profile $h(\mathbf{R}_{\|})$, while for the flat film with the height h_f the balance $\Delta p = \Pi_{|h_f}$ holds.

Accordingly, the morphologic transition is triggered by a competition between the disjoining pressure $\Pi(h) := -\partial_h\phi(h)$ and the interfacial tension σ_{lg}. For a given ratio V_l/A_s, this competition affects the effective interfacial free energy $\tilde{\mathcal{F}}$ (5.2) in such a way, that the displacement of the curved interfacial profile $h(\mathbf{R}_{\|})$ from the film level h_f generates an energetic gain due to the interfacial tension σ_{lg}, while an energetic loss might occur at the same time since extensive parts of the displaced interface come closer to the global minimum value ϕ_0 at the level h_0.

The figure 5.10 shows the impact on $\tilde{\mathcal{F}}$ due to a change of V_{ex} and A_s while the ratio $V_{\mathrm{ex}}/[A_s h_0]$ is kept constant. This corresponds to a flat wetting film which spreads or shrinks at constant height due to an injection or an extraction of liquid. The analysis of this scenario in terms of energetic loss due to ϕ and energetic gain due to σ_{lg} as a function of A_s is given in figure 5.11, i.e., the difference of loss and gain reveals whether the mesoscopic droplet may exist as a stable or a metastable configuration.

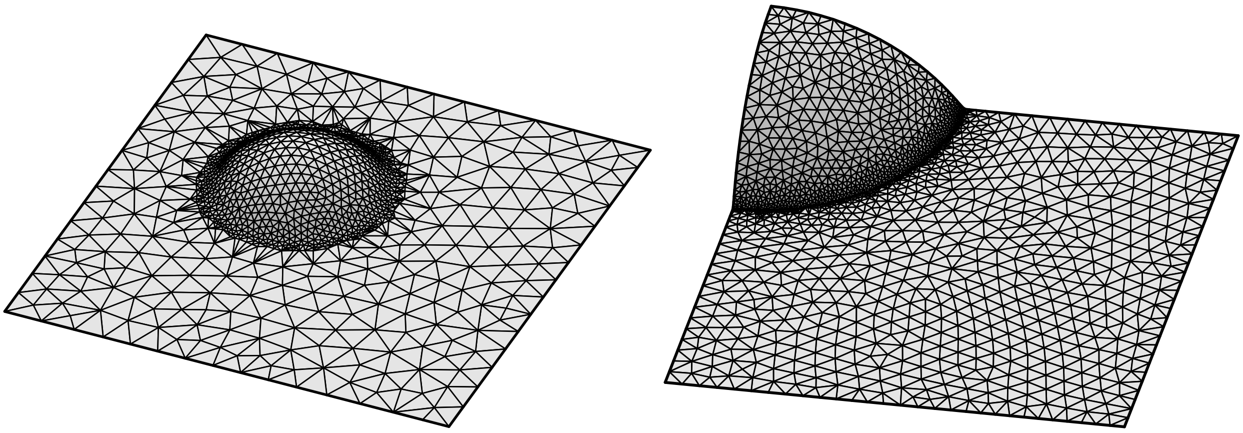

Figure 5.3: Mesoscopic droplet morphology obtained by numerical minimization of the effective interfacial free energy $\tilde{\mathcal{F}}$ (5.2) for an effective contact angle $\theta = 60^\circ$ corresponding to a relative potential depth $|\phi_0/\sigma_{lg}| = 0.5$. The substrate lying underneath is not shown. Due to rotational symmetry, it is possible to simulate a quarter of the satem in order to save computational resources. The refinement of the triangulation has been coupled to the need for spatial resolution in an adaptive way in order to keep the mesh size sufficiently small in the regions where the droplet evolves out of the film and bigger elsewhere.

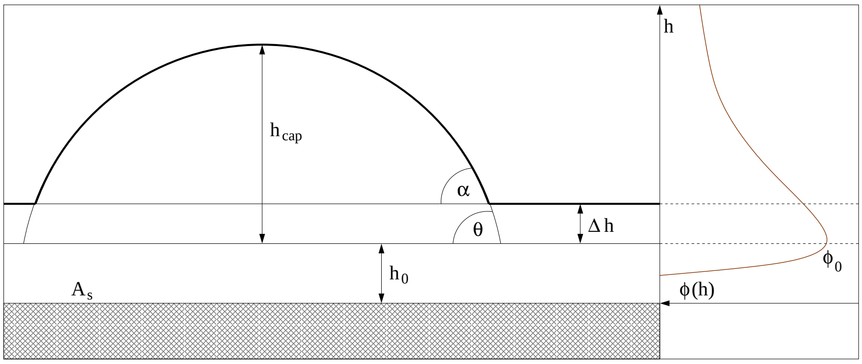

Figure 5.4: Schematic sketch of the analytical model. The thick black line represents the analytic interfacial model profile $\tilde{A}_{lg}$. The graph on right depicts the effective interface potential $\phi(h)$ with a minimum at the level h_0 as a function of the interfacial height h.

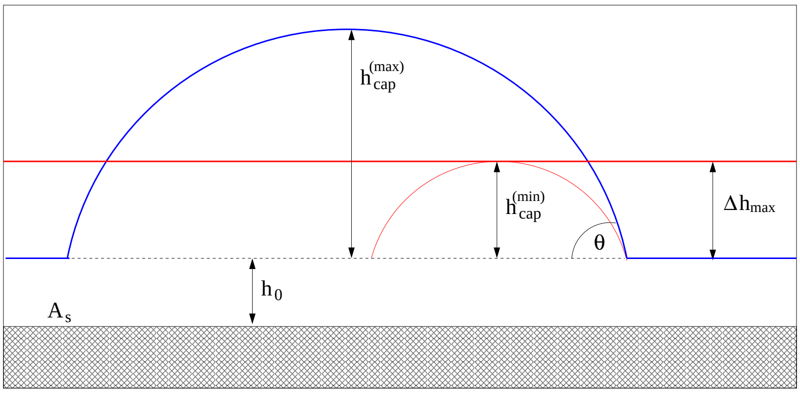

Figure 5.5: Schematic sketch of the border cases of the analytical model. The thick blue line depicts the first border case determined by $\Delta h = 0$ and $V_{\mathrm{cap}} \equiv V_{\mathrm{ex}}$. The red lines represent the second border case, i.e., the case in which the interfacial profile $\tilde{A}_{lg}$ is a flat film determined by $\Delta h_{\mathrm{max}} := V_{\mathrm{ex}}/A_s$ and $h_{\mathrm{cap}}^{(\mathrm{min})} \equiv \Delta h_{\mathrm{max}}$.

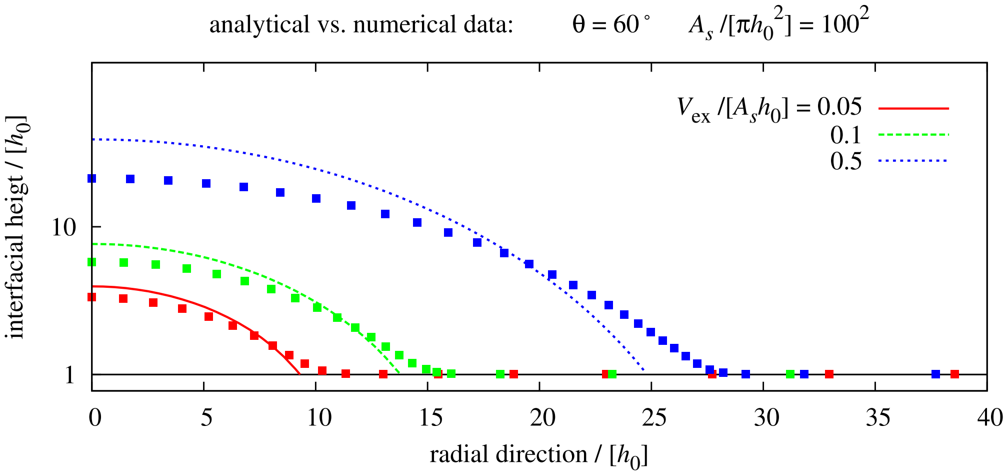

Figure 5.6: Height profiles obtained analytically (full lines) and via numerical minimization (squares) for different excess volumes V_{ex} and a fixed solid-liquid interfacial area A_s. The contact angle $\theta = 60°$ corresponds to the relative potential depth $|\phi_0/\sigma_{lg}| = 0.5$.

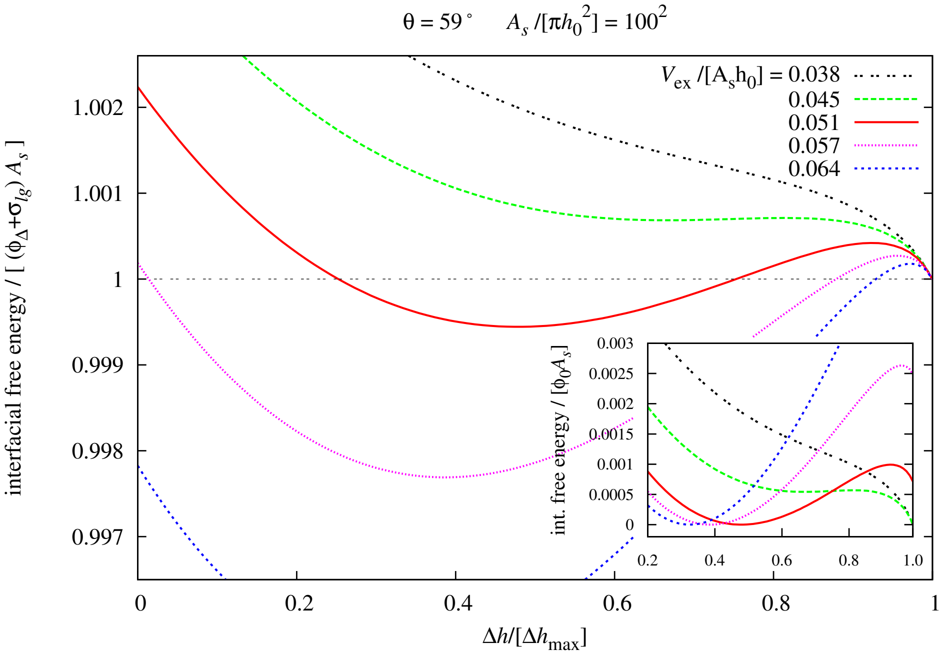

Figure 5.7: The morphologic transition with respect to the excess volume V_{ex} for fixed values of the effective contact angle θ and the solid-liquid interfacial area A_s. The effective interfacial free energy $\tilde{\mathcal{F}}$ is scaled by means of $\phi_\Delta := \phi_{|(h_0+\Delta h_{\mathrm{max}})}$, i.e., the point $(1,1)$ corresponds to uniform films with a height $h_f = h_0 + \Delta h_{\mathrm{max}}$. Insert: $\tilde{\mathcal{F}}$ is scaled by means of $\phi_0 := |\phi_{|h_0}|$ and the global minima are shifted to zero.

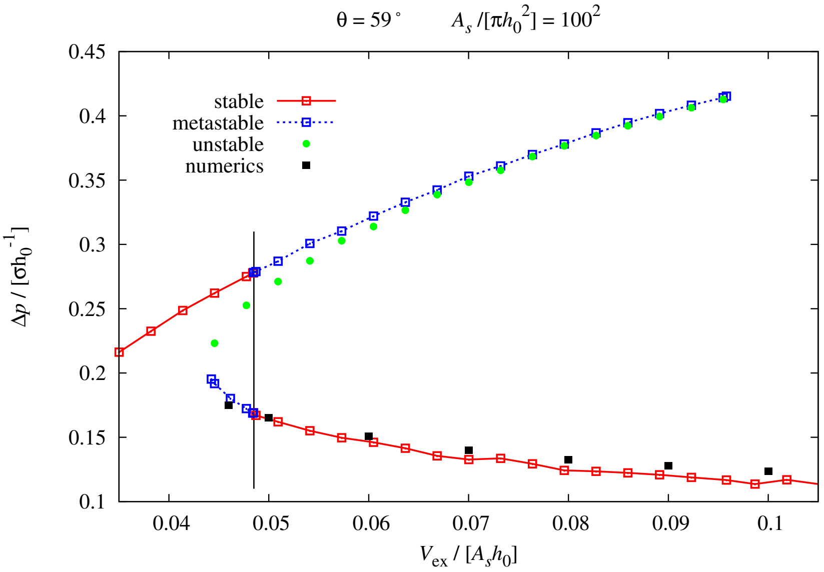

Figure 5.8: The hysteresis of the Laplace pressure Δp with respect to the excess volume V_{ex} for fixed values of the effective contact angle θ and the solid-liquid interfacial area A_s. The upper branch corresponds to uniform wetting films and the lower one to mesoscopic droplets. The transition from stability to metastability is marked by the blue line. The pink data points refer to local maxima of the effective interfacial free energy $\tilde{\mathcal{F}}$.

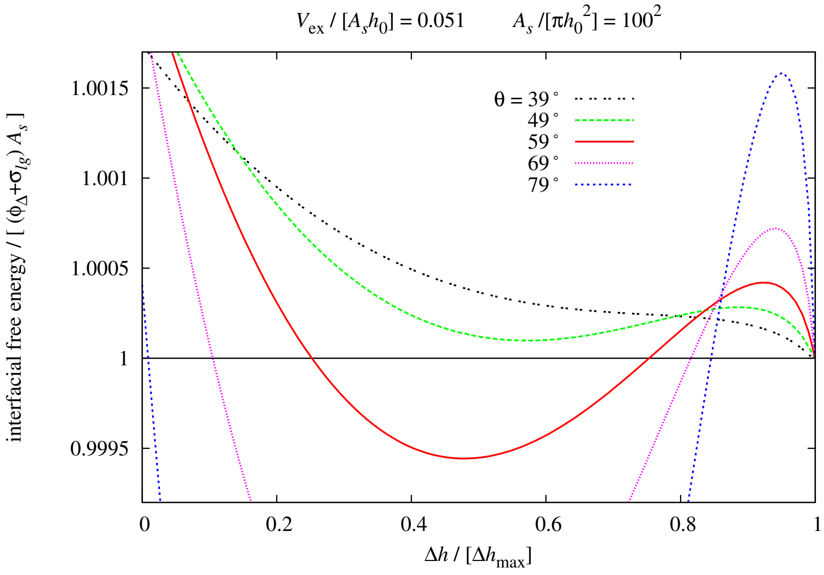

θ	$39°$	$49°$	$59°$	$69°$	$79°$
$\lvert\phi_0/\sigma_{lg}\rvert$	0.223	0.344	0.485	0.642	0.809

Figure 5.9: The free energy energy as a function of Δh for different values of the contact angle θ illustrates the morphologic transition with respect to θ for a fixed value of the excess volume V_{ex} and a fixed ratio V_{ex}/A_s.

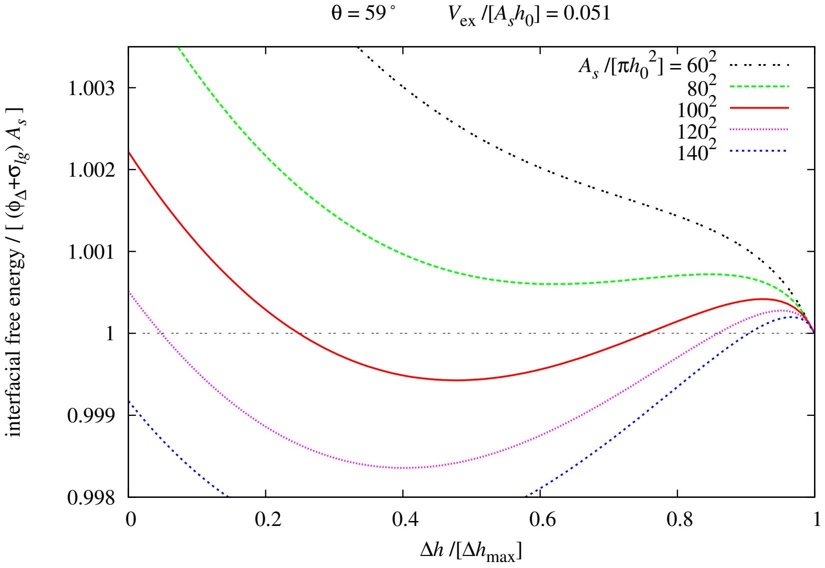

Figure 5.10: The morphologic transition with respect to the excess volume V_{ex} and the solid-liquid interfacial area A_s for a fixed effective contact angle θ. The fixed ratio $V_{\mathrm{ex}}/[A_s h_0]$ for different values of V_{ex} corresponds to a uniform film spreading at constant height.

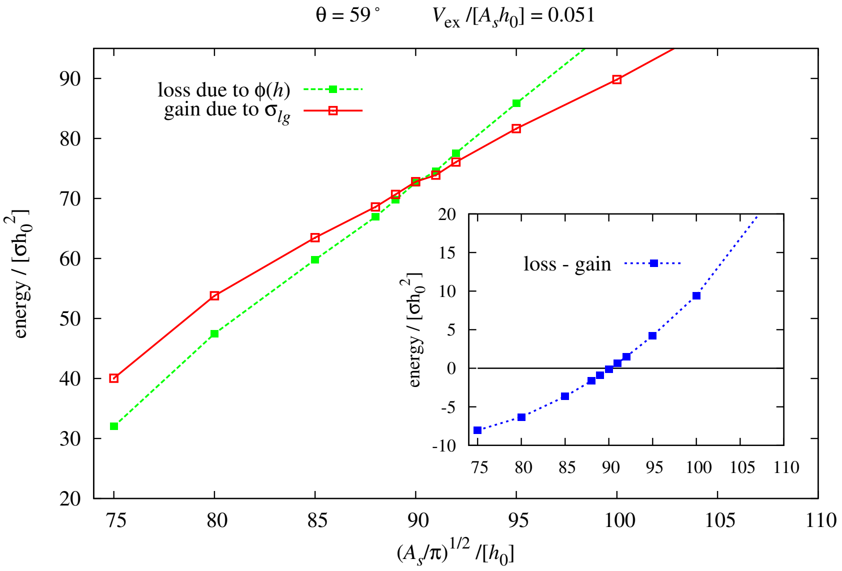

Figure 5.11: Energetic gain due to the interfacial tension σ_{lg} and energetic loss due to the effective interface potential $\phi(h)$ of a mesoscopic droplet with respect to a uniform film as a function of the solid-liquid interfacial area A_s for a constant ratio $V_{\mathrm{ex}}/[A_s h_0]$.

Bibliography

[1] T. Young. An essay on the cohesion of fluids. *Philos. Trans. Roy. Soc. London*, 95:65, 1805.

[2] P.S. Laplace. *Traite de Mechanique celeste; Supplement au Dixieme Livre sur l'Action Capillaire.* Courcier, Paris, 1806.

[3] P.S. Laplace. *Supplement a la Theorie de l'Action Capillaire.* Courcier, Paris, 1807.

[4] C.F. Gauss. 1877. Principia generalia theoriae figurae fluidorum in statu aequilibrii. In: *Carl Friedrich Gauss. Werke* Vol. 5. Königl. Gess. Wiss. Göttingen. 2nd ed.

[5] C. Domb, J.L. Lebowitz, editor. S. Dietrich in *Phase transitions and Critical Phenomena.* Academic Press, 1988.

[6] W. Barthlott and C. Nienhuis. The purity of sacred lotus or escape from contamination in biological surfaces. *Planta*, 202:1, 1997.

[7] N. Goirdano and J.T. Cheng. *J. Phys.: Cond. Matter*, 13:R271, 2001.

[8] P. Mitchell. Microfluidics - downsizing large-scale biology. *Nat. Biotech.*, 19:717, 2001.

[9] T. Thorsen, S.J. Maerkl, and S.R. Quake. Microfluidic large scale integration. *Science*, 298:580, 2002.

[10] K. Handique, D.T. Burke, C.H. Mastrangelo, and M.A. Burns. *Anal. Chem.*, 72:4100, 2000.

[11] B. Zhao, J.S. Moore, and D.J. Beebe. *Anal. Chem.*, 74:4259, 2002.

[12] P. Lam, K.J. Wynne. and G. Wnek. *Langmuir*, 18:948, 2002.

[13] H. Gau. S. Hermingshaus. P. Lenz. and R. Lipowsky. Liquid morhologies on structured surfaces: From microchannels to microchips. *Science*, 283:46, 1999.

[14] A.A. Darhuber. S.M. Troian and W.W. Reisner. *Phys. Rev. E*, 64:031603, 2001.

[15] N.L. Jeon et al. *Biomed. Mircodev.*, 4:117, 2002.

[16] R. Mukhopadhyay. What does nanofluidics have to offer? *Anal. Chem.*, 78:7379, 2006.

[17] J.C.T. Eijkel and A. van den Berg. Nanofluidics: What is it and what can we experct from it? *Microfluid Nanofluid*, 1:249, 2005.

[18] M.L. Kovarik and S.C. Jacobsen. Attoliter-scale dispensening on nanofluidic channels. *Anal. Chem.*, 79:1655, 2007.

[19] G.P. Lopez, H.A. Biebuyck, C.D. Frisbie and G.M. Whitesides. Imageing of features on surfaces by condensation figures. *science*, 260(647), 1993.

[20] E. Meyer and H.G. Braun. Controlled dewetting processes on microstructured surfaces - a new procedure for thin film microstructuring. *Macromol. Mat. Eng.*, 276:44, 2000.

[21] A. Valencia, M. Brinkmann, and Reinhard Lipowsky. Liquid bridges in chemically structured slit pores. *Langmuir*, 17:3390, 2001.

[22] R.C. Hayward, D.A. Saville, and I.A. Aksay. Electrophoretic assembly of colliodal crystals with optical tunable micropatterns. *nature*, 404:56, 2000.

[23] A.M. Higgins and R.A.L. Jones. Anisotropic spinodal dewetting as a route to selfassembly of patterned surfaces. *nature*, 404(476), 2000.

[24] F. Burmeister, C. Schäfle, T. Matthes, M. Böhnisch, J. Boneberg, and P. Leiderer. Colloid monolayers as versatile lithographic masks. *Langmuir*, 13:2983, 1997.

[25] Local oxidation of silicon surfaces by dynamic force microscopy: Nanofabrication and water bridge formation. *Appl. Phys. Lett.*, 72:2295, 1998.

[26] U. Drodofsky, J. Mylnek, et al. Hexagonal nanostructures generated by light masks for neutral atoms. *Appl. Phys. B*, 65:755, 1997.

[27] C. Caccamo, editor. S. Dietrich in *New Approaches to New and Old Problems in Liquid State Theory (NATO-ASI Series C, C529)*. Kluwer, 1999.

[28] C. Bauer and S. Dietrich. Wetting on chemically heterogeneous substrates. *Phys. Rev. E*, 60(6):6919, 1999.

[29] C. Bauer. *Benetzung chemisch strukturierter Substrate.* Thesis, Universität-Gesamthochschule Wuppertal, 1999.

[30] K. Mecke and M. Rauscher. On thermal fluctuations in thin film flow. *J. Phys.: Cond. Matter*, 17(45):S3515, 2005.

[31] G. Grün, K. Mecke, and M. Rauscher. Thin-film flow influenced by thermal noise. *J. Stat. Phys.*, 122(6):1261, 2006.

[32] A. Oron, S.H. Davis, and S.G. Bankoff. Long-scale evolution of thin liquid films. *Rev. Mod. Phys.*, 69(3):931, 1997.

[33] H. Nogushi and G. Gompper. Transport coefficients of off-lattice mesoscale-hydrodynamics simulation techniques. *Phys. Rev. E*, 78:016706, 2008.

[34] S. Succi. *The Lattice Boltzmann Equation for Fluiddynamics and beyond.* Oxford University Press, 2001.

[35] J.P. Rivet and J.P. Boon. *Lattice Gas Hydrodynamics.* Cambridge University Press, 2001.

[36] S. Chen and G.D. Doolen. Lattice Boltzmann method for fluid flows. *Annu. Rev. Fluid Mech.*, 30:329, 1998.

[37] S. Mechkov, G. Oshanin, M. Rauscher, M. Brinkmann, A. M. Cazabat and S. Dietrich. Contact line stability of ridges and drops. *Europhys. Lett.*, 80(6):66002, 2007.

[38] P. Lenz and R. Lipowsky. Stability of droplets and channels on homogeneous and structured surfaces. *Euro. Phys. J.E*, 1:249, 2000.

[39] R. Lipowsky. Structured surfaces and morphological wetting transitions. *Int. Sci.*, 9:105, 2001.

[40] M. Brinkmann and R. Lipowsky. Wetting morphologies on substrates with striped surface domains. *J. Appl. Phys.*, 92(8):2002, 4296.

[41] Martin Brinkmann. *Benetzung lateral strukturierter Oberflächen.* Thesis, Universität Potsdam, 2002.

[42] P. Lenz and R. Lipowsky. Morphological transitions of wetting layers on structured substrates. *Phys. Rev. Lett.*, 80(9):1920, 1998.

[43] A. Moosavi, M. Rauscher, and S. Dietrich. Motion of nanodroplets near chemical heterogeneities. *Langmuir*, 24(3):734, 2008.

[44] A. Moosavi, M. Rauscher, and S. Dietrich. Size dependent motion of nanodroplets on chemical steps. *J. Chem. Phys.*, 129(4):044706, 2008.

[45] S. Mechkov, M. Rauscher, and S. Dietrich. Stability of liquid ridges on chemical micro- and nanostripes. *Phys. Rev. E*, 77(6):061605, 2008.

[46] J. Koplik and T.S. Lo; M. Rauscher and S. Dietrich. Pearling instability of nanoscale fluid flow confined to a chemical channel. *Physics of Fluids*, 18:032104, 2006.

[47] M. Rauscher, S. Dietrich, and J. Koplik. Shear flow pumping on open microfluidic systems. *Phys. Rev. Lett.*, 98(22):224504, 2007.

[48] A. Dupuis and J.M. Yeomans. Lattice Boltzmann modelling of droplets on chemically heterogeneous substrates. *Future Generation Computer Systems*, 20:993, 2004.

[49] H. Kusumaatmaja and J.M. Yeomans. Controlling drop size and polydispersity using chemically patterned surfaces. *Langmuir*, 23:956, 2007.

[50] M. Rauscher and S. Dietrich. Wetting phenomena in nanofluidics. *Ann. Rev. Mater. Research*, 28:143, 2008.

[51] R. Blossey, A. Münch, M. Rauscher, and B. Wagner. Slip vs viscoelasticity in dewetting thin films. *Eur. Phys. J. E*, 20(3):267, 2006.

[52] R. Fetzer, M. Rauscher, R. Seemann, K. Jacobs, and K. Mecke. Thermal noise influences fluid flow in thin films during spinodal dewetting. *Phys. Rev. Lett.*, 99(11):114503, 2007.

[53] M. Rauscher, R. Blossey, A. Münch, and B. Wagner. Spinodal dewetting of thin films with large interfacial slip: implications from the dispersion relation. *Langmuir*, 24(21):12290, 2008.

[54] R. Seemann, S. Herminghaus, and K. Jacobs. Dewetting patterns and molecular forces: A reconciliation. *Phys. Rev. Lett.*, 86(24):5534, 2001.

[55] R. Seemann, S. Herminghaus, and K. Jacobs. Gaining control of pattern formation of dewetting liquid films. *J. Phys.: Cond. Mat.*, 13:4925, 2001.

[56] L. Luo. Theory of the lattice Boltzmann method: Lattice Boltzmann for nonideal gases. *Phys. Rev. E*, 62(4):4982, 2000.

[57] J.O. Hirschfelder, C.F. Curtis, and R.B. Bird. *Molecular Theory of Gases and Liquids.* Wiley and Sons, 1967.

[58] F. Brochard-Wyart, D. Quere, and P.G. de Gennes. *Capilarity and Wetting Phenomena.* Springer, 2004.

[59] J.S. Rowlinson, B. Widom. *Molecular Theory of Capillarity.* Dover Publications, 1982.

[60] Samuel A. Safran. *Statistical Thermodynamics of Surfaces, Interfaces, and Membranes.* Westview Press, 2003.

[61] L. Landau, E.M. Lifshitz. *Fluid Mechanics.* Verlag Harry Deutsch, 3rd edition.

[62] L. Landau, E.M. Lifshitz. *Theory of Elasicity.* Pregamon Press, Oxford, 2nd edition.

[63] M. Napiorkowski and S. Dietrich. Analytics results form wetting transitions in the presence of van der Waals tails. *Phys. Rev. A*, 43(4):1861, 1991.

[64] R. Evans. The nature of the liquid-vapour interface and other topics in the statistical mechanics of non-uniform classical fluids. *Advances in Physics*, 28(2):143, 1979.

[65] C. Bauer and S. Dietrich. Quantitative study of laterally inhomogeneous wetting films. *Eur. Phys. J. B*, 10:767, 1999.

[66] S. Dietrich and M. Napiorkowski. Structure of the effective hamiltonian for liquid-vapour interfaces. *Phys. Rev. E*, 47(3):1836, 1993.

[67] J. Charvolin et al., editor. M. Schick in *Liquids at interfaces.* Elsevier, Amsterdam, 1989.

[68] K. Brakke. The surface evolver. *Experimental Mathematics*, 1(2):141, 1992.

[69] G.K. Batchelor. *An Introduction to Fluid Dynamics.* Cambridge Univesity Press, 2000.

[70] H. Bruus. *Theoretical Microfluidics.* Oxford University Press, 2008.

[71] L. Landau, E.M. Lifshitz. *Statistical Physics.* Verlag Harry Deutsch, 3rd edition.

[72] C. Cercignani. *Theory and application of the Boltzmann equation.* Scottish Academic Press, 1975.

[73] M.N. Kogan. *Rarefied Gas Dynamics.* Plenum, New York, 1969.

[74] P.M. Resibois. *Classical kinetic theory of fluids.* Wiley and Sons, 1977.

[75] S.G. Brush, editor. D. Enskog in *Kinetic Theory*, volume 3. Pergamon Press, 1972.

[76] S. Chapman, T.G. Cowling. *The Mathematical Theory of Non-uniform Gases.* Cambridge University Press, 1970.

[77] E.P. Gross, M. Krook, and P.L. Bhatnagar. A model for collision processes in gases. *Phys. Rev.*, 94(3):511, 1954.

[78] P. Welander. *Arkiv Fysik*, 7:507, 1954.

[79] B. Hasslacher Y. Pomeau, U. Frisch. Lattice-gas automata for the Navier-Stokes equation. *Phys. Rev. Lett.*, 56(14):1505, 1986.

[80] L. Luo. A priori derivation of the lattice Boltzmann equation. *Phys. Rev. E*, 55(6):R6333, 1997.

[81] X. Shan and H. Chen. Lattice Boltzmann model for simulating flows with multiple phases and components. *Phys. Rev. E*, 47(3):1815, 1993.

[82] X. Shan and H. Chen. Simulation of nonideal gases and liquid-gas phase transitions by the lattice Boltzmann equation. *Phys. Rev. E*, 49(4):2941, 1994.

[83] M. Nekovee, P.V. Coveney, H. Chen, and B.M. Boghosian. Lattice Boltzmann model for interacting amphiphilic fluids. *Phys. Rev. E*, 62(6):8282, 2000.

[84] M.R. Swift, W.R. Osborn, and J.M. Yeomans. Lattice Boltzmann simulation of nonideal fluids. *Phys. Rev. Lett.*, 75(5):830, 1995.

[85] A.J. Briant, A.J. Wagner, and J.M. Yeomans. Lattice Boltzmann simulations of contact line motion: Liquid-gas systems. *Phys. Rev. E*, 69:031602, 2004.

[86] A.J. Briant and J.M. Yeomans. Lattice Boltzmann simulations of contact line motion: Binary fluids. *Phys. Rev. E*, 69:031603, 2004.

[87] J. Chin, J. Harting, M. Nekovee, N. Gonzales-Segredo, M. Venturoli and P.V. Coveney. *LB3D V5.0: A Parallel Implementation of the Lattice-Boltzmann Method for the Simulation of Interacting Amphiphilic Fluids.* Center for Computational Science, University College, London, U.K.; Christopher Ingold Labs, London, U.K.; Institute for Computational Physics, University of Stuttgart, Germany.

[88] D.J. Holdych et al. An improved hydrodynamics formulation for multiphase flow lattice Boltzmann models. *Int. J. Mod. Phys.*, C9:1393, 1998.

[89] D.P. Ziegler. Boundary conditions for lattice Boltzmann simulations. *J. Stat. Phys.*, 71(5/6):1171, 1993.

[90] S. Chen, D. Martinez and R. Mei. On boundary conditions in lattice Boltzmann methods. *Physics of Fluids*, 8(9):2527, 1996.

[91] J.W. Cahn and J.E. Hillard. *J. Chem. Phys.*, 28:258, 1958.

[92] D.M. Anderson, G.B. McFadden, and A.A. Wheeler. Diffuse-interface methods in fluid mechanics. *Rev. Fluid Mech.*, 30(139), 1998.

[93] P. Seppecher. Moving contact lines in the Cahn-Hilliard theory. *Int. J. Engng. Sci*, 34:977, 1996.

[94] J.W. Cahn. Critical point wetting. *J. Chem. Phys.*, 66:3667, 1997.

[95] D.H. Rothmann and J.W. Keller. Immiscible cellular-automaton fluids. *J. Stat. Phys.*, 52(3/4):1119, 1988.

[96] H. Chen, B.M. Boghosian, P.V. Coveney, and M. Nekovee,. A ternary lattice Boltzmann model for amphiphilic fluids. *Proc. Roy. Soc.*, A(456):2043, 2000.

[97] B. Levich. *Physicochemical Hydrodynamics.* Prentice-Hall, London, 1962.

[98] L. Landau and B. Levich. *Acta Physicochim. USSR*, 17:42, 1942.

[99] P.G. de Gennes. *Colloid Polym. Sci.*, 246:463, 1986.

[100] R.G. Cox. *J. Fluid Mech.*, 168:169, 1986.

[101] Jens Harting and Fatollah Varnik. private communication.

[102] S. Chandrasekhar. *Hydrodynamic and Hydromagnetic Stability.* Dover, New York, 1981.

[103] H.L.F. Helmholtz. On the discontinuous movements of fluids. *Monthly Reports of the Royal Prussian Academy of Philosophy*, 23:215, 1868.

[104] W.T. Kelvin. Hydrokinetic solutions and observations. *Philosophical Magazine*, 42:362, 1871.

[105] S. Schmieschek and J. Harting. Contact angle determination in multicomponent lattice Boltzmann simulations. *to be published*, http://arxiv.org/abs/0910.3915.